Nonlinear Dynamic Process Characterization of Lithium-Ion Batteries: A Model-Based Approach

Von der Fakultät für Maschinenbau

der Technischen Universität Carolo-Wilhelmina zu Braunschweig

zur Erlangung der Würde

eines Doktor-Ingenieurs (Dr.-Ing.)

genehmigte Dissertation

von: Nicolas Alexander Wolff

aus (Geburtsort): Bremen

eingereicht am: 06.05.2019

mündliche Prüfung am: 27.09.2019

Gutachter: Prof. Dr.-Ing. Ulrike Krewer

Prof. Dr. rer. nat. habil. Wolfgang Bessler

2019

Today's scientists have substituted mathematics for experiments, and they wander off through equation after equation, and eventually build a structure which has no relation to reality.

Nikola Tesla

Publications within the Research of this Thesis

Journal Publications

- Wolff, N., Harting, N., Röder, F., Heinrich, M. and Krewer, U.
  Understanding Nonlinearity in Electrochemical Systems, European Physical Journal Special Topics 227, 2617-2640, 2019

- Wolff, N., Harting, N., Heinrich, M., Krewer, U.
  Nonlinear Frequency Response Analysis on Lithium-Ion Batteries: Process Identification and Differences between Transient and Steady-State Behavior, Electrochimica Acta 298, 788-798, 2019

- Wolff, N., Röder, F., Krewer, U.
  Model Based Assessment of Performance of Lithium-Ion Batteries Using Single Ion Conducting Electrolytes, Electrochimica Acta 284, 639-646, 2018

- Wolff, N., Harting, N., Heinrich, M., Röder, F. and Krewer, U.
  Nonlinear Frequency Response Analysis on Lithium-Ion Batteries: A Model-Based Assessment, Electrochimica Acta 260, 614-622, 2018

- Heinrich, M., Wolff, N., Harting, N., Röder F. and Krewer, U.
  Physico-Chemical Modeling of a Lithium-Ion Battery: An Aging Study with Electrochemical Impedance Spectroscopy, Batteries & Supercaps 2, 1-12, 2018

- Laue, V., Wolff, N., Röder, F. and Krewer, U.
  The Influence of Mixing Strategies on Micro Structural Properties of All—Solid State Electrodes, Energy Technology, 2194-4288, 2019

- Harting, N., Wolff, N., Röder, F. and Krewer, U.
  State-Of-Health Diagnosis of Lithium-Ion Batteries Using Nonlinear Frequency Response Analysis, Journal of The Electrochemical Society 166, 2, 277-285, 2019

- Harting, N., Wolff, N. and Krewer, U.
  Identification of Lithium Plating in Lithium-Ion Batteries using Nonlinear Frequency Response Analysis (NFRA), Electrochimica Acta 281, 378-385, 2018,

- Harting, N., Wolff, N., Röder, F. and Krewer, U.
  Nonlinear Frequency Response Analysis (NFRA) on Lithium-Ion Batteries, Electrochimica Acta 248, 133-139, 2017

- Harting, N., Schenkendorf, R. Wolff, N. and Krewer, U.
  State-Of-Health Identification of Lithium-Ion-Batteries Based on Nonlinear Frequency Response Analysis: First Steps with Data Mining, Applied Sciences 8, 821, 1-14, 2018

Conference Contributions

- Wolff, N., Harting, N., Heinrich, M., Röder, F., Krewer, U.
  A Nonlinear Model-Based Study for Dynamic-Steady-State Process Identification on Lithium-Ion Batteries, Presentation, 232nd Meeting of the Electrochemical Society, 2017

- Wolff, N., Harting, N., Heinrich, M., Röder, F., Krewer, U.
  A nonlinear model approach for separation and identification of processes in Lithium-ion batteries, Presentation, Kraftwerk Batterie, 2017

- Wolff, N., Heinrich, M., Harting, N., Röder, F., Seitz, S., Krewer, U.
  Analysing and Ageing Induced Changes in Lithium-Ion Batteries by Correlating EIS Simulations and Experiments, Poster and Presentation, Batterieforum, 2018

- Wolff, N., Harting, N., Heinrich, M., F., Krewer, U.
  Lithium-Ion Battery Process Identification with Nonlinear Frequency Response Analysis, Poster, Kraftwerk Batterie, 2018

- Wolff, N., Heinrich, M., Harting, N., Röder, F., Seitz, S., Krewer, U.
  Analysing and Ageing Induced Changes in Lithium-Ion Batteries by Correlating EIS Simulations and Experiments, Poster, 232nd Meeting of the Electrochemical Society, 2017

- Wolff, N., Heinrich, M., Röder, F., Krewer, U.
  Modeling of All-Solid-State Batteries, Poster, Bunsen-Kolloqium: Solid-State Batteries II, 2016

Acknowledgements

This thesis is the result of years of enthusiasm towards science and hard work and was accompanied by joy, frustration, friendship and love. Numerous people have helped and have a decisive share at the success of this thesis.

First of all, I have to thank my Professor, Ulrike Krewer for the continuous and intensive and rigorous support. Without her patience, motivation, enthusiasm and immense knowledge, this thesis would not have been possible. Further, I would like to thank the second examiner of my thesis Professor Wolfgang Bessler and the chair of the examination committee Professor Georg-Peter Ostermeyer

My sincere thanks also goes to my coworkers and friends Marco Heinrich, Vincent Laue, Oke Schmidt, Max Röhe and Fridolin Röder for numerous productive, fruitful and nice meetings, projects and hours of modeling sessions. Additionally, I would like to express my thanks to Wilfried Janßen, Ina Schunke and Horst Müller.

Last but not least I take this opportunity to express the profound gratitude from deep heart to my beloved parents, my family and my girlfriend Nina Harting for their love and continuous support.

Thanks!

Abstract

Understanding of Lithium-ion batteries and underlying processes is highly important, due to the change from fossil fuel driven to battery driven vehicles. This thesis introduces a novel nonlinear dynamic measurement method, so called Nonlinear Frequency Response Analysis (NFRA), with the purpose of extensive understanding of processes within Lithium-ion batteries with liquid and with solid electrolytes, respectively.

After the thesis is brought into context, a systematic model-based analysis of an electrochemical system is conducted for the first time with NFRA. For this, the excitation of higher harmonic voltage responses due to fundamental processes in electrochemical systems, such es reaction and diffusion, is investigated. Results thereby show that the degree of symmetry of the current-voltage relation strongly influences the excitation of second and third harmonic responses. Based on this information, a state-of-the-art Pseudo-Two-Dimensional battery model is investigated, and simulated results are compared to measured spectra, thereby showing great agreement. NFRA is further used to understand the impact of the most prominent ageing factor, the Solid-Electrolyte-Interface (SEI). For this purpose a Single-Particle model is extended with a SEI. Then, differences between the initial excitation and steady-state are deeply investigated. Model-based studies further show that the fundamental working principle of the transport of Lithium-ions through the SEI/electrolyte interface can be better investigated with NFRA compared to the linear Electrochemical Impedance Spectroscopy.

To not only account for current generation Lithium-ion batteries, higher harmonic voltage responses of next generation batteries with a single-ion-conducting solid electrolyte are additionally investigated. They are believed to be one of the most promising future battery designs. NFRA on next generation batteries shows benefits concerning fast charging and thick electrode designs due to smaller nonlinearities, resulting from different electrolyte processes.

This, overall, demonstrates that process characterization and identification of present as well as next generation Lithium-ion batteries can highly benefit from the combi-

nation of NFRA and commonly applied methods, such as Electrochemical Impedance Spectroscopy.

Kurzfassung

Durch den Umschwung von Fahrzeugen mit konventionellen Verbrennungsmotor hin zu Batterie-elektrischen Fahrzeugen ist das Verständnis von Lithium-Ionen-Batterien und deren Prozessen essentiell und zunehmend wichtig. Innerhalb dieser Doktorarbeit wird eine neuartige nichtlineare, dynamische Messmethode, die sogenannte Nonlinear Frequency Response Analysis (NFRA) eingeführt, um das Verständnis über Batterien und Batterieprozesse signifikant zu erhöhen.

Nachdem diese Arbeit innerhalb einer Literaturrecherche in Kontext gebracht wird, findet eine fundierte, systematische Analyse elektrochemischer Systeme statt. Die Ergebnisse zeigen dabei, dass der Grad der Asymmetrie der Strom-Spannungskurve entscheidend für die Anregung der zweiten bzw. dritten Harmonischen ist. Im nächsten Teil der Arbeit wird dieses Wissen verwendet und auf ein Pseudo-Zweidimensionales Batterie-Modell angewendet. Die Simulationsergebnisse werden dabei mit gemessenen Spektren verglichen und zeigen eine sehr gute Übereinstimmung. Das Verständnis der Alterung von Lithium-Ionen-Batterien ist eines der wichtigsten Forschungsthemen in Bezug auf Lithium-Ionen-Batterien. Insbesondere der Einfluss der sogenannten Solid-Electrolyte-Interface (SEI) ist hierbei zu nennen. Da diese maßgeblich für die Alterung von Batteriezellen verantwortlich ist, wird sie in einem nächsten Schritt in ein Single-Particle Modell implementiert. Mit dem Single-Particle Modell werden Unterschiede der initialen Anregung und des eingeschwungenen Zustandes untersucht. Simulationsergebnisse zeigen weiterhin, dass mit klassischen Methoden, wie der Elektrochemischen Impedanzspektroskopie, keine Aussage über die Linearität bzw. Nichtlinearität des Transports von Lithium-Ionen durch die Grenzfläche zwischen SEI und Elektrolyt getroffen werden kann. Mittels NFRA ist es allerdings möglich, zu unterscheiden, ob dieser Prozess linear oder nichtlinear ist.

Zusätzlich zu klassischen Lithium-Ionen-Batterien mit flüssigen Elektrolyten werden im letzten Teil der Arbeit sogenannten Einzel-Ionen leitende Festelektrolytsysteme mit NFRA untersucht, da sie als eines der vielversprechendsten zukünftigen Batteriedesigns gelten. Hierbei werden Vorteile des Festelektrolytsystems in Bezug auf Schnellladefähigkeit und Hochenergiezellen durch den weniger limitierenden Elek-

trolyten deutlich.

Daraus lässt sich schlussfolgern, dass NFRA, insbesondere in Kombination mit der verbreiteten und linearen Elektrochemischen Impedanzspektroskopie, eine vielversprechende dynamische Messmethode darstellt.

Contents

List of Figures

List of Tables

1 Introduction[1]

In times where every device, even cars, are battery powered, demands on batteries concerning energy density, safety and cycle life continuously increase. One way to meet these demands is understanding of the battery to be able to perform detailed design optimization and an adaption of operational parameters. Current state-of-the-art are Lithium-ion batteries (LiB) with a liquid, organic electrolyte.

Focus of this thesis is the understanding of batteries by introducing a novel nonlinear dynamic measurement method in a model-based approach. This method is called Nonlinear Frequency Response Analysis (NFRA). In this Chapter, first an in-depth study of the state-of-art of LiB, their modeling and dynamic measurement methods is provided before the working principle of NFRA and the scope of this work are shown in detail.

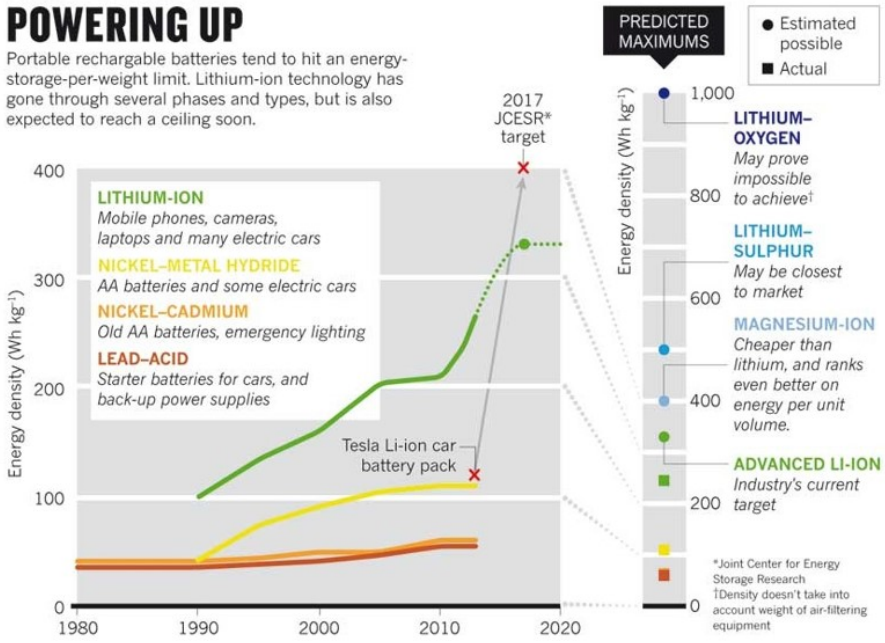

Figure 1.1.: Development of energy density of batteries over time [1].

[1]Parts of this chapter have been published in: Nonlinear Frequency Response Analysis on Lithium-Ion Batteries: A Model-Based Assessment, Electrochimica Acta, 260, 614-622, 2018 [9], in: Physico-Chemical Modeling of a Lithium-Ion Battery: An Aging Study with Electrochemical Impedance Spectroscopy, Batteries & Supercaps,2, 1-12, 2018, [10], in: Nonlinear Frequency Response Analysis on Lithium-Ion Batteries: Process Identification and Differences between Transient and Steady-State Behavior, Electrochimica Acta 298, 788-798 2019 [11], in: Model Based Assessment of Performance of Lithium-Ion Batteries Using Single Ion Conducting Electrolytes, Electrochimica Acta, 284, 639-646, 2018 [12] and in: Understanding Nonlinearity in Electrochemical Systems, European Physical Journal Special Topics, 227, 2617-2640, 2019 [13].

1.1. Lithium-Ion Batteries

LiB are promising candidates to enable the change from fossil fuel driven cars to zero-emission vehicles as they are the batteries with the highest energy density in mass production for automotive application, as shown in Figure 1.1.

In most current generation LiB, graphite is used as anode material since its open circuit potential as well as its costs are low [2]. On the cathode side, Nickel Manganese Cobalt Oxide (NMC111) is currently one of the most popular materials [14]. Nevertheless, current trends show that future cathodes focus on Nickel rich compositions (NMC622, NMC811 or NCA) due to their higher specific capacity [14, 15]. Between anode and cathode, an electrically insulating separator is placed to prevent short-circuiting.

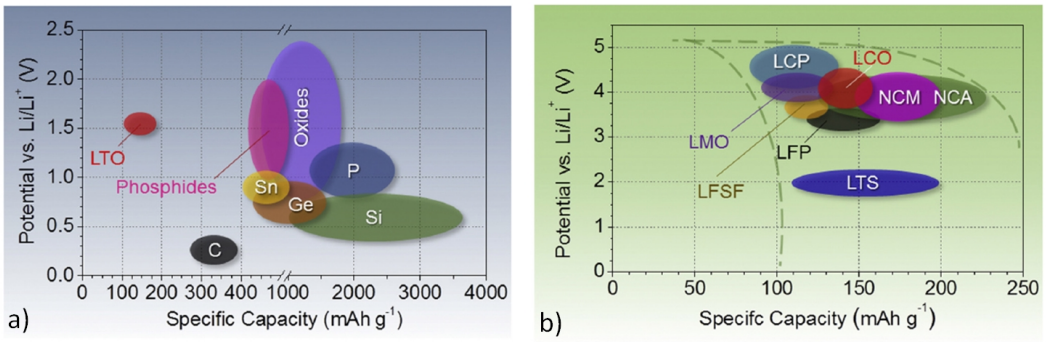

Figure 1.2.: Schematic illustration of potential against Lithium over specific capacity of a) anode and b) cathode active materials [2].

In Figure 1.2, the general potential of various active materials for the anode and cathode are shown over theoretical specific capacity. It can be seen that, on the anode side, one highly benefits from adding Silicon [2]. Nevertheless, Silicon has a high volume expansion which leads to mechanical stress and one is therefore limited concerning the maximum amount of Silicon in the negative electrode [16].

The general working principle of LiBs is shown in Figure 1.3. During battery discharge, Lithium deintercalates from the porous anode and reacts to Lithium-ions at the surface of the anode active material particles. The Lithium-ions further move through the electrolyte towards the cathode via migration and diffusion. Here, the second main charge transfer reaction, the reduction of Lithium-ions, takes place and the resulting Lithium intercalates into the cathode. For the charging process, the described procedure is vice versa.

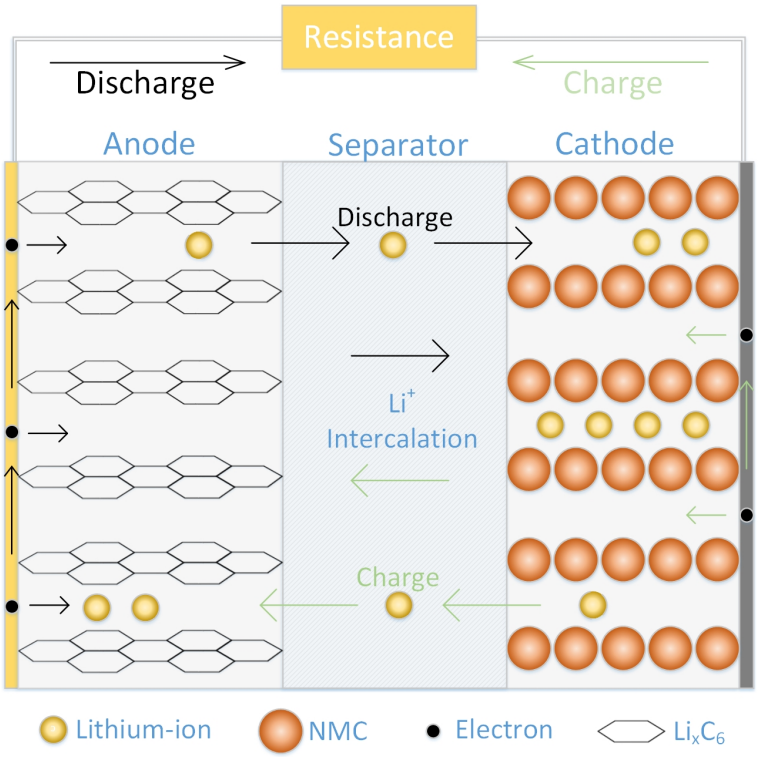

Figure 1.3.: Schematic illustration of the working principle of a LiB.

Current generation batteries commonly use a liquid, so called binary, electrolyte, such as a solvent mixture of ethylene carbonate and diethyl carbonate, in which the ionic conductivity is assured by adding conducting salts such as Lithium hexafluorophosphate [10]. The electrolyte is distributed in the porous electrodes and the separator. The reactions can be described as follows [17]:

$$\begin{aligned} \text{anode}: \quad & \mathrm{Li}_x\mathrm{C}_6 && \leftrightharpoons x\mathrm{Li}^+ + x\mathrm{e}^- + \mathrm{C}_6 \\ \text{cathode}: \quad & \mathrm{Li}_{1-x}\mathrm{MO}_2 + x\mathrm{Li}^+ + x\mathrm{e}^- && \leftrightharpoons \mathrm{LiMO}_2 \\ \text{total}: \quad & \mathrm{Li}_{1-x}\mathrm{MO}_2 + \mathrm{Li}_x\mathrm{C}_6 && \leftrightharpoons \mathrm{LiMO}_2 + \mathrm{C}_6 \end{aligned}$$

After decades of extensive research, liquid electrolyte cells still offer many challenges to be faced. One of these is rightful understanding of ageing. The liquid electrolyte is operated outside its electrochemical stability window and it is therefore reduced at the anode during the first cycles [18]. The reduction reaction leads to the growth of a passivating layer, so called Solid-Electrolyte-Interface (SEI), on the anode particles which protects the electrolyte from further reduction [19]. The SEI and all corresponding processes, such as formation, conversion and growth, are assumed to

be the dominating effects concerning ageing of LiB with liquid electrolytes and are, among others, shown in Figure 1.4 [20, 3].

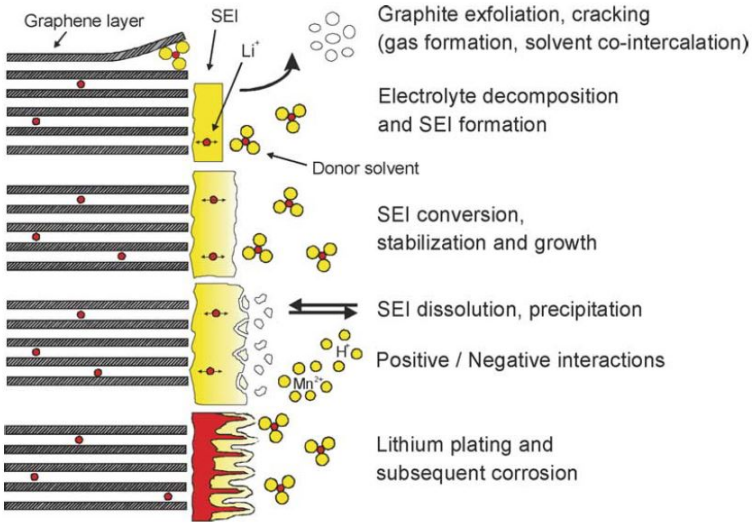

Figure 1.4.: Schematic illustration ageing effect in LiB [3].

The critical aspects using those electrolytes are electrolyte leakage, high risk of thermal runaway and low power density. An often proposed possible solution is using inorganic solid electrolytes, because they can overcome these issues [21]. There are various types of inorganic solid electrolytes available. Experimental investigations are presently mainly focused on glasses and crystals [21]. The advantages of glasses compared to crystals are a higher ionic conductivity, isotropic properties and no grain boundaries [22]. In particular, sulfidic glasses are expected to be promising candidates, because they have a very high ionic conductivity at room temperature due to the high polarizability of sulfur ions. This will enable application with porous electrodes. Further, since sulfidic glasses are single ion conductors, no side reactions that are caused by reactions with counter ions occur [23, 24, 25]. Presently, the two most crucial challenges in the development of cells based on solid electrolytes are to achieve an ionic conductivity comparable to liquid electrolytes at room temperature and to minimize the high resistances at the contact area between active material and electrolyte [26]. To overcome the first issue, sulfidic glasses can be used. Further, the contact resistance, called interdiffusion layer, can be minimized by coating of the active material particles [27]. As sulfidic glasses, such as $70Li_2S30P_2S_5$ [21], are promising, focus is laid on comparing such All-Solid-State Batteries (ASSB) to classical LiB. Overall, this review has shown that ASSB in general are a favorable fu-

ture battery design. Nevertheless, for an optimal application, it is essential to develop extensive understanding of processes of this kind of battery, especially in comparison to classical LiB.

1.2. Dynamic Diagnosis of Lithium-Ion Batteries

Deep understanding of processes underlying batteries is getting more important for further improvement in performance and safety for current and next generation batteries. Efforts have been undertaken to increase the understanding of processes to be able to increase the cells durability, long-term stability and minimize production costs. Among these efforts, this thesis is placed.

Processes in batteries in general can be analyzed with stationary methods, such as C-rate tests [28], Differential Voltage Analysis [29] and Incremental Capacity Analysis [30] and further, with linear dynamic measurement method, such as Electrochemical Impedance Spectroscopy (EIS) [10]. Other nonlinear techniques are Cyclovoltammetry (CV) and Chronoamperometry (CA) or -potentiometry (CP). CV is usually employed for in-depth study of reaction and sorption processes at single electrodes or for material characterization regarding performance, active area and stability [31, 32]. It thus often focuses on surface processes studied on plain electrodes in solutions, but it is seldomly applied to full cells, as transport processes make signal interpretation difficult [31, 33]. Also CA or CP are frequently applied for material characterization and kinetic studies. The method is also applied to full cells, e.g. as Current Interrupt analysis for determining Ohmic resistance in fuel cells or batteries [34, 35], or to study the interaction of reaction, sorption and transport processes at electrode or cell level [36, 37]. Dynamic electrochemical methods may be coupled with physical or chemical methods, e.g. as done in Differential Electrochemical Mass Spectroscopy [38, 39]. However, CV, CA and CP are less suitable or accurate for separating and separate analysis of fast and slow processes. Here, frequency response analysis techniques, such as NFRA have its advantages, as the results are given over a wide frequency range from mHz to MHz.

Within this thesis, focus is laid on dynamic measurement methods for process characterization. Thus, EIS and NFRA are described in detail.

Electrochemical Impedance Spectroscopy

One of the most advanced and well established dynamic techniques for characterization of electrochemical cells, is the EIS. For reliable EIS measurements, four criteria have to be met: stationarity, causality and linearity and finiteness [40]. The general working principle is schematically shown in Figure 1.5.

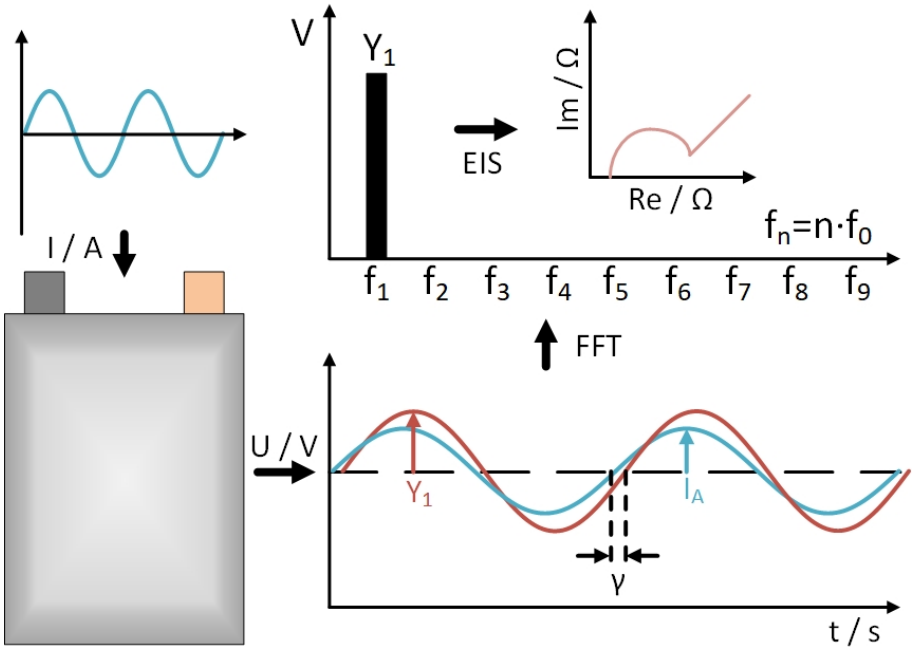

Figure 1.5.: Schematic illustration of the working principle of EIS.

For EIS, the battery is sinusoidally excited with a current with a small amplitude to guarantee linear excitation of the system [41]. The resulting output voltage in the time domain is phase shifted in relation to the excitation current. In a next step, the voltage response in time domain is transferred to the frequency domain via a fast-Fourier transformation (FFT). The linear voltage amplitude, which is the first harmonic Y_1, the excitation amplitude I_A and phase shift γ are used to calculate the real part $Re(Z)$ and imaginary part $Im(Z)$, according to equation 1.1 and equation 1.2 [42].

$$Re(Z) = |Z| \cos \gamma(\omega) = |\frac{Y_1(\omega)}{I_A}| \cos \gamma(\omega) \tag{1.1}$$

$$Im(Z) = |Z| \sin \gamma = |\frac{Y_1(\omega)}{I_A}| \sin \gamma(\omega) \tag{1.2}$$

The calculation of real and imaginary part allows the common presentation of EIS in a Nyquist plot, as shown in Figure 1.6. Additionally, it is possible to display results of

$|Z|$ and the phase shift γ as a Bode plot over the measured frequency.

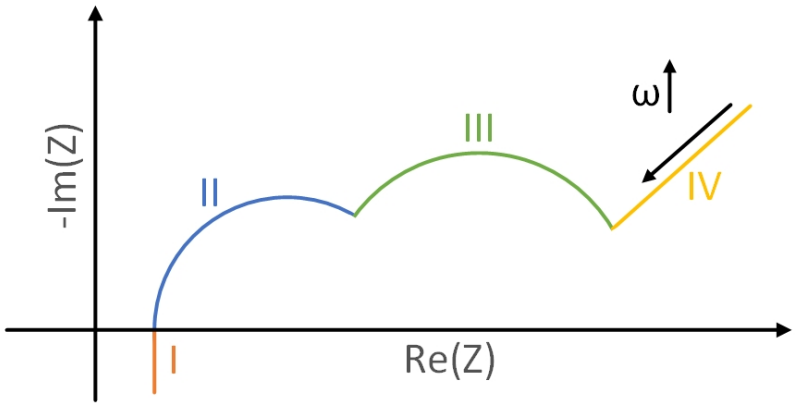

Figure 1.6.: Schematic illustration of the Nyquist plot presentation of an impedance spectrum.

In the Nyquist plot representation, the fastest processes are present at the left hand side of the spectrum with a positive imaginary part (orange). This part is caused by inductive behavior due to metallic elements in the cell and wires. Further, the zero crossing is induced by Ohmic potential losses in the electrodes, the electrolyte and the SEI. In general, charge transfer processes are visible by a semi-circle in the high to mid frequency range (blue and green). The low frequency range is dominated by diffusion processes in the active material (yellow) [10, 41]. Therefore, changes in processes can be accessed, which explains the enormous potential and popularity of EIS.

Commonly, EIS can be applied to detect changes in LiB, in example due to ageing. If liquid electrolyte cells are investigated, changes of the SEI are believed to be the dominating effect for an increase of cell impedance and a loss of capacity [43].

Nevertheless, processes within electrochemical cells, such as the electrochemical reaction and ageing, are nonlinear processes [44, 45] and can show complex nonlinear behavior, i.e. spontaneous oscillation of current or potential [46] and if EIS is applied, not all useful information can be accessed [47], since it is limited to linear analysis. In this case, characterization of processes would benefit from a nonlinear dynamic measurement method, such as NFRA.

Nonlinear Techniques

For NFRA, higher harmonics caused by a sinusoidal deflection with a large current amplitude are used for process identification and characterization [48]. NFRA is com-

monly applied in electrical engineering where the influences of higher harmonics, treated as noise, to power systems are investigated [49]. Another field of application is material science, where higher harmonic generation in solids is used to differentiate between interband and intraband harmonic generation and to determine the ageing behavior of steel [50, 51]. Additionally, electrochemical and corrosion processes are investigated by applying large AC electric signals [52]. NFRA has further been applied to study the nonlinear behavior of ferrocyanide oxidation using a mathematical model [53] and measurements [54]. An additional implementation of NFRA to access nonlinearities in impedance spectra, and further to sense and determine reaction kinetics in an electrochemical cell was investigated by Kiel et al. [55]. Later research focuses on the application of NFRA to electrochemical methanol oxidation using Volterra series. They found that the linear output (EIS) does not contain sufficient information to discriminate between different kinetic models, but NFRA however does [56]. Kadyk et al. further investigated the CO poisoning and dehydration within a PEM fuel cell, using experiments and simulations. The model approach is again based on a Volterra series. They thereby found that CO poisoning can be detected with NFRA due to a change in the second order response, but not with conventional methods such as EIS [57, 58, 59]. Additionally, NFRA was used to identify reaction kinetics of methanol oxidation [60] and oxygen reduction [61] in model based and experimental studies on fuel cells and further for state estimation as well as methanol concentration sensing of a fuel cell [62]. Here a related type of NFRA, so called Total Harmonic Distortion (THD), where higher harmonic voltage responses normalized to the linear output are calculated, is used. A further study of the excitation of higher harmonic voltage responses of Solid Oxide Fuel Cells was investigated by Wilson et al., thereby showing that higher harmonic voltage responses contain specific resonant features [63]. In the field of LiB, Harting et al. were the first to show the experimental application of NFRA, to use it to discriminate between different processes in cells [47] and between different degradation processes [64] and to determine the state-of-health of LiB [65, 66]. The first model-based dynamic studies of the application NFRA on LiBs have been published within this work and contributed to in-depth understanding of nonlinear voltage responses of batteries with a Pseudo-Two-Dimensional (P2D) battery model [9]. Additionally, a base case study to explore the effect of kinetic, mass-transport and

thermodynamic parameters on the harmonics response was conducted by Murbach et al. [67].

In general, despite the obvious advantages, very few groups use this technique, and the method has not yet entered electrochemical textbooks, nor is it widely known. Whereas several of the leading laboratory EIS measurement device suppliers nowadays feature this technology as a free option, researchers may be discouraged by the yet difficult interpretation of the observed features in the spectra. A systematic fundamental analysis of single processes and their impact on NFRA is missing, which prevents wide-spread application of this promising, advanced, but yet not well understood characterization technique. Such a systematic and generic, i.e. application-independent analysis will deliver a sound knowledge base and guideline which experts and newcomers can use for their application specific analyses and is provided within this work. The working principle and enormous potential of NFRA will thereby be explained and demonstrated in detail, later.

Working principle of NFRA

In contrast to the commonly applied EIS, the electrochemical cell is nonlinearly excited for NFRA to access higher harmonic responses. The fundamental working principle of NFRA is schematically shown in Figure 1.7.

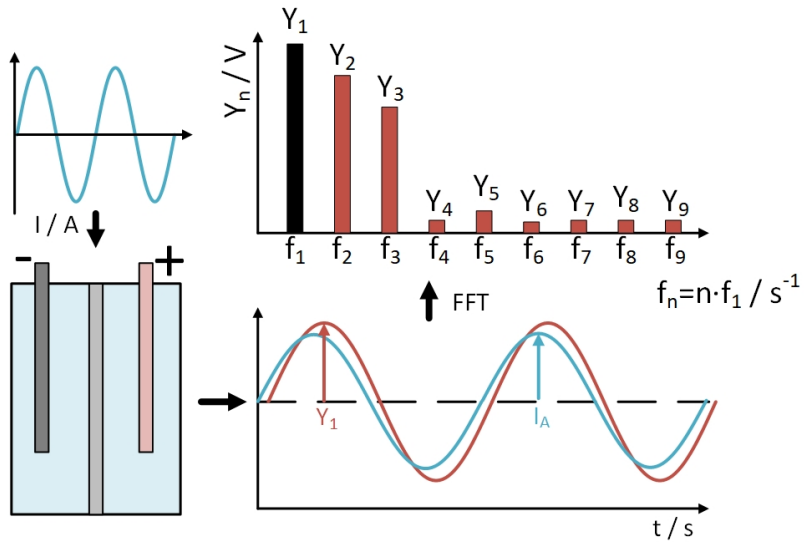

Figure 1.7.: Schematic illustration of the working principle of NFRA.

A sinusoidal current with high AC excitation amplitude is applied to the electrochemical cell or electrode. The dynamic output signal of the voltage to the current input

with frequency f_1 contains besides a sinusoidal voltage response with the amplitude Y_1 with the inlet frequency f_1 also sinusoidal voltage responses of amplitude Y_n with n times the input frequency $f(Y_n) = n \cdot f_1$. To extract and analyze these higher frequency responses from the output voltage signal, it is transferred from the time domain to the frequency domain via a FFT. The corresponding function to extract the amplitudes is implemented in MATLAB. This allows to display higher frequency responses Y_n as a function of the input frequency f_1, shown as an example for the discrete FFT in equation 1.3.

$$Y_n = |\frac{2}{b}\sum_{j=0}^{b-1} v_j \left[\cos(2\pi f_1 nj) - i\sin(2\pi f_1 nj)\right]| = |\frac{2}{b}\sum_{j=0}^{b-1} v_j e^{-i2\pi f_1 nj}|, \qquad (1.3)$$

with b as the number of sample points, v_j as the calculated discrete output voltage of the model in the time domain and n as the numerator for higher harmonic voltage responses. Due to their different parities, odd (Y_{2i+1}) and even (Y_{2i}), higher harmonics can show different sensitivities and therefore a different progression [47]. The amplitudes of these higher frequency responses, the so called higher harmonics Y_n, are further used for process characterization. Please note that there are also other options to analyze the nonlinear frequency response, e.g. via Volterra series, which also yield phase shifts [59]. However, an approach based on the widely applied method of THD, which analyses only the amplitude [60], is used here. It should be noted, that in contrast to THD or also EIS, the voltage response is not normalized. This allows electrochemists to better practically interpret the response signal.

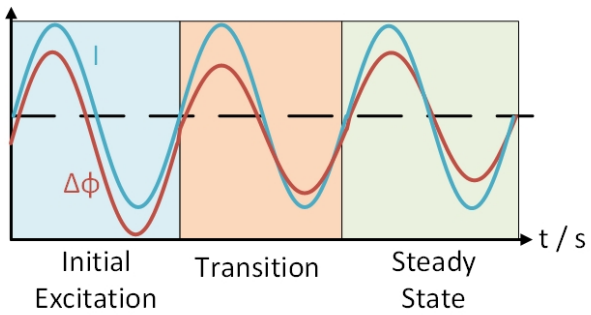

Figure 1.8.: Schematic illustration of transition of the signal response from transient to steady-state behavior.

Once a complex system is excited with a sinusoidal input, it will reach a (dynamic)

steady-state after a certain time [68]. This is shown in Figure 1.8 for the systems output (red curve), reaching for a steady-state and the systems periodic current input (blue curve) in a steady state. Therefore, one can distinguish between the initial time dependent response (transient response) and the periodic, i.e steady-state, response of the system. Since NFRA on LiB is pioneering work, different evaluation approaches were investigated for the evaluation of higher harmonic voltage responses during the last years and thus within this thesis. In Chapter 2 and Chapter 4, the root mean square (rms) of the first two harmonics, and in Chapter 3 and Chapter 5, corresponding to earlier works, the sum of the first eight higher harmonics, both shown in equation 1.4 and equation 1.5, respectively, are investigated.

$$Y_{rms} = \sqrt{\frac{\sum_{i=2}^{3} Y_n^2}{2}} \tag{1.4}$$

$$\sum_{n=2}^{9} Y_n \tag{1.5}$$

Future studies should focus on the rms representation as it is a common and established measure in metrology. In all chapters, focus additionally is laid on the first two higher harmonics. Further, the specific evaluation form is given in the corresponding chapter.

1.3. Modeling of Lithium-Ion Batteries

To fully understand processes within a battery with a novel dynamic measurement technology, modeling is essential. Therefore, a general overview of modeling Lithium-ion batteries is presented.

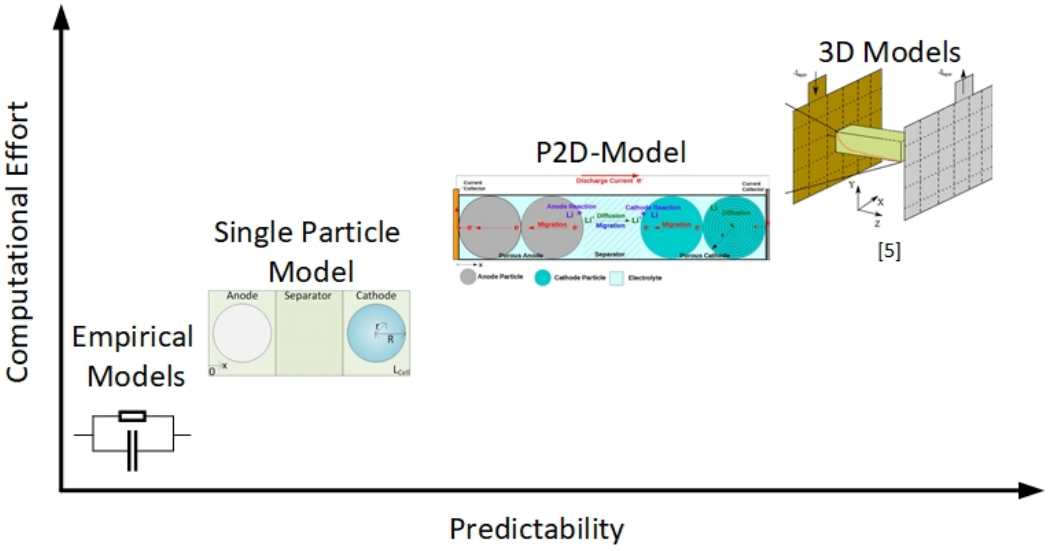

Figure 1.9.: Schematic illustration of the predictability and computational effort of various kinds of battery models [4].

In Figure 1.9, predictability and computational effort of different kinds of battery models are shown. The simplest models are empirical models, so called Equivalent Circuit Models (ECM). ECM need low computational effort and can easily be used to fit simulations to measurement results, i.e. using EIS, which enables an immediate parameter estimation [69]. Nevertheless, ECM are ambiguous in the assignment of electric circuit components to physical processes and are limited to linear processes as they consist of linear elements [10]. More complex, continuum models, are a more feasible alternative to get deeper insight into the cell. Doyle et al. have been the first to introduce a continuum model, known as the Newman-model, based on the theories of porous electrodes and concentrated solutions for cells with a binary electrolyte [70]. In order to simulate dynamic measurements with such physicochemical models, the charging and discharging of double layers has to be included. This has been implemented by Ong et al. [71] and later by Legrand et al. [5].

The simplest version of this model is the Single-Particle (SP) model, where Ohmic losses in the electrodes and electrolyte are neglected. The more complex P2D model uses the battery width as first dimension and the active material particles as second

dimension. For both dimensions, partial differential equations are discretized and solved, thereby significantly increasing both, the predictability and complexity.
By further increasing the number of dimensions considered, i.e. 3D models [4] (or the level of detail, i.e. Monte Carlo- and kinetic Monte Carlo model [72]), the predictability can be enhanced. Due to the computational effort, such models are out of scope of this thesis. Focus is laid on SP and P2D models for this first model-based assessment of NFRA.
All of the above mentioned models commonly deal with liquid electrolyte cells. Next generation ASSB are rarely analyzed by model-based approaches despite the obvious advantages of modeling, e.g. identifying the state of such cells and optimizing cell design. Efficient modeling and excellent understanding of processes in the cell are necessary to fully understand and predict cell behavior and to enable rigorous optimization of cell design. If instead of a binary electrolyte, a Single-Ion-Conducting (SIC), solid electrolyte cell is modeled, adaptions to the aformentioned models have to be made. Becker-Steinberger et al. [73] and Landstorfer et al. [74] presented a 1D model, which models transport processes as a Nernst-Planck flux. Focus is laid on the investigation of the double-layer structure at the solid/electrolyte interface. Bates et al. [75] simulated discharge curves with a 2D model implementing an additional heat flux due to reaction heat. Further, Danilov et al. [76] modeled the transport processes within the SIC electrolyte based on binary electrolyte equations, where instead of negative ions, defects in the lattice move. All models are applied to investigate thin film ASSB and do not focus on elucidating the fundamental differences of cells with a binary and SIC electrolyte.

1.4. Scope of this Work

This thesis aims for in-depth analysis of LiB cells, their processes and corresponding dynamic behavior. The focus of this thesis is laid on a model-based interpretation and understanding of processes in LiB with NFRA, since the modeled processes are well known and the resulting response of higher harmonics can be deeply analyzed and interpreted.
In a first step, in Chapter 2, basic processes of electrochemical systems, such as reaction and diffusion, are analyzed with NFRA and compared to the common and linear

EIS. In Chapter 3, a P2D-battery model is used to investigate the general applicability of NFRA on current generation LiB. Concerning NFRA, it is important to note that the steady-state may change due to an excitation with a high current amplitude. It is thereby possible to distinguish between the initial excitation (transient behavior) and the steady-state. Concerning investigations in Chapter 3, the transient behavior of the battery is investigated, thereby conducting process characterization via parameter variation.

As the formation and continuous growth of the SEI is one of the main ageing processes, NFRA is used to enhance understanding of the impact of the SEI on the dynamic behaviour of the cell [43]. Thus, in Chapter 4, the SEI is included in a SP model. NFRA on the cell is thereby investigated in the transient and steady-state via parameter variation. Focus is further laid on identification of the nature of the kinetics of the transport process of Lithium-ions across the SEI/electrolyte interface.

Within Chapter 5, a P2D model is extended towards next generation ASSB with a SIC electrolyte, as they are one of the most promising future battery designs. NFRA is thereby used to point out differences between current and next generation batteries and shows benefits of this future design.

Focus and structure of the thesis is shown in Figure 1.10.

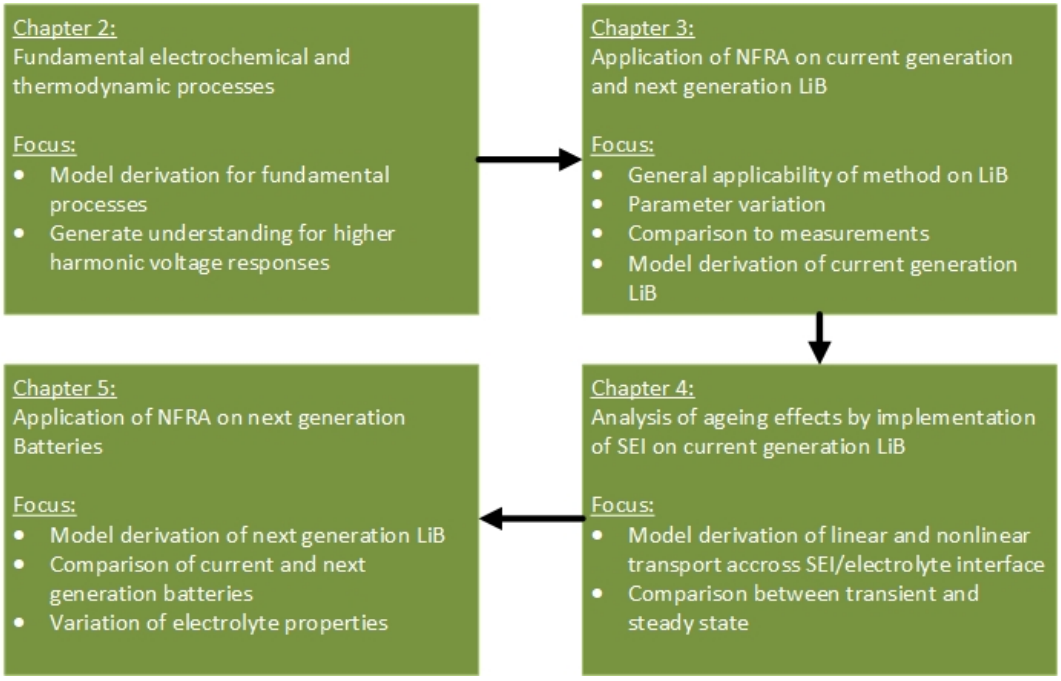

Figure 1.10.: Schematic illustration of the structure of this thesis.

2 Fundamental Processes and Higher Harmonic Voltage Responses[1]

Safety and performance of electrochemical technologies, such as batteries, electrolysers and fuel cells is essential to accelerate the change towards green and renewable energies and towards sustainable production of chemicals via power-to-x. To fulfil this ambitious goal, exact characterization of processes within the previously mentioned cells and their electrodes is needed. Dynamic electrochemical analysis offers the advantage to separate slow from fast processes, and thus an in-depth study and more information of single processes, compared to steady-state techniques such as Tafel slope interpretation. It is thus frequently applied in electrochemistry [36, 77]. Currently, one of the most popular dynamic electrochemical analysis and state diagnosis methods is EIS. This analysis technique is limited to a linear excitation of the investigated system as previously described.

Within this chapter, it is aimed to deliver a basic guideline to enhance interpretation and usage of NFRA via illustrating the nonlinearity using simple fundamental models. The effect of fundamental processes in electrochemical cells on NFR spectra is first analyzed using a most basic electrochemical reaction. Subsequently, the often encountered limited reactant availability, due to slow diffusion, is analyzed, and their impact on NFR is shown. Then the interaction of both processes is studied. In a next step, coupling of electrode reactions is investigated. Further, analysis of sensitivity of the spectra to electrode parameters gives the reader an idea on how parameters and their changes, e.g. due to ageing, impact the spectra. In detail, a variation of characteristic parameters, such as double layer capacitance, excitation amplitude and exchange current density, is conducted.

[1] Parts of this chapter have been published in: Understanding Nonlinearity in Electrochemical Systems, European Physical Journal Special Topics, 227, 2617-2640, 2019 [13].

2.1. Evaluation of NFRA

A detailed description of the working principle of NFRA is provided in Chapter 1. Within this Chapter, the second Y_2 and third Y_3 individual harmonics as well as the root mean square of the first two harmonics Y_{rms}, shown in equation 1.4, are used. Here, the rms instead of the sum of all higher harmonics, or the square root of the squares of the higher harmonics is used, because the rms is a well known measure in metrology and electrical engineering, also for THD [60], and it gives a sound mean value of overall nonlinearity of a system. As the rms requires division by the number of higher harmonics, comparability of rms values will be only given if the same number of higher harmonics is used. As explained in the following, Y_2 and Y_3 are recommended. The amplitudes are chosen so that nonlinear responses for Y_2 and Y_3 are visible, but all further higher harmonics, i.e. n>3 are negligible. This prevents interference of the signals [54]. Please note that, if the excitation signal contains nonlinearities, all harmonics can be influenced. 20 continuous sinusoidal cycles are calculated in this study and the data is extracted from the last cycle to guarantee the dynamic equilibrium of the system.

Tangent Method

Changes of parameters can significantly influence NFR spectra. Therefore, a method which can be generally applicable to gather and compare characteristic values of the spectra is introduced. In this case it is the tangent method.

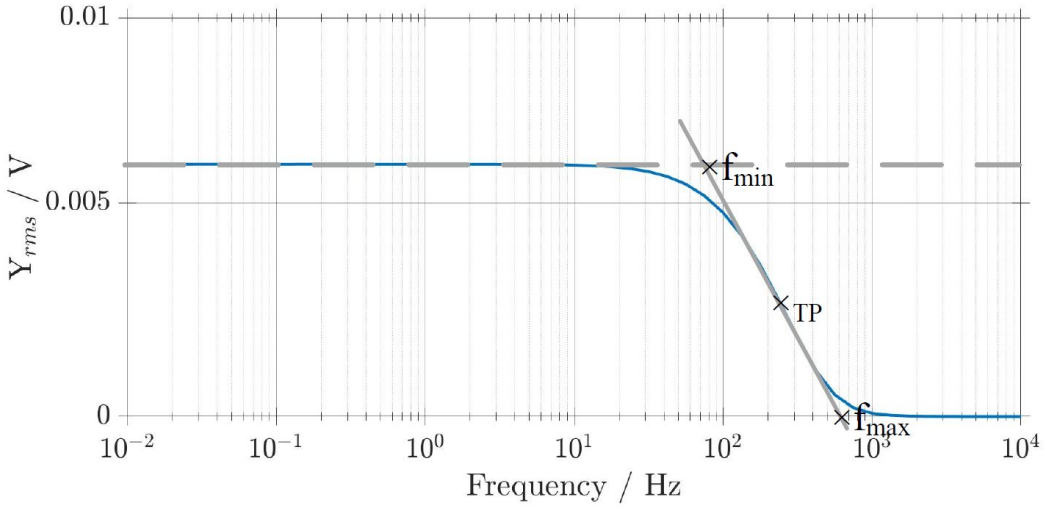

Figure 2.1.: Tangent method for simulated Y_{rms} with the reference case simulation parameters from Table 2.1.

The tangent method is a standard technique in control engineering for identification and analysis of dynamic systems. Control parameters, respectively characteristic values, of the system are gained using the tangent method. Characteristic time periods of the control system are identified with this method. As the shape of a NFR spectrum resembles the typical shape of a step response of a dynamic control system, the tangent method is applied in this study for the characterization of NFR spectra. The tangent method is used for each suitable simulation for the calculation of characteristic parameters of NFRA within this Chapter. Thereby, the characteristic frequencies f_{max}, f_{min} and the turning point TP, which identify and separate specific regions in the NFRA, are recorded, as shown in Figure 2.1.

2.2. Modeling of Fundamental Processes

Focus of this research is laid on the understanding of the excitation of higher harmonics. Therefore, a reaction process according to Butler-Volmer kinetics and a diffusion process according to Fick's law are investigated in a model-based approach. For the sake of simplicity, further mass transport processes, such as migration, convection and electro-osmotic drag, heat transport as well as complex surface processes and adsorption or desorption are ignored.

All functions used within this work are embedded in MATLAB, the spatial discretization of the partial differential equations used for simulating diffusion is implemented with a finite volume approach, and time derivatives are solved with an ode-solver. A spatial discretization is chosen that is sufficiently fine to guarantee a mesh independent solution. Computation time was typically below 15 minutes. A base case parameter set is provided in Table 2.1, with the initial concentration of reactant A $c_{A,0}$, the specific surface area a_s. Further, reference values for double layer capacitance $C_{\mathrm{DL},0}$, exchange current density $i_{0,0}$, symmetry factor α, diffusion coefficient D_0, AC current density $I_{AC,0}$, thickness d as well as ambient temperature T are used in this study.

parameter:	value:	unit:
$c_{A,0}$	$1.5 \cdot 10^{4}$	mol m^{-3}
a_s	$1.5 \cdot 10^{5}$	m^{-1}
$C_{DL,0}$	0.2	F m^{-2}
$i_{0,0}$	10	A m^{-2}
α	0.5	-
D_0	$1.0 \cdot 10^{-12}$	m^2 s^{-1}
$I_{AC,0}$	400	A m^{-2}
d	$50.0 \cdot 10^{-6}$	m
T	300	K

Table 2.1.: Simulation parameters.

Since this model-based study targets to explain the fundamentals of the excitation of higher harmonic voltage responses, a one step redox reaction is assumed as a base case scenario:

$$\mathrm{A} \rightleftharpoons \mathrm{A}^{+} + \mathrm{e}^{-} \tag{2.1}$$

An unlimited reservoir for A^{+} and a constant activity of 1 are assumed. The reservoir of A on the other hand is limited. A change of its activity a_A leads to a change of the open circuit potential of the system $\Delta\phi^0$, implemented via a Nernst-approach, given in equation 2.2. This activity dependence of the potential is measured to a neutral reference and for the simple priorly described redox reaction it can be expressed as follows:

$$\Delta\phi^0 = \Delta\phi^{00} + \frac{\mathrm{R}T}{\mathrm{F}} \ln \frac{1}{a_A}, \tag{2.2}$$

with the standard potential $\Delta\phi^{00}$, Faraday constant F, ideal gas constant R and temperature T. The activity a_A can be expressed by the corresponding concentration c_A and its standard equilibrium concentration $c_{A,0}$, if an ideal system with an activity coefficient of one is investigated, as shown in the following:

$$a_A = \frac{c_A}{c_{A,0}}, \tag{2.3}$$

with:

$$\Delta\phi^0 = \Delta\phi^{00} + \frac{\mathrm{R}T}{\mathrm{F}} \ln \frac{1}{\frac{c_A}{c_{A,0}}} \tag{2.4}$$

The priorly described one step reaction, shown in equation 2.1, can be modeled via a Butler-Volmer equation, which, according to Bard et al. [36], further can be expressed

as follows, including the already made assumptions:

$$j_\mathrm{f} = a_s i_0 \left(\frac{c_A}{c_{A,0}} \exp\left(\alpha \frac{\eta \mathrm{F}}{\mathrm{R}T} \right) - \exp\left(-(1-\alpha) \frac{\eta \mathrm{F}}{\mathrm{R}T} \right) \right), \tag{2.5}$$

with the Faradaic volumetric reaction current j_f, specific surface area of the electrode a_s, exchange current density i_0 and overpotential η.

The overpotential η used in the previous equation is defined as:

$$\eta = \Delta\phi - \Delta\phi^0, \tag{2.6}$$

with the potential gradient across the interface $\Delta\phi$.

Additionally to the ion generation rate due to Butler-Volmer kinetics, a total volumetric current j_tot leaves or enters the interface, resulting in the charge balance:

$$a_s \cdot \mathrm{C_{DL}} \frac{\partial \Delta\phi}{\partial t} = j_\mathrm{tot} - j_\mathrm{f}, \tag{2.7}$$

with the electric double layer capacitance C_DL. The current per electrode volume j_tot, thereby equals the externally applied sinusoidal current per geometric area of electrode per electrode thickness d with amplitude I_{AC}, as shown in the following equation:

$$j_\mathrm{tot} = \frac{I_{AC}}{d} \sin(2\pi f t), \tag{2.8}$$

As species are consumed or produced at the interface, reactant and product species need to diffuse to or from the interface before or after reaction, respectively. If, a volumetric current is transferred to a current across an interface, the specific surface area a_s is used. Diffusion impacts the concentration at the surface, and by this both, the overpotential, e.g via a concentration dependent Butler-Volmer curve, i.e, kinetics, and the open circuit potential via the Nernst equation. Both, open circuit potential and overpotential impact electrode potential and thus dynamic response of potential to current.

Typical diffusion processes in cells are planar diffusion, e.g. occurring between the electrodes in the electrolyte, or spherical diffusion in spherical electrode particles, as observed in insertion electrodes of batteries, such as LiB, where the reduced species is stored and diffuses in the active material particles. Diffusion processes are imple-

mented according to Fick's law. Within this research, differences between planar and spherical diffusion, shown in equation 2.9 and 2.10, respectively, are analyzed.

$$\frac{\partial c_A}{\partial t} = \frac{\partial}{\partial x}\left(D\frac{\partial c_A}{\partial x}\right), \tag{2.9}$$

$$\frac{\partial c_A}{\partial t} = \frac{1}{r^2}\frac{\partial}{\partial r}\left(Dr^2\frac{\partial c_A}{\partial r}\right), \tag{2.10}$$

with the time t, diffusion coefficient D and spacial coordinates x and r, respectively. Concerning planar and spherical diffusion, a maximal diffusion length, which corresponds to the thickness d, is set, respectively. In Figure 2.2, a schematic illustration of the implemented spherical and planar diffusion with the corresponding diffusion length d is shown.

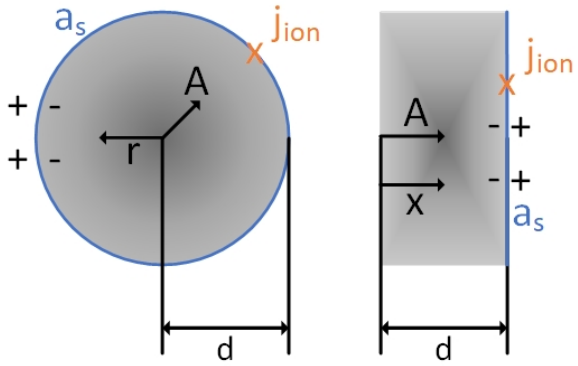

Figure 2.2.: Schematic illustration of the implemented spherical diffusion and planar diffusion of species A to the electrochemically active surface (blue), where the reaction j_f takes place.

Boundary conditions are provided in the following:

$$\frac{\partial c(0)}{\partial r} = \frac{\partial c(0)}{\partial x} = 0, \frac{\partial c(d)}{\partial r} = \frac{\partial c(d)}{\partial x} = \frac{j_f}{Da_sF} \tag{2.11}$$

Model for impact of reaction process

In a first step, focus is laid on an investigation of the reaction process and the nonlinear response of $\Delta\phi$. For this purpose, influences of concentration changes are fully neglected. Therefore c_A is assumed to be constant with $c_A = c_{A,0}$ and the previously derived and described equations can be simplified as follows.

For the Nernst-equation, shown in equation 2.2, a constant concentration $c_{A,0}$ leads

to a constant open circuit potential $\Delta\phi^0$:

$$\Delta\phi^0 = \Delta\phi^{00} = constant \tag{2.12}$$

Additionally within the Butler-Volmer equation, shown in 2.5 the priorly concentration dependent forward reaction can be simplified to a concentration independent reaction:

$$j_f = a_s i_0 \left(\exp\left(\alpha \frac{\eta \mathrm{F}}{\mathrm{R}T} \right) - \exp\left(-(1-\alpha) \frac{\eta \mathrm{F}}{\mathrm{R}T} \right) \right). \tag{2.13}$$

All other equations remain valid without simplifications.

Model for impact of diffusion process

In a second step, it is aimed to understand in-depth the excitation of higher harmonics due to diffusion. The model as it was derived in section 2.2, without further simplifications is used. However, to isolate the influence of the diffusion process, at this point, the effect of reaction via Butler-Volmer kinetics, i.e. η on the nonlinear response and analyze the higher harmonic voltage response of $\Delta\phi^0$, is neglected. While both, spherical and planar diffusion are analyzed, spherical diffusion is defined as the reference scenario.

Model for impact of coupled processes

In a last step, the interaction and coupling of reaction and spherical diffusion are investigated as they are inevitably coupled in electrochemical systems. Also, the diffusion impact on η will be elucidated. Here, the complete model, derived in section 2.2, without further simplifications is used.

2.3. Results and Discussion

In-depth understanding of the excitation of higher harmonics is generated and discussed within this research. For this purpose, the root mean square Y_{rms}, calculated with the first two higher harmonics Y_{2-3} as well as individual harmonics Y_2 and Y_3 are investigated, as previously stated; impedance spectra, calculated with small excitation amplitude, are provided where helpful for the discussion. First, the reaction process is analyzed, then different diffusion processes are investigated followed by a coupling of reaction and diffusion. To quantitatively evaluate and compare the spec-

tra characteristic, parameter specific information gathered from the tangent method are shown and discussed. The tangent method is described in Figure 2.1. It is to the awareness of the author that multiple possibilities to quantify changes in spectra exist. Nevertheless, the tangent method is a suitable method to gather characteristic frequencies and intensities of these spectra and evaluate changes in the symmetry.

2.3.1. Impact of Reaction

In this first section, it is aimed to systematically and thoroughly characterize the priorly described reaction process. Therefore the general model from section 2.2 with the simplification from section 2.2 is used. In Figure 2.3, simulations with the base case parameter set given in Table 2.1 and a variation of the AC excitation amplitude between 0.5 $I_{AC,0}$ and 2.0 $I_{AC,0}$ are shown. If not mentioned otherwise, the base case parameters are chosen for simulation. The NFR spectrum with an excitation amplitude of 1.0 $I_{AC,0}$ is referred to as reference simulation in the following and is marked with an asterisk. Additional to NFR simulations, EIS, simulated with an excitation amplitude of 0.1 $I_{AC,0}$, guaranteeing linear behavior of the system, is provided. In Figure 2.3 a), three frequency ranges with characteristic nonlinearities are identified for Y_{rms}, applying the tangent method, described in section 2.1. The general shape resembles that of a bode plot of an EIS, its high frequency value being zero and low frequency value being constant. For high frequencies greater than the characteristic frequency f_{max} of 600 Hz (dash-dotted line in Figure 2.3 a)), NFR have negligible intensity. In the frequency range below 600 Hz up to the second characteristic frequency f_{min} of 75 Hz (dashed line in Figure 2.3 a)), NFR increase monotonously. One additional characteristic feature is identified in this frequency range, the turning point (TP) of the spectrum at 240 Hz (see blue circle in 2.3 a)). The characteristic frequency of the turning point is marked in each NFR spectrum in the corresponding plot color. For frequencies smaller than 75 Hz, NFR have an almost constant value of $Y_{rms}(f_{min})$. As f_{min} and f_{max} separate the three characteristic frequency regions, they are used in the following to separate and separately discuss the three regions in-depth. The three characteristic features, namely f_{max}, f_{min} as well as $Y_{rms}(f_{min})$, are identified for each simulated parameter variation concerning the reaction process for the root mean square Y_{rms} and shown in Figure 2.10, 2.11 and 2.12 at the end of this section.

The change of these characteristic features in dependence of the specific parameter variations is discussed and concluded on at the end of this section, as well. In Figure 2.3 b), the individual higher harmonics Y_2 and Y_3 are analyzed. Hereby, it is highly interesting to notice that only the third harmonic Y_3 is excited in the overall frequency range. The second harmonic Y_2, however, is not excited. Thus, it is deduced that one single electrochemical reaction implemented as previously described only impacts the third harmonic Y_3. Further, the same three characteristic frequency ranges as well as the same frequencies of the features f_{min}, f_{max} and TP, as for Y_{rms} are identified for the individual higher harmonic Y_3. In the additionally provided impedance spectrum, shown in Figure 2.3 c), a semi circle corresponding to the electrochemical reaction with a characteristic frequency of 320 Hz, also marked for the NFR spectrum (black line), can be seen. This is in agreement to the literature [41].

In the following, the focus is laid on a qualitative description and analysis of the impact of the particular parameters on the NFR spectra, such as the excitation amplitude.

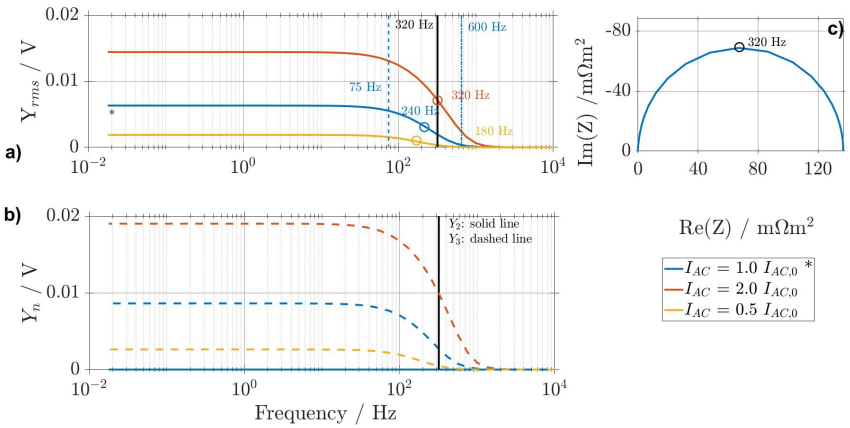

Figure 2.3.: Simulated NFR for the reaction model with a variation of the AC excitation amplitude for a) Y_{rms}, b) individual harmonics Y_2 and Y_3 and c) EIS. The reference case simulation with parameters from Table 2.1 is marked with an asterisk. f_{min} is marked by a dashed blue line and f_{max} is marked by a dash-dotted blue line, both for the reference case simulation.

Increasing the sinusoidal excitation amplitude impacts Y_{rms}, shown in Figure 2.3 a), as well as the individual higher harmonics, shown in Figure 2.3 b). For the higher AC excitation of 2.0 $I_{AC,0}$, f_{min}, f_{max} shift towards higher frequencies and $Y_{rms}(f_{min})$ increases due to higher nonlinearities for the higher excitation amplitude. The characteristic frequency of TP shifts from 240 Hz for an excitation of 1.0 $I_{AC,0}$ to 320 Hz for 2.0 $I_{AC,0}$. If the excitation amplitude is lowered to 0.5 $I_{AC,0}$, f_{min}, f_{max} shift to-

wards lower frequencies and $Y_{rms}(f_{min})$ decreases due to lower nonlinearities. The characteristic frequency of TP shifts from 240 Hz for an excitation of 1.0 $I_{AC,0}$ to 180 Hz for 0.5 $I_{AC,0}$. Therefore, a dependency of the characteristic features of the spectra on AC excitation amplitude can be deduced from this study for the simple reaction model. However, amplitude changes excite no novel characteristic features or qualitative change in the NFR spectrum. In Figure 2.3 b), the individual higher harmonics Y_2 and Y_3 are analyzed for an increased AC amplitude. Increasing the AC excitation increases the intensity of the third harmonic as well $Y_{rms}(f_{min})$ and increases the characteristic frequencies, as well but does not lead to an excitation of Y_2.

Understanding the features of the NFR spectra and their dependence on the single processes is essential for a sound future interpretation of such spectra. As the best way to see the impact of single processes is by accelerating or slowing down each process via changing of its parameters, a systematic parameter sensitivity study is conducted in the following.

Based on the above given reference NFR simulation at 1.0 $I_{AC,0}$, parameter variations, for the double layer capacitance C_{DL} as well as the exchange current density i_0, are shown. Further, the influence of the symmetry factor α is investigated. DC currents or cell potentials that lead to a reaction and current are frequently used in EIS research to characterize the cell and processes under operation. Therefore, the impact of an additional DC current and its impact on NFR spectra is also elucidated.

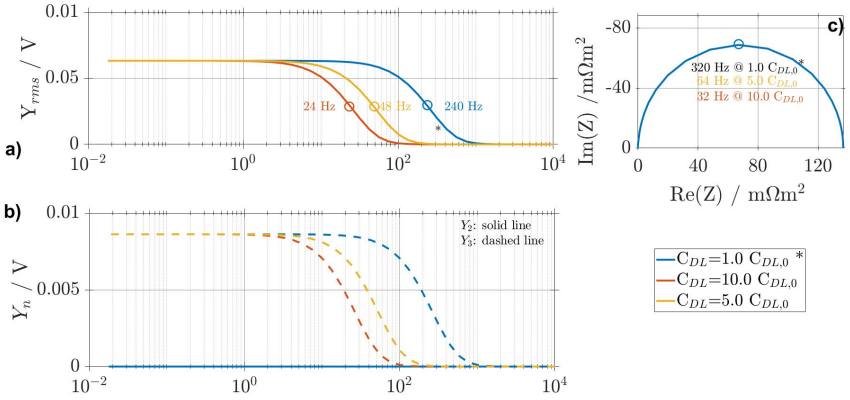

Figure 2.4.: Simulated NFR for the reaction model with a variation of the double layer capacitance C_{DL} and AC excitation amplitude for a) Y_{rms}, b) individual harmonics Y_2 and Y_3 and c) EIS. The reference case simulation with parameters from Table 2.1 is marked with an asterisk.

In Figure 2.4, the influence of a variation of the double layer capacitance C_{DL} on Y_{rms} and EIS is shown. With increasing double layer capacitance C_{DL}, the dynamic answer of the reaction becomes slower and the characteristic frequencies f_{min} and f_{max} shift towards lower frequencies. Overall, this shift is linear, as it can be seen for the frequency of the turning point. This is similar to EIS simulations. By changing the double capacitance C_{DL} with one order of magnitude, the frequency of the turning point also shifts by one order of magnitude.

Whereas the double layer capacitance C_{DL} impacts the characteristic frequency range of the reaction process in the spectra, it does not impact the absolute values at high and low frequencies. Therefore, $Y_{rms}(f_{min})$ stays constant. Concerning individual harmonics, also here only Y_3 is excited. This feature is not affected by a change of the double layer capacitance C_{DL}. Thus, the previously described changes of the characteristic features for Y_{rms} are similar for Y_3, as only Y_3 contributes to Y_{rms} in this case.

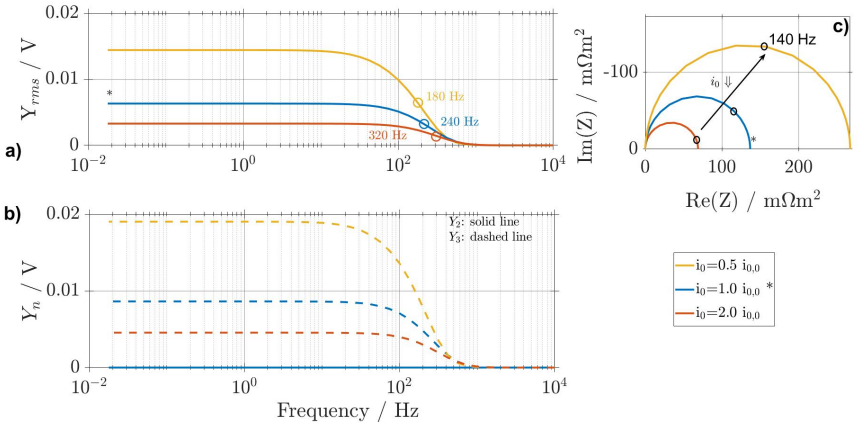

Figure 2.5.: Simulated NFR for the reaction model with a variation of the exchange current density i_0 for a) Y_{rms}, b) individual harmonics Y_2 and Y_3 and c) EIS. The reference case simulation with parameters from Table 2.1 is marked with an asterisk.

In the following, a variation of the exchange current density i_0 and its influence on nonlinear voltage responses is investigated. The simulation results for Y_{rms} are shown in Figure 2.5 a). With decreasing exchange current density i_0, nonlinear voltage responses increase nonlinearly, as well indicated by $Y_{rms}(f_{min})$. Further, the characteristic turning point as well as f_{min} and f_{max} move towards lower frequencies. For an increase of the exchange current density i_0 this is vice versa. This can analogously be observed for the impedance in Figure 2.5 c). A shift of the characteristic frequency towards lower frequencies and a higher impedance in general indicates a slower process

with a higher resistance i.e for a lower exchange current density i_0. Concerning individual harmonics, again, only the third harmonic Y_3 is excited and therefore changes of the characteristic feature of Y_3 are again, similar to Y_{rms}. Overall, the information accessed by NFRA and EIS for a variation of the exchange current density i_0 is comparable.

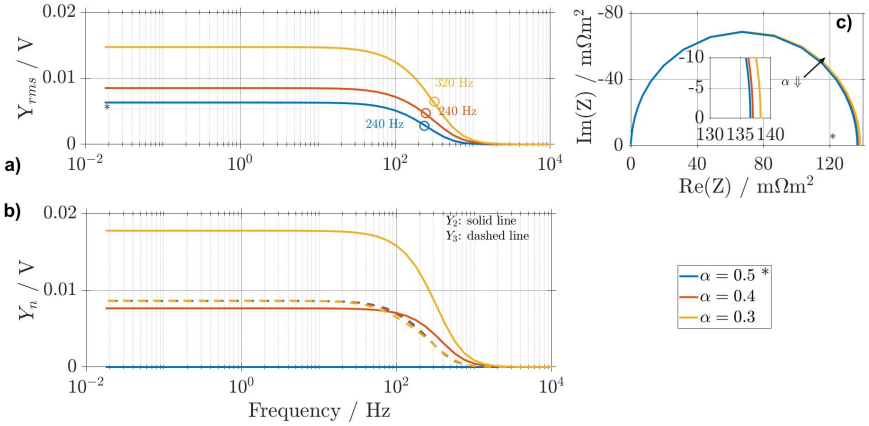

Figure 2.6.: Simulated NFR for the reaction model with a variation of the symmetry factor α for a) Y_{rms}, b) individual harmonics Y_2 and Y_3 and c) EIS. The reference case simulation with parameters from Table 2.1 is marked with an asterisk.

In the following, the influence of the symmetry of the electrochemical reaction on NFRA by a variation of the symmetry factor α is investigated. In general, decreasing and increasing the symmetry factor by a certain value with reference to 0.5 will lead to the same excitation of higher harmonics as shown in the Appendix A.1 in Figure 2.17 for $\alpha = 0.4$ and $\alpha = 0.6$. Therefore, focus is laid on decreasing of the symmetry factor α. A decreasing symmetry factor α leads to higher nonlinear voltage responses, as shown in Figure 2.6 a) by an increased $Y_{rms}(f_{min})$. In combination with the simulation in the Appendix it can be concluded that not the absolute value of α determines the excitation of higher harmonics but its deviation from 0.5.

An investigation of the individual harmonics Y_2 and Y_3 shows that voltage responses of the third harmonic Y_3 are barely affected by a change of the symmetry factor, but as soon as the reaction becomes asymmetrical for $\alpha \neq 0.5$, Y_2 is excited. It has a similar curve shape with a constant but alpha-dependent value $Y_2(f_{min})$ at low frequencies and a smooth decrease to zero at higher frequencies greater than f_{max}. This characteristic information cannot be accessed by EIS, shown in Figure 2.6 c), where a decreasing symmetry factor α only leads to a minorly increased semi-circle corresponding to an increased linear output as for a priorly observed decreased exchange

current density i_0. The excitation of Y_2 further causes the turning point of Y_{rms} and the characteristic frequencies to move to higher frequencies, if α is smaller than 0.4. For a variation of the symmetry factor α, a significant advantage of NFRA compared to conventional EIS can be observed, a symmetry change causes a specific excitation of the second harmonic Y_2. This phenomenon is further investigated in the following.

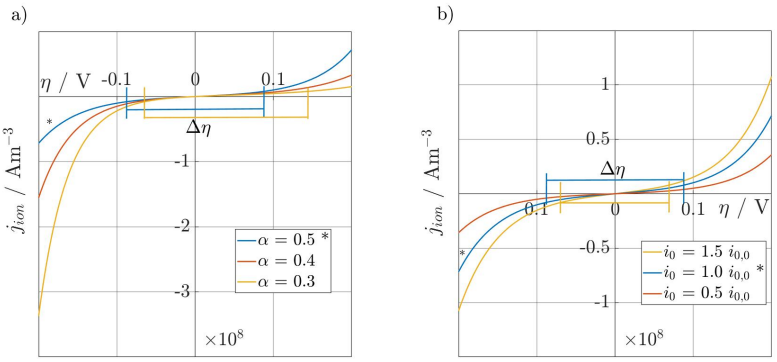

Figure 2.7.: Butler-Volmer kinetics for a) variation of symmetry factor α and b) exchange current density i_0 with reference values according Table 2.1. The reference case is marked with an asterisk.

In Figure 2.7 a), the change of the current-voltage relation according to the Butler-Volmer equation due to a change of α is shown. Additionally, the maximal overpotentials $\Delta\eta$ which are excited for the reference case and for $\alpha = 0.5$ are shown. For a perfectly symmetric reaction, with $\alpha = 0.5$, only Y_3 is excited and η changes symmetrically around 0. If α is decreased, the corresponding curve changes its characteristic progression and becomes asymmetrical, as shown in Figure 2.7 a): The slope increases on the left hand side of the y-axis and decreases on the corresponding right hand side. This causes a shift of the mean overpotentials and $\Delta\eta$ to the right for a decreased α, thereby leading to an excitation of Y_2. This unique feature of NFRA suggests that NFRA might also allow to determine α without recording current-voltage curves.
In Figure 2.7 b), the change of the current-voltage relation according to the Butler-Volmer equation for a change of the exchange current density i_0 is shown for comparison. Again, maximal overpotentials $\Delta\eta$ for the reference case and the deviation from it are shown. With increasing i_0, the slope of the plotted curve becomes steeper. Both, curve and $\Delta\eta$ stay symmetrical to the potential of 0, making a change in i_0 distinguishable from that of α. Both, oxidation and reduction current, lead to a smaller

$\Delta\eta$ to the higher j_f generation. This explains the decrease of impedance and NFR for a larger exchange current density i_0, as shown in Figure 2.5. If i_0 is lowered, the observed effects are vice versa.

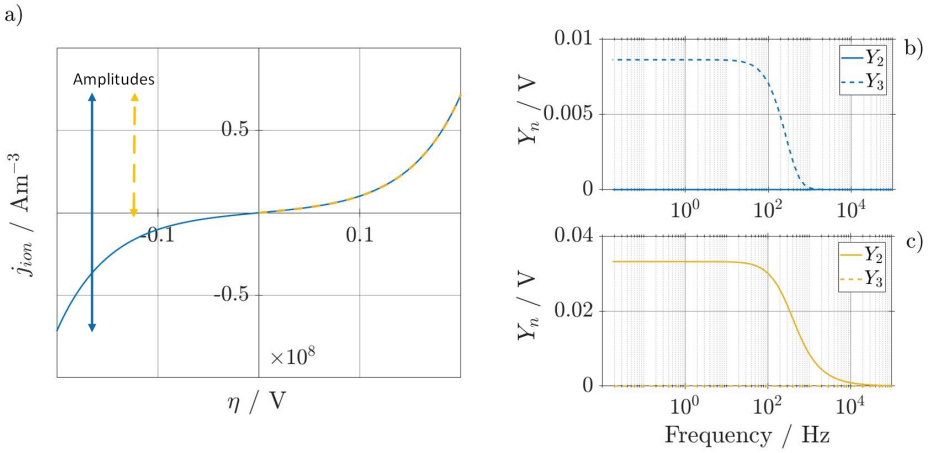

Figure 2.8.: Correlation between shape of current excitation and higher harmonics Y_2 and Y_3 with a) Butler-Volmer kinetics with full (solid) and partial (dashed) sinusoidal excitation of current, b) individual harmonics for sinusoidal excitation and c) individual harmonics for partially sinusoidal excitation.

It is aimed to understand the excitation of the second Y_2 and third Y_3 harmonic in general, as it is an important feature of NFR spectra. Usually, a sinusoidal current (blue curve) is applied to the model, as shown in the following equation.

$$I = I_{AC} \sin(2\pi f t),$$

with the frequency f. As a result, the full range of the symmetric Butler-Volmer curve is employed, resulting in positive and negative potentials. If instead only a partial sinusoidal excitation (yellow curve) is periodically applied to the model, as shown in the following equation, only one branch of the Butler-Volmer equation is employed, resulting in a correlation of current and potential which is not symmetric to i=0,η=0 any more.

$$I = I_{AC} || \sin(2\pi f t) || > 0$$

This could be the case for completely irreversible reaction or operation with additional DC current. In Figure 2.8 b), individual harmonics Y_2 and Y_3 for the sinusoidal excitation of the system are shown. This results in the well known excitation of Y_3.

In Figure 2.8 c), individual harmonics Y_2 and Y_3 for the partially sinusoidal excitation of the system are shown. It can be seen that in this case only the second harmonic Y_2 is excited. This leads to the conclusion that a nonlinear relation between current and potential which is symmetric to the center causes an excitation of the third harmonic Y_3 and a nonlinear relation between current and potential which is symmetric to the y-axis or which has only positive current and voltage causes an excitation of Y_2. This can be explained with the different parities of the harmonics. Additionally, the excitation of harmonics is not linear since the maximal amplitude of Y_2 is three times as high as the corresponding maximal amplitude of Y_3. For real systems, the relation between current and potential will neither be fully symmetric to the center nor to the y-axis and therefore an excitation of both individual harmonics, Y_2 and Y_3, will both be present, as found in experimental studies [47, 64].

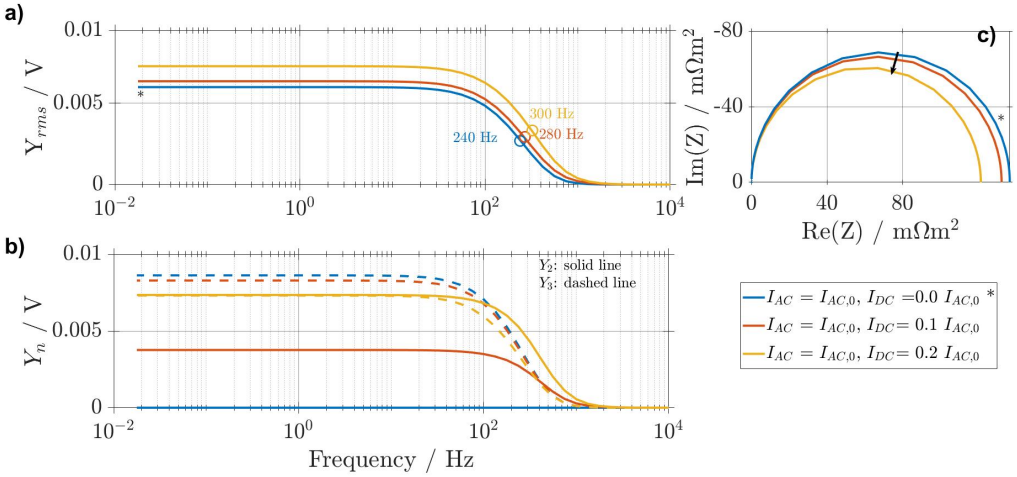

Figure 2.9.: Simulated NFR for reaction model and DC excitation of the cell for a) Y_{rms}, b) individual harmonics Y_2 and Y_3 and c) EIS. The reference case simulation with parameters from Table 2.1 is marked with an asterisk.

Finally, the influence on NFRA for operating a cell under load is investigated by adding a DC excitation. In Figure 2.9 a), Y_{rms} is shown. If an additional DC is applied to the system, Y_{rms} increases nonlinearly and the turning point as well as f_{max} and f_{min} shift slightly towards higher frequencies. Overall, NFR are excited in the same frequency range, but with a higher overall value, again indicated by $Y_{rms}(f_{min})$, as well. To understand this behavior, individual harmonics, shown in Figure 2.9 b), are investigated. With increasing DC current, the operating point shifts farther away from the symmetry point at zero current on the Butler-Volmer curve in Figure 2.7, and

the current oscillates symmetrically around this new value, leading to strong asymmetric current-voltage relation. Therefore, the second harmonic Y_2 is excited. In parallel, the voltage responses of Y_3 decrease. A DC current equals an offset concerning the current j_f in the Butler-Volmer equation and due to the exponential relation between current and potential, a smaller overall change in potential results. Thereby, the linear output and Y_3 decrease. These findings are confirmed by investigation of EIS, shown in Figure 2.9 c), where the corresponding semi-circle becomes slightly smaller with increasing DC current. The characteristic frequency is barely influenced, indicated by the black arrow. Also here, it can clearly be seen that the single higher harmonics yield more information than EIS.

2.3.2. Comparison of Parameter Effects

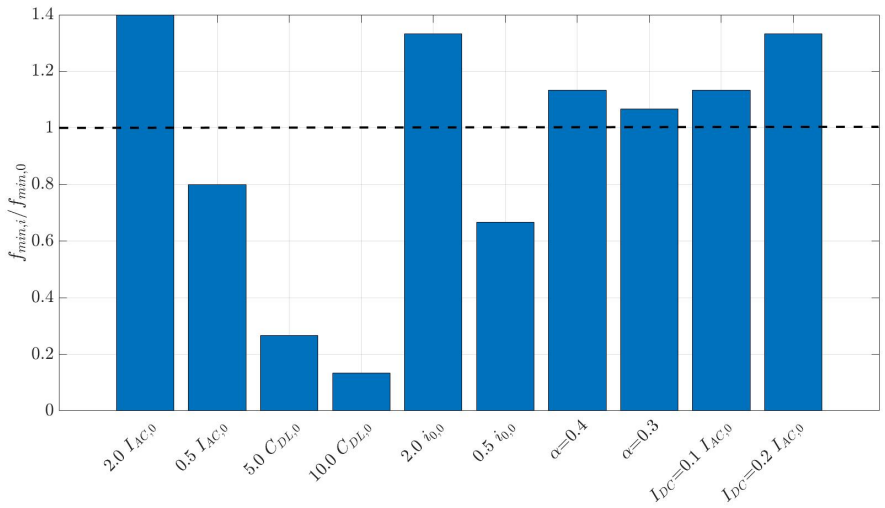

Figure 2.10.: f_{min} relative to the reference case gathered from tangent method; the reference case simulation is marked with a dashed line with parameters from Table 2.1.

In this section, the quantitative and qualitative impact of the various investigated parameters on NFR spectra is compared using the characteristic NFRA values f_{min}, f_{max} and $Y_{rms}(f_{min})$. As priorly discussed, the characteristics f_{min} and f_{max} are used for separation and characterization of process-dependent NFRA frequency regions, and $Y_{rms}(f_{min})$ represents the constant Y_{rms} values in the lowest frequency range. In case that f_{min} and f_{max} are both higher, or lower than the reference value, the reaction process becomes faster, or slower for the corresponding variation of the model parameter, respectively. In the bar plots in Figures 2.10, 2.11 and 2.12, the values of the characteristics relative to the reference case, i.e. $f_{min}/f_{min,0}$, $f_{max}/f_{max,0}$ and

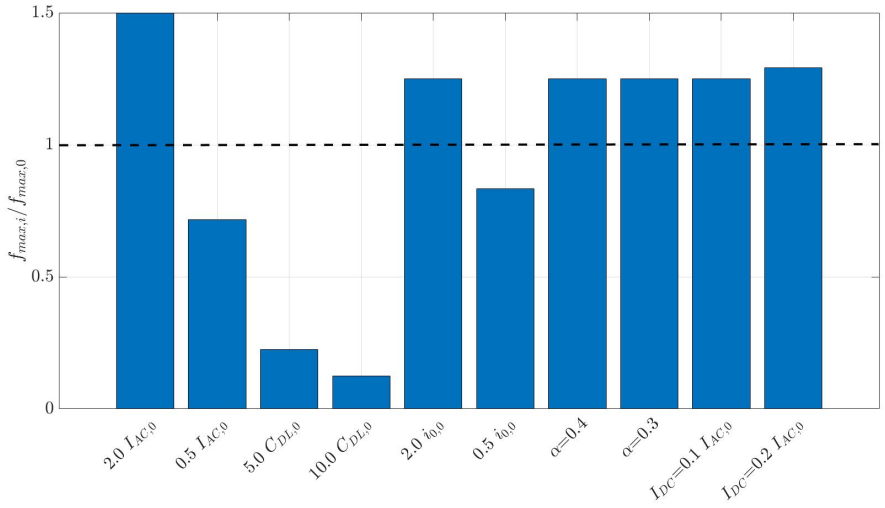

Figure 2.11.: f_{max} relative to the reference case gathered from tangent method; the reference case simulation is marked with a dashed line with parameters from Table 2.1.

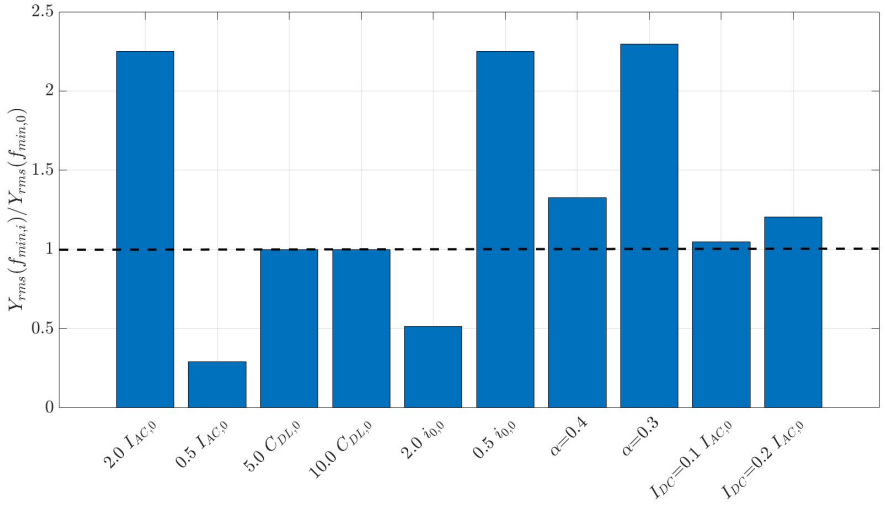

Figure 2.12.: $Y_{rms}(f_{min})$ relative to the reference case gathered from tangent method; the reference case simulation is marked with a dashed line with parameters from Table 2.1.

$Y_{rms}(f_{min})/Y_{rms}(f_{min,0})$ are given. Thus, the values of the reference case are 1 and marked with a dashed line in the corresponding Figures.

It can be seen that for the investigated reaction, a variation of parameters has a strong influence on the characteristics. If the excitation amplitude I_{AC} is increased, all characteristics are increased. The higher amplitudes cause a larger deviation from linear current potential relation and thus stronger nonlinearities. Also, for higher amplitudes, the double layer is charged faster, leading to a faster increase in voltage and reaction and thus to higher frequencies. This impact is vice versa for a decreasing excitation amplitude: $Y_{rms}(f_{min})$ has a lower value, the NFR slope is flatter and f_{min} and f_{max} are at lower frequencies.

A change of the double layer capacitance C_{DL} does not affect the intensity of NFR and therefore, the absolute value $Y_{rms}(f_{min})$ stays constant at the reference value for each variation of the double layer capacitance. However, the frequency characteristics shift as C_{DL} determines the time delay between current and voltage or reaction. For an increase of C_{DL}, the frequencies f_{min}, respectively f_{max}, are at lower frequencies, and thus the reaction process becomes slower.

A variation of the exchange current density i_0, again, influences all characteristics. For increasing the exchange current density i_0 in comparison to the reference case, the overall excited nonlinearities Y_{rms} are lower, as less overpotential is required for the same reaction current. As the reaction can follow current more easily also for fast charges, f_{min} and f_{max} shift to higher values. Adding an additional DC current impacts all characteristics. Both parameters increase the overall excitation of nonlinearities Y_{rms} due to the respective change of symmetry and therefore a corresponding excitation of Y_2. Thus, the slope of NFR between the characteristic frequencies f_{min} and f_{max} is steeper, which shifts these characteristics to higher frequencies.

For a variation of the symmetry factor α, the reaction process changes its symmetry and becomes asymmetric compared to the reference case. Thereby, due to the previously discussed reasons, higher nonlinearities are excited and the corresponding $Y_{rms}(f_{min})$ has a higher value. Both characteristics f_{min} and f_{max} are sensitive to change of the symmetry factor. However, f_{min} is slightly more sensitive to a lowering of the symmetry factor than f_{max}. Here, $Y_{rms}(f_{min})$ is the most impacted characteristic.

To conclude, NFRA characteristics identified in this section using the tangent method are highly sensitive to parameter variations. The given overview should aid future studies in understanding and identifying the reason for experimentally observed changes in NFR spectra. Vice versa, NFR might even be a proper tool of material scientists to tailor certain material properties.

2.3.3. Impact of Diffusion

As the previous section has clearly shown, the impact of reaction on the nonlinear response of the cell and how to interpret the spectra, now focus is laid on the second most important process, diffusion. The excitation of higher harmonics due to planar and spherical diffusion is investigated. At this point, only the impact of sinusoidal current on open circuit potential via consumption or production of species is analyzed, as described in section 2.2. For the full impact of diffusion on open circuit and overpotential it is referred to the next section of the coupling of diffusion and reaction. Please note that spherical diffusion is defined as the reference case.

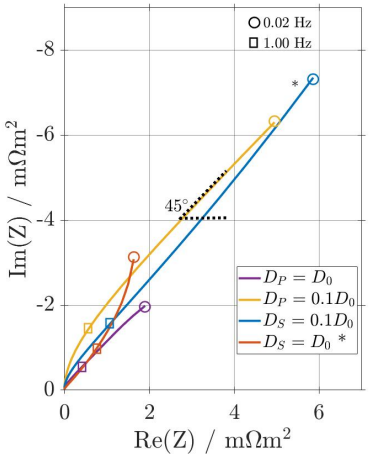

Figure 2.13.: Simulated impedance spectra for planar and spherical diffusion for different diffusion coefficients D_S, D_P. The reference case simulation for spherical diffusion with parameters from Table 2.1 is marked with an asterisk.

First, impedance spectra for the different diffusion processes and for different diffusion coefficients are shown in Figure 2.13. Simulated impedance spectra show characteristic, well known behavior from the literature [78] for the chosen boundary conditions. The models with planar diffusion, with the reference and for a significantly lowered diffusion coefficient, both show the typical slope of 45° at least at low frequencies, as observed by Jacobsen et al. for a planar blocking diffusion impedance

[78]. By decreasing the diffusion coefficient, diffusion slows down, causing a higher impedance at all frequencies. This is observed for spherical diffusion, as well. Spherical diffusion leads to a steeper slope than planar diffusion, which is explained in-depth in the next paragraph and observed by Jacobsen et al. for a spherical blocking diffusion impedance [78]. Further, for the reference case, a transition towards capacitive behavior is visible. If the frequency was decreased further, ideal capacitive behavior would occur. By decreasing the diffusion coefficient by 90 %, this transition is moved to even lower frequencies, not visible in the spectrum. This interpretation is supported by the characteristic time constants:

$$\tau = \frac{d^2}{D}, \tag{2.14}$$

with d being the characteristic length from Table 2.1. It can be seen, that a decreasing diffusion coefficient leads to a higher time constant and therewith a smaller characteristic frequency.

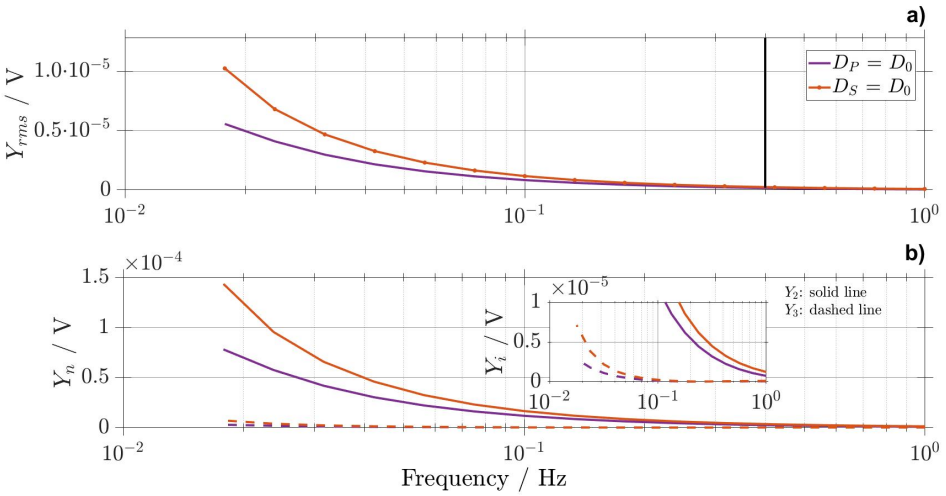

Figure 2.14.: Simulated NFR for planar and spherical diffusion for a) Y_{rms} with a marker (black line) for the lowest frequency with higher harmonic excitation and b) individual harmonics Y_2 and Y_3, with the reference case simulation parameters from Table 2.1.

In Figure 2.14, nonlinear voltage responses for planar and spherical diffusion are shown. The tangent method can not be applied to analyze the obtained NFR spectra, as NFR excited by diffusion do not have the same characteristic progression as NFR excited by a reaction process.

Concerning Y_{rms}, in Figure 2.14 a), no distinct maximum nor turning point is visible, only a continuous, increase of exponential shape of NFR with decreasing frequency

can be observed, starting at a frequency of ca. 0.4 Hz. Therefore, neither f_{max} nor f_{min} can be determined. Overall, a lower frequency range compared to the reaction process is excited. The characteristic time constant according to equation 2.14 is at 200 s corresponding to 0.005 Hz, which indicates that nonlinear responses due to diffusion will be indeed rather in the mHz range only. Diffusion coefficients are in the order of 10^{-12} m^2 s^{-1} and therefore lead to a small concentration change, resulting in small $\Delta\phi^0$ changes and therewith NFR amplitudes. Nonlinear voltage responses are higher for spherical diffusion compared to planar diffusion as explained in the following. Within the underlying model, spherical and planar diffusion are assumed to have the same surface area. The diffusion area within a sphere becomes smaller towards the inner radius and therefore results in a nonlinear concentration profile during steady-state in the particle due to less diffusive transport than in the planar case. Here, with a uniform diffusion path across the overall thickness and the uniform diffusion area itself, a linear concentration profile and higher molar flows at steady state occurs. This leads to higher nonlinear voltage responses for the spherical compared to the planar diffusion process.

In Figure 2.14 b), individual harmonics Y_2 and Y_3 are shown. Y_2 is thereby more sensitive than Y_3 (additionally shown in the inlet) for both diffusion processes. This corresponds to the findings of the reaction model, where concentration impact excites Y_2 more than Y_3.

2.3.4. Impact of Coupled Reaction and Diffusion

In a next step, the impact of both, reaction and diffusion, is investigated and simulation results are shown in Figure 2.15. Here, the model derived in section 2.2 without further simplifications and including concentration dependent reaction rate, as described in section 2.2 is used.

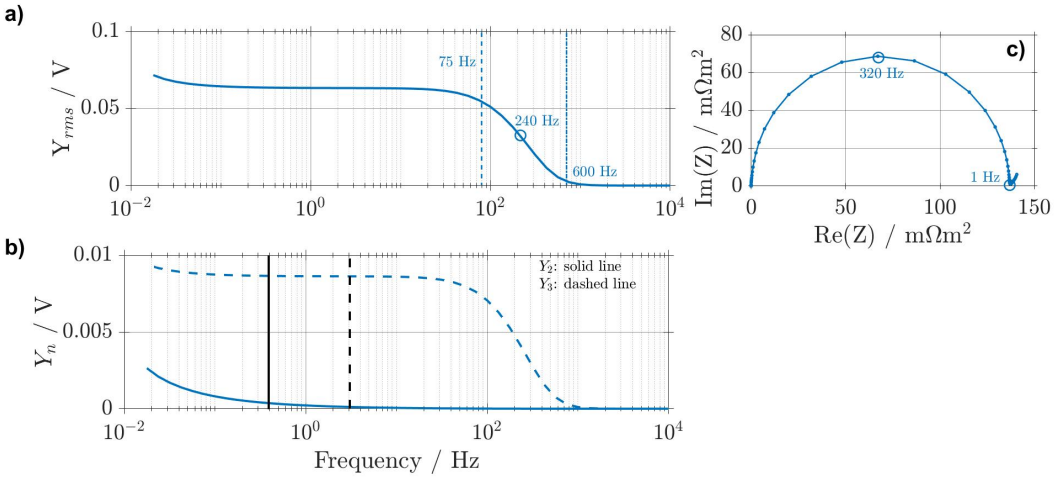

Figure 2.15.: Simulated NFR for reaction with a coupled diffusion process for a) Y_{rms} f_{min} is marked by a dashed blue line and f_{max} is marked by a dash-dotted blue line, b) individual harmonics Y_2 and Y_3 with markers for the beginning of the excitation of the priorly investigated diffusion process (solid black line) and the corresponding frequency of the coupled model (dashed black line) and c) EIS. Reference case simulation parameters from Table 2.1 are used.

For Y_{rms}, shown in Figure 2.15 a), a superposition of the priorly analyzed impacts of reaction and diffusion processes can be seen. At high frequencies, the curve is identical to the spectrum for the reaction process in Figure 2.3 a), as it can be seen by identical values of f_{min}, f_{max} and the corresponding turning point. For lower frequencies, the signal shows, in addition the typical exponential increase due to diffusion effects (see Figure 2.14). In general, nonlinear voltage responses are significantly higher in the low frequency domain, if diffusion is coupled with a reaction process compared to solely investigating the diffusion process. Within the model for quantifying the diffusion impact only its impact on $\Delta\phi^0$ was investigated. When taking into account that most reaction kinetics and thus, η is concentration dependent, this has a strong impact on nonlinearities. It significantly increases nonlinearities in the system by a factor of 100 at the diffusion-dominated low frequency range, showing the dominant impact of diffusion kinetics, i.e. η compared to thermodynamics, i.e. $\Delta\phi_{\mathrm{OCP}}$.

If individual harmonics are investigated, shown in Figure 2.15 b), these findings are confirmed. In general, Y_2 and Y_3 are excited by the coupled processes. Y_3 thereby dominates the overall frequency range and is excited at high frequencies due the reaction process. Since the reaction process is symmetrical at these frequencies due to a quasi steady-state activity of one, Y_2 is not affected at this point. This corresponds to the discussion of the excitation of higher harmonics due to a singular reaction process,

shown in section 2.3.1. Y_2 is excited at lower frequencies, similar as for the investigation of the diffusion process, shown in section 2.3.3. Nevertheless, the amplitude for the excitation of higher harmonics in the diffusion dominated frequency range is significantly higher, thereby confirming the previously mentioned dependency of η of the concentration in this frequency range. Additionally, Y_2 is excited starting at a frequency still characteristic for the reaction, which shows the impact of diffusion on overpotential. The solid black line thereby indicates the beginning of higher harmonic voltage excitation due to the priorly observed diffusion process in scenario 2. It is at lower frequencies than the dashed black line, which marks the onset of higher harmonic voltage excitation of Y_2 for the coupled model. Y_3, however, is less affected from diffusion than Y_2.

In the impedance spectrum, in Figure 2.15 c), a semi-circle for the reaction process with a maximum at 320 Hz and a branch in the low frequency range on the right hand side of the spectrum for the diffusion process, beginning at 1 Hz, are visible, confirming the shown impacts of diffusion at low frequencies.

With these results, the occurrence of Y_2 as well as Y_3 in experimental studies on LiB [47, 64] can be explained, as in battery cells electrochemical reaction and diffusion process are always inevitably coupled.

2.3.5. Impact of Coupled Reactions

In a last step, the excitation of higher harmonics due to two coupled electrodes, i.e. reactions, to understand their interaction, is investigated as this always occurs in electrochemical cells such as batteries. For this purpose a new model without diffusion processes is set up. For each electrode, Butler-Volmer kinetics (equation 2.5), overpotentials η according to equation 2.6 and double layer charging according to equation 2.7 are included. Both sets of equations are coupled by the following relation, resulting in a potential difference $\Delta\phi_{Cell}$.

$$\Delta\phi_{Cell} = \Delta\phi_2 - \Delta\phi_1, \tag{2.15}$$

Base case simulation parameters for both electrodes are provided in Table 2.2. For both, the same species with identical concentration but different capacitances, i.e. time constants, is assumed, to be able to separate the electrode responses.

Parameter:	Reaction 1:	Reaction 2:	Unit:
$c_{A,0}$	$1.5 \cdot 10^4$	$1.5 \cdot 10^4$	mol m^{-3}
C_{DL}	0.2	20.0	F m^{-2}
a_s	$1.5 \cdot 10^5$	$1.5 \cdot 10^5$	m^{-1}
$i_{0,0}$	10	10	A m^{-2}
α	0.5	0.5	-
T	300.0	300.0	K

Table 2.2.: Simulation parameters for the investigation of two coupled reactions.

The interaction of both electrodes can be studied by a variation of characteristic parameters. These characteristic parameters are: the double layer capacitance C_{DL}, the exchange current density i_0, the specific surface area a_s and the symmetry factor α. A variation of C_{DL} causes the excitation of higher harmonic voltage responses to shift towards higher respectively lower frequencies. A variation of i_0 on the other hand leads to in- respectively decreased higher harmonic voltage responses and in parallel to a shift of the excited frequency range. The influence of both parameters on a singular process has been analyzed in-depth within this chapter. At this point, the influence of a variation of a_s is studied in a first case. As a_s influences j_f (equation 2.5) and the charge balance (equation 2.7) in parallel, a variation will lead to in- respectively decreased higher harmonic voltage responses due to equation 2.7, but will counteract the shift of the excited frequency range due to the parallel influence of equation 2.5. This allows to study higher harmonic voltage responses without a further shift of the process itself and therefore to study whether a change of amplitudes of higher harmonic voltage responses of one electrode process has an impact on the other electrode process.

Further, the symmetry factor α has shown to have a significant influence on the excitation of higher harmonic voltage responses and is therefore focus of the second investigation of this section.

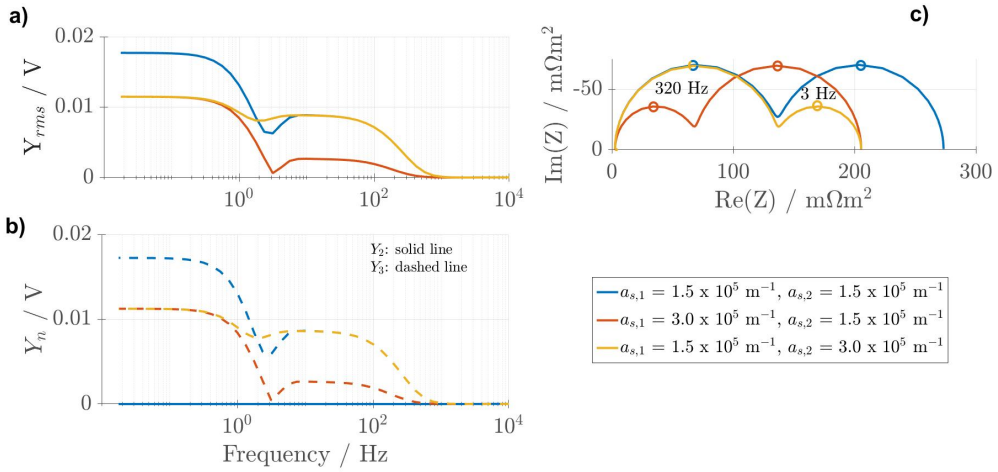

Figure 2.16.: Simulated NFR for two coupled reactions according to Butler-Volmer kinetics with a variation of the specific surface area a_s for a) Y_{rms}, b) individual harmonics Y_2 and Y_3 and c) EIS.

In Figure 2.16 a), the Y_{rms} for a variation of the specific surface area a_s, is shown. Prior research within this thesis showed that the excitation of higher harmonics due to a reaction process influences the overall excited frequency range, beginning with the characteristic frequency of the process. This phenomenon can well be seen for Y_{rms}, where the faster process (1) causes nonlinear voltage responses in the overall excited frequency range and the slower process (2), due to the higher double layer capacitance, only in the medium to low frequency range. If a_s is increased, the overall level of nonlinear voltage responses is decreased. The specific surface area a_s influences the flux in the double layer according to equation 2.7 and the Faradaic volumetric reaction current j_f, according equation 2.5. A greater specific surface area a_s leads to decreasing overpotentials η and thus, nonlinear voltage responses. This effect is well visible for an increasing specific surface area a_s for both reactions. As priorly mentioned, one of the purposes of this parameter variation is to study the impact of higher harmonic voltage responses of one electrode process on the other electrode process. It can be seen that for identical a_s an almost smooth transition between higher harmonic voltage responses of both processes is present. Nevertheless, a small minimum due to the coupling of both processes is present. This may be attributed to resonance effects. If $a_{s,1}$ and $a_{s,2}$ are not identical, this effect becomes stronger.

In Figure 2.16 b), simulation results for individual harmonics Y_2 and Y_3 are shown. Both implemented reactions are perfectly symmetric with $\alpha_{1,2} = 0.5$. Therefore, only Y_3 is excited and Y_2 is not sensitive for a variation of the specific surface area a_s in

this case.

The impedance spectra, shown in Figure 2.16 c), are similarly influenced as the nonlinear voltage responses. With increasing specific surface area a_s, the semi-circles corresponding to the electrochemical reactions become smaller. Characteristic time constants are thereby not affected.

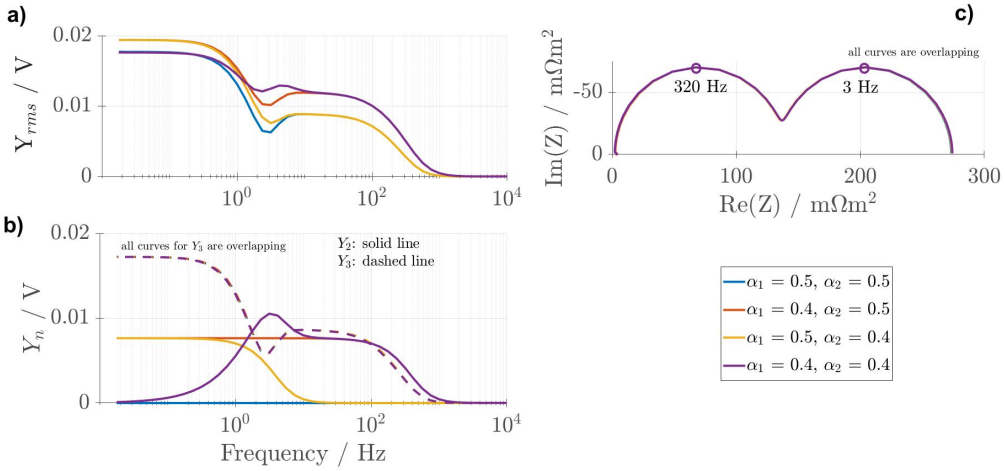

Figure 2.17.: Simulated NFR for two coupled reactions according to Butler-Volmer kinetics with a variation of the reaction symmetry factors $\alpha_{1,2}$ for a) Y_{rms}, b) individual harmonics Y_2 and Y_3 and c) EIS.

In a last step, a variation of the reaction symmetry factors $\alpha_{1,2}$ is investigated. Y_{rms} is shown in Figure 2.17 a) and the corresponding EIS in Figure 2.17 c). For an in-depth evaluation, individual harmonics Y_2 and Y_3, shown in Figure 2.17 b), have to be taken into account. It can be seen that nonlinear frequency responses are more distinctly influenced than the linear output in the impedance spectrum. Concerning the impedances one can barely distinguish between different symmetries of the reactions. Prior research of this thesis showed that an asymmetric reaction causes an excitation of the second harmonic Y_2. This effect is clearly visible, if solely the symmetry factor of one reaction is changed and can be explained as follows: If solely α_1 or α_2 is decreased, the current-voltage relation according to equation 2.5 becomes asymmetrical, as shown in Figure 2.7 a). Thereby leading to the observed excitation of Y_2.

If further both symmetry factors are varied by the same amount, the overall output current-voltage relation becomes symmetrical again. Therefore, decreasing/vanishing the excitation of Y_2, as shown for the purple curve.

These findings are a last and very important addition to the priorly presented research. By varying the reactions symmetry in a coupled system, it is possible to

decrease the sensitivity of the second harmonic by decreasing the symmetry of individual processes.

2.4. Concluding Remarks[2]

Prior research showed that NFRA is a powerful, but yet seldomly used tool for the in-depth study of processes in electrochemical cells and electrodes and for diagnosing cell states. The results in this chapter deliver a basic guideline to enhance interpretation and usage of NFRA via illustrating the nonlinearity using simple fundamental models. The effect of fundamental processes in electrochemical cells on NFR spectra was first analyzed using a basic electrochemical reaction. Subsequently, the often encountered limited reactant availability, i.e. diffusion, is analyzed, and its impact on NFRA was shown. Finally, the interaction of both processes was revealed.

Focus was thereby laid on understanding why and how individual harmonics of an electrochemical reaction are excited by variation of the input amplitude I_{AC}, double layer capacitance C_{DL}, exchange current density i_0 and symmetry factor α. It is shown that exciting a system sinusoidally around an operating point, which shows point symmetry in the nonlinear current-voltage relation causes the excitation of the third harmonic Y_3. This is typically achieved when operating at zero current for a Butler-Volmer kinetics with α=0.5. By changing α or applying a current, an excitation of Y_2 can be generated. NFRA thus yields essential information about the kinetics, which can not be accessed by conventional methods, such as EIS. Bar plots summarize the findings and give an overview on how and where each kinetic and electrode parameter impacts the spectrum.

Additionally, it is shown that planar and spherical solid diffusion cause an excitation of both individual harmonics Y_2 and to less extend Y_3 at low frequencies. Thereby, the relation between current and concentration is purely linear and not exciting higher harmonics. Only due to the nonlinear relation between concentration and potential, higher harmonics are excited. Spherical diffusion was shown to cause higher nonlinearities.

Further, a coupled simulation of reaction and diffusion has been shown to be a super-

[2] Additional information on a pseudo-concentration dependent exchange current density and the effect of the reaction's symmetry to provide further in-depth understanding of the excitation of higher harmonic voltage generation are shown in the Appendix A.1.

position of both signals, with diffusion dominating in the low frequency range and reaction in higher frequencies. Additionally, a significant increase for Y_2 beginning at frequencies still characteristic for the reaction process can be observed.

Last, two reaction processes are coupled and the effect of a variation of a_s as well as the symmetry α of the reaction is investigated. It is thereby shown that a variation of specific surface area a_s can similarly be detected by EIS and NFRA. Concerning the reactions symmetry α, NFRA reveals its high potential. Here, changes in the symmetry highly influence the spectra. Studies thereby showed that it is possible to decrease the amplitude of Y_2 by coupling of two asymmetric reactions, illustrating the high complexity of the interpretation of nonlinear signals.

Electrochemical reaction and diffusion are common processes in LiB. This thesis aims to introduce NFRA on this type of batteries. Therefore, in a next step, a more complex system than a single reaction and spherical or planar diffusion is investigated. For this purpose a state-of-the-art P2D model is chosen.

3 Process Characterization in Current Generation Lithium-Ion Batteries[1]

A battery is a complex system, where various kinds of processes are coupled. Priorly, only single processes, i.e. electrochemical reaction and diffusion and their influence on the excitation of higher harmonics were investigated. In next step, this approach is extended to the analysis of a full-cell battery model.

Fundamentals and an in-depth literature review of NFRA on electrochemical processes are provided in Chapter 1. Within this Chapter, a P2D model is used to characterize processes in the battery with NFRA and to establish this new dynamic measurement method in the field of battery characterization for current generation liquid electrolyte batteries. Parameter and amplitude variations are further applied to enable a reliable interpretation of NFRA measurements: Reaction rate constant, diffusion coefficient and double layer capacitance are varied to detect how nonlinear processes and the output signal are affected. A deeper insight into the cell and a more detailed dynamic analysis are the result of this research. The work demonstrates that for an understanding of the nonlinear processes in batteries not only measurements of higher harmonics but also modeling is essential.

3.1. Modeling of a Liquid Electrolyte Battery

The liquid electrolyte battery model, used for the simulation of NFRA is described within this Chapter. First, model equations are stated. Subsequentially, the evaluation methods are explained. A model-based on state-of-the-art P2D models is used, as described in [6, 5, 7]. Within the P2D model porous, structured electrodes consisting of active material, binder, conducting additives and electrolyte are assumed. Two intercalation electrodes with graphite (C_6) as active material in the anode, Lithium Cobalt Oxide ($LiCoO_2$) in the cathode and a separator are considered. Detailed derivation of model equations are not given within this work but can be found elsewhere [6, 5, 7].

[1] Parts of this chapter have been published in: Nonlinear Frequency Response Analysis on Lithium-Ion Batteries: A Model-Based Assessment, Electrochimica Acta, 260, 614-622, 2018 [9]. Measurements were thereby conducted by Nina Harting.

The model considers the following processes: Solid diffusion, equation 3.1, diffusion and migration in the electrolyte, equation 3.3, potential distribution in the electrodes and electrolyte, equation 3.2 and 3.4, charge accumulation at double layers, equation 3.6, Butler-Volmer kinetics, equation 3.7, concentration dependent exchange current density i_0, equation 3.8, overpotentials η, equation 3.9, Nernst approach for the open circuit potential, equation 3.10, a Nernst-Einstein approach for the electrolyte conductivity, equation 3.11, specific surface are a_s, equation 3.14 and effective conductivity effective conductivity $\sigma_{s,eff}$, equation 3.15. The model equations are summarized in Table 3.1. The model uses spatial discretization by application of a finite volume method. Through a highly resolved univolume mesh it is made sure that the solution is mesh independent. Time derivatives are solved by an adaptive solver in MATLAB. The working principle of NFRA is explained in detail in Chapter 1. Within this research, individual higher harmonics Y_n as well as the sum of higher harmonics, from now on called NFR, are analyzed and interpreted.

Within the experimental investigation, explained in detail in the following section, the first four output oscillations are analyzed. Therefore, the response contains the steady-state and transient part. Because of this, the simulated investigation in this Chapter focuses on the initial response by analyzing the response to the first sinusoidal oscillation only. A systematic analysis of the contribution of the transient part to the overall response is provided later. In this case, NFRA is an instationary investigation method. Further, the aspect of a possible discharge of the battery due to a high AC amplitude is neglected for this research.

For presented simulations, if not declared otherwise, parameters from Table 3.2 are taken. The electrolyte diffusion coefficient D_e is thereby decreased compared to the literature [5] to demonstrate the influence of a limiting electrolyte. Further, reaction rate constants of the anode k_a and cathode k_c are chosen to differ by one order of magnitude to distinguish between the reaction processes in the NFRA and EIS spectrum. All simulations are performed at a state of charge (SOC) of 60%.

$$\frac{\partial c_s(r)}{\partial t} = \frac{1}{r^2}\frac{\partial}{\partial r}\left(D_s r^2 \frac{\partial c_s(r)}{\partial r}\right) \tag{3.1}$$

$$\frac{\partial}{\partial x}\left(\varepsilon_s \sigma_s \frac{\partial \phi_s}{\partial x}\right) = j_{tot} \tag{3.2}$$

$$\varepsilon_e^\beta \frac{\partial c_e(r)}{\partial t} = \frac{\partial}{\partial x}\left(\varepsilon_e^\beta D_e \frac{\partial c_e(x)}{\partial x}\right) + (1 - t_p) \cdot \frac{j_{\mathrm{Li}}(x)}{\mathrm{F}} \tag{3.3}$$

$$\frac{\partial}{\partial x}\left(\varepsilon_e^\beta \sigma_e \frac{\partial \phi_e}{\partial x}\right) = -j_{tot} - 2\frac{\mathrm{R}T}{\mathrm{F}}\left(t_p - 1\right)\sigma_{e,eff} \cdot \frac{\partial \ln c_e}{\partial x} \tag{3.4}$$

$$j_{tot} = j_{\mathrm{Li}} + j_{DL} \tag{3.5}$$

$$j_{DL} = a_s C_{DL} \frac{\partial\left(\phi_s - \phi_e\right)}{\partial t} \tag{3.6}$$

$$j_{\mathrm{Li}} = a_s i_0 \left(\exp\left(\alpha \frac{\eta \mathrm{F}}{\mathrm{R}T}\right) - \exp\left(-(1-\alpha)\frac{\eta \mathrm{F}}{\mathrm{R}T}\right)\right) \tag{3.7}$$

$$i_0 = k_i \mathrm{F} c_e^\alpha \left(c_{max} - c_s\right)^\alpha c_s^{1-\alpha} \tag{3.8}$$

$$\eta = \phi_s - \phi_e - U_{OCV} \tag{3.9}$$

$$U_{OCV} = U_0 + \frac{RT}{\mathrm{F}} \ln\left(\frac{\left(1 - \frac{c_{\mathrm{Li}^+}}{c_{\mathrm{Li}^+,max}}\right)\frac{c_{\mathrm{Li},^+,e}}{c_{\mathrm{Li},^+,e,0}}}{\frac{c_{\mathrm{Li}}}{c_{\mathrm{Li}^+,max}}}\right) \tag{3.10}$$

$$\sigma_e = \frac{\mathrm{F}^2}{\mathrm{R}T}\left(D_{e,\mathrm{Li}^+} + D_{e,\mathrm{PF6}^-}\right) c_e \tag{3.11}$$

$$D_{e,\mathrm{PF6}^-} = \frac{D_e \frac{t_p}{1-t_p} + D_e}{2t_p(1-t_p)} \tag{3.12}$$

$$D_{e,\mathrm{Li}^+} = \frac{t_p D_{e,\mathrm{PF6}^-}}{1 - t_p} \tag{3.13}$$

$$a_s = \frac{3\varepsilon}{R_i} \tag{3.14}$$

$$\sigma_{s,eff} = \sigma_{s,i}\varepsilon_{s,i} \tag{3.15}$$

Table 3.1.: Equations of the LiB model according to [5, 6, 7].

Parameter	Anode	Separator	Cathode
Width δ / μm [5]	50	25.4	26.4
Particle radius R_i / μm [5]	1	-	1
Volume fraction solid ε_s / - [5]	0.58	-	0.50
Volume fraction electrolyte ε_e / - [5]	0.33	0.50	0.33
Maximal solid concentration $c_{s,max}$ / mol m^{-3} [5]	16100	-	23900
Initial solid concentration $c_{s,0}$ / mol m^{-3}	10884	-	10564
Initial electrolyte concentration c_e / mol m^{-3} [5]	1200	1200	1200
Transfer coefficient α / - [5]	0.5	-	0.5
Solid phase diffusion coeff. D_s / m^{2}s^{-1} [5]	$2{\cdot}10^{-16}$		$3.7{\cdot}10^{-16}$
Electronic conductivity σ_s / S m^{-}1 [5]	100	-	10
Electrolyte phase diffusion coeff. D_e / m^{2}s^{-1}	$0.39{\cdot}10^{-10}$	$0.39{\cdot}\ 10^{-10}$	$0.39{\cdot}10^{-10}$
Transference number t_p / - [5]	0.36	0.36	0.36
Bruggeman's exponent β / - [5]	1.5	1.5	1.5
Double layer capacitance C_{DL} / F m^{-2} [5]	0.2		0.2
Reaction rate constant k_i / m^{4}mol^{-1}s^{-1}	$4{\cdot}10^{-12}$	-	$4{\cdot}10^{-11}$

Table 3.2.: Parameter set for simulation.

3.2. Experimental Investigation

Three cells in total with two different cell designs were investigated with NFRA, a commercial 18650 cell with a capacity of 800 mAh and two hand-made pouch cells from the Battery LabFactory Braunschweig with a capacity of $\approx$ 35 mAh. The excitation AC amplitude is set to 2.9 C for the 18650 cell and 1.6 C for the pouch cells. The measurement device can not guarantee a precise sinusoidal input prior to the second oscillation. Therefore, the first output oscillation is discarded. The presented experiments use the first real output oscillation and the four further waves to calculate an average signal with minimum random measurement error. For a more detailed description of the experimental investigation it is referred to the literature [9].

3.3. Results and Discussion

In this section, higher harmonic measurements and simulations are discussed. Concerning simulations, at first, amplitude dependency of NFRA is investigated and then, parameters are varied. This variation covers diffusion coefficient, double layer capacitance, particle radius and electrolyte properties. It is aimed to show influences of individual processes on the spectrum to enable process identification with NFRA.

3.3.1. Experimental Analysis

In Figure 3.1 a) to f), measurements of higher harmonics at LiB with different cell designs, e.g. 18650 cell and pouch cells, are shown as an example for nonlinear voltage responses of such systems. Concerning individual harmonics only the second harmonic, Y_2, and the third harmonic, Y_3, are shown since harmonics of higher orders are in the signal range of measurement noise.

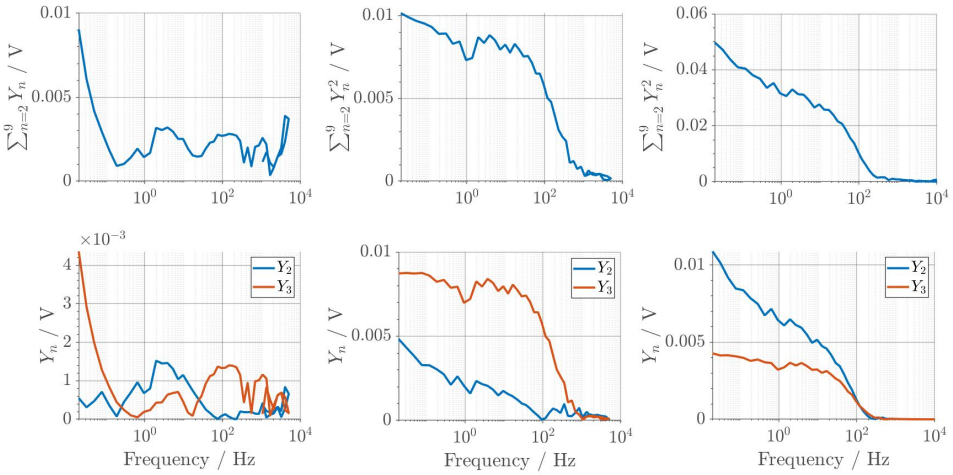

Figure 3.1.: Measurements of NFRA, performed at various LiB at 25°C: sum a) and single harmonics d) of a 18650 cell with 2.9 C amplitude, sum b) and individual harmonics e) of pouch cell A and sum c) and individual harmonics f) of pouch cell B, both with 1.6 C amplitude.

In Figure 3.1 a), a characteristic progression for the sum of higher harmonics for a 18650 cell with a capacity of 800 mAh with an AC amplitude of 2.9 C can be observed. Peaks at 145 Hz and 3 Hz are detectable as well as an increase of the nonlinear response for frequencies lower than 0.2 Hz. The second, Y_2, and third, Y_3, harmonics strongly deviate from each other as shown in Figure 3.1 d). Y_3 shows a high sensitivity in the low frequency range (< 0.1 Hz) and at a frequency in the order of 100 Hz. In the frequency range inbetween, Y_2 is more sensitive.

In Figure 3.1 b), the sum of higher harmonics for a pouch cell with a capacity of ≈ 35 mAh measured with an AC amplitude of 1.6 C is shown. Again, characteristic areas can be identified with negligible higher harmonics > 1000 Hz, high, almost constant, nonlinear responses < 100 Hz and a local minimum at ca. 1 Hz. The third harmonic Y_3, as shown in Figure 3.1 e), is more sensitive in the complete frequency range. For pouch cell B, the sum of higher harmonics in Figure 3.1 c) shows a similar progression

as pouch cell A, though with a significant higher intensity. Concerning the individual higher harmonics in Figure 3.1 f), the sensitivity is vice versa of cell B: the voltage response Y_2 is higher in the complete frequency range. By investigating measurements at three different cells it can be stated that NFR highly varies with cell design.

Modeling of NFRA is the key to interpret the observed characteristic progression of individual higher harmonics and their sum with the frequency, to understand how NFRA may be used for studying processes and states of the battery and to get a deep understanding of the potential of this dynamic measurement method. Therefore, within the following section NFR is analyzed with amplitude and parameter variations with a battery model.

3.3.2. Amplitude Sensitivity

First, the influence of the amplitude of a sinusoidal input on the response is analyzed. Therefore, amplitudes of the input sinusoidal current are varied between 1 C and 10 C, and the response is simulated using the parameter set from Table 3.2. In parallel, EIS with an amplitude of 1/15 C is investigated to be able to correlate NFRA behavior to typical EIS features.

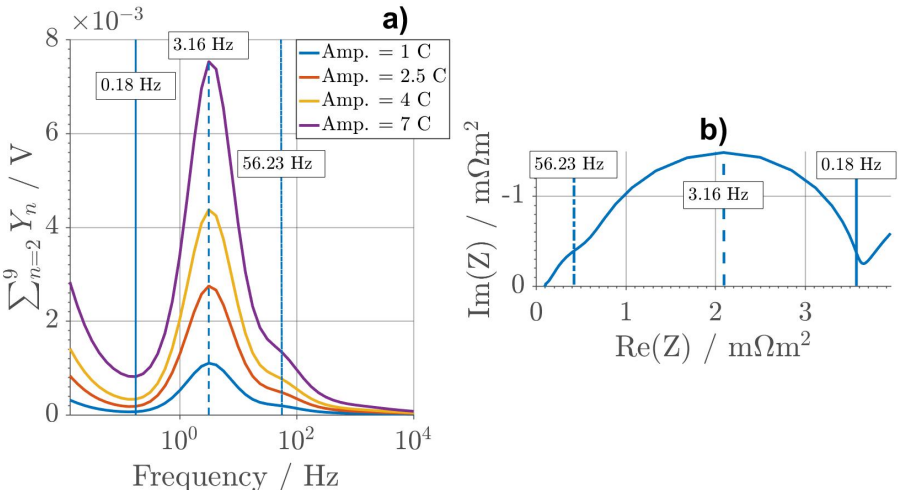

Figure 3.2.: Nonlinear frequency response for variation of input amplitude with the sum of higher harmonics a) and b) corresponding EIS with input amplitude C/15, conditions: SOC 60% and T=25°C.

In Figure 3.2 a), the sum of higher harmonics is shown versus the corresponding input frequency for various amplitudes. With increasing amplitude, the response and therewith the nonlinearities increase monotonously over the whole frequency range. Three characteristic frequency ranges are visible: Below 0.18 Hz, NFR in-

creases monotonously with decreasing frequency. The limiting process at such frequencies is solid diffusion [79]. Peaks at 3.16 Hz and 56.23 Hz are observed; here, faster processes, such as electrochemical reactions take place. No further signals and as such nonlinear processes are visible in the simulations for frequencies higher than 10^4 Hz. Typical processes occurring at such frequencies are SEI and transport through current collectors; they are not implemented in the model. In Figure 3.2 b), the corresponding EIS spectrum is shown. Two semi-circles are present, one small semi-circle with a characteristic frequency of 56.23 Hz and a large one with a characteristic frequency of 3.16 Hz. Each semi-circle represents one electrochemical reaction. Further, a diffusion part can be identified at low frequencies $<$0.18 Hz in the EIS. An excellent match between EIS and NFRA is visible, peaks for electrochemical reactions match perfectly and also diffusion influence is visible at identical frequencies. Concerning NFRA, the characteristic maximum at 3.16 Hz and 56.23 Hz for electrochemical reactions stay constant within the whole range of amplitudes. Higher amplitude results in higher nonlinear responses, and frequency ranges of processes are not affected for the chosen parameter set.

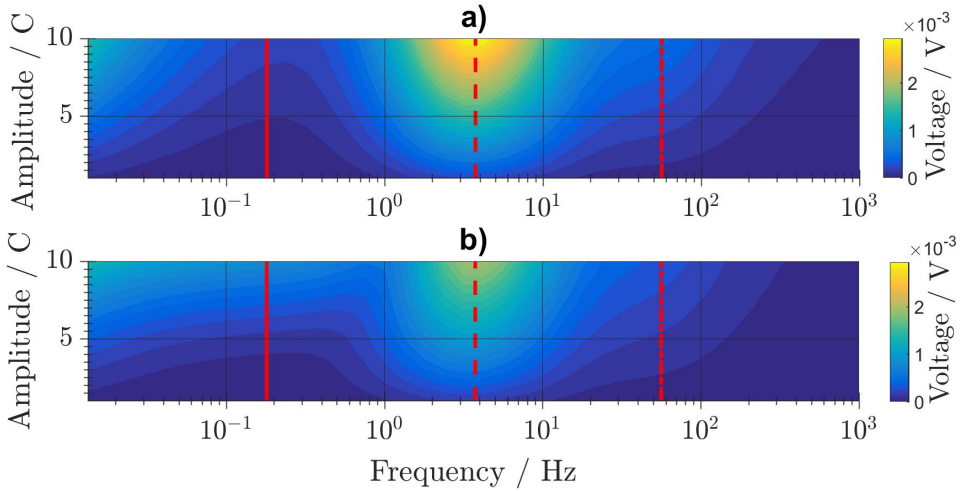

Figure 3.3.: Amplitude and frequency dependency of a) the second Y_2 and b) the third higher harmonic Y_3, red line: solid at 0.18 Hz, dashed at 3.16 Hz and dash/dotted at 56.23 Hz.

In Figure 3.3, the second harmonic response Y_2 and the third harmonic response Y_3 are shown respectively for the amplitude variation to study the influence of amplitude on processes. For the chosen parameter set, the second harmonic Y_2 surpasses the third harmonic Y_3 with the exception of the frequency range between 0.05 Hz and 1 Hz. With increasing amplitude, the voltage response Y_3 is stronger influenced in this

frequency range than the voltage response Y_2. The qualitative progression of both higher harmonics Y_2 and Y_3 with frequency is similar within the simulated frequency range. As a result, both individual higher harmonics show the same characteristic frequencies. For further simulations, a fixed amplitude of 4 C is chosen to guarantee nonlinear excitation of the battery and to ensure comparability to measured spectra.

3.3.3. Sensitivity to Electrode Properties

As shown before, processes can be correlated to the characteristic frequencies in NFR spectra. Further, it is important to know how changes of these processes, such as diffusion and electrochemical reactions, affect the spectrum. Thereby, only changes in cathode processes are further investigated since it is assumed that anode processes have similar influences. In Figure 3.4 a), the EIS and in Figure 3.4 b), the corresponding sum of higher harmonics are shown for a variation of the solid diffusion coefficient of the cathode $D_{s,c}$. A decreasing diffusion coefficient $D_{s,c}$ results in an increased real and imaginary part for the EIS in the low frequency range, as seen in the inset in Figure 3.4 a). Physically, a smaller diffusion coefficient $D_{s,c}$ causes a higher concentration gradient in the active material particles and therefore changes in the surface concentration become stronger. This directly influences the electrochemical reaction due to a strong correlation of current and potential in equation 3.8 and leads to an increased impedance. In Figure 3.4 b), similar observations can be made for NFRA. The nonlinear voltage response increases in the low frequency range when decreasing the diffusion coefficient. Solid diffusion thus has neither an influence on NFR nor on EIS at higher frequencies. By this, the capability to identify and characterize the diffusion process with NFRA is further confirmed.

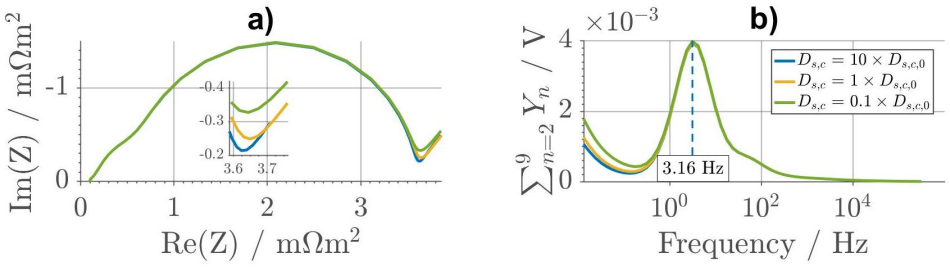

Figure 3.4.: Influence variation of $D_{s,c}$ with $D_{s,c}$ =3.7·10^{-15} m^{2}s^{-1} to $D_{s,c}$ =3.7·10^{-17} m^{2}s^{-1} on a) EIS and b) corresponding sum of higher harmonics.

In Figure 3.5 a), the EIS and in Figure 3.5 b), the corresponding sum of higher har-

monics for a variation of the cathode double layer capacitance $C_{DL,c}$ are shown. The cathode double layer capacitance $C_{DL,c}$ directly influences the frequency range characteristic for the cathode reaction. The smaller the cathode double layer capacitance $C_{DL,c}$ becomes, the higher the characteristic frequency of the reaction process gets as the double layer is charged faster, resulting in an increased reaction current and thus a faster response. In the EIS, for higher values than $C_{DL,c}$ =0.2F m^{-2}, the characteristic frequency of the cathode reaction becomes similar to the frequency of the anode reaction and therefore both processes can not be separated. For smaller values, both processes can be separated in the EIS and NFR spectrum and the cathode reaction occurs at higher frequencies. Therefore, the left semi-circle in the EIS represents the cathode reaction. In Figure 3.5 b), the peak at high frequencies corresponds to the cathode reaction and the left one to the anode reaction. For a larger double layer capacitance than $C_{DL,c}$ =0.2F m^{-2}, processes can not be separated, similar to the EIS investigation. For a smaller double layer capacitance $C_{DL,c}$, processes are separable. Concluding, additionally to the diffusion process, the charging of double layers and its interaction with the electrochemical reaction within the cell can be studied by using NFRA.

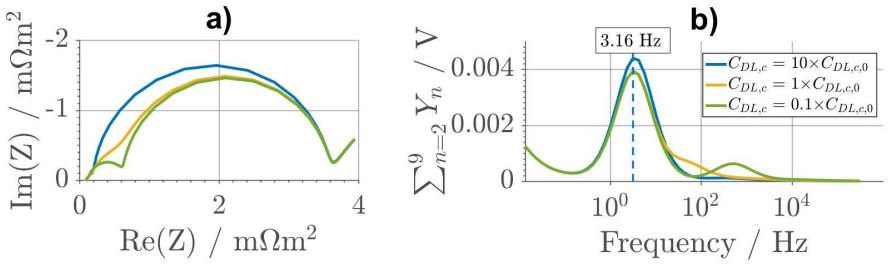

Figure 3.5.: Influence variation of $C_{DL,c}$ with $C_{DL,c}$ =20· F m^{-2} to $C_{DL,c}$ =0.02· F m^{-2} on a) EIS and b) corresponding sum of higher harmonics.

Further in Figure 3.6, the effect of variation of the cathode reaction rate constant k_c is shown on the EIS and NFR spectrum. According to equation 3.7 and 3.8, a larger reaction rate k_c causes lower overpotentials η. This should lead to a faster reaction and less nonlinearities in the voltage response. In Figure 3.6 a), NFRA is shown. Beginning from k_c =4·10^{-11} m^{4}mol$^{-1}s^{-1}$ (blue) to k_c =4·10^{-13} m^{4}mol^{-1}s^{-1} (green), the cathode reaction moves from frequencies higher than for the anode reaction, at 3 Hz, to lower ones. The anode reaction is thereby not affected. Its characteristic peak stays

constant at 3 Hz and is completely covered by the cathode reaction peak. This effect is shown in the inset for reaction rate constants k_c ranging from $k_c = k_c = 4{\cdot}10^{-11}$ m^4mol^{-1} to $k_c = 4{\cdot}10^{-12}$ m^4mol^{-1}. The characteristic frequency moves from 40 Hz (blue) for $k_c = 4{\cdot}10^{-11}$ to 4 Hz for $k_c = k_c = 4{\cdot}10^{-12}$. Thereby, two initially separated peaks merge and the anode peak at 3 Hz (black) is covered due to higher nonlinear voltage responses of the cathode reaction. For small reaction rates k_c, the characteristic slope for the diffusion process in the low frequency area is not visible. This indicates an overlap of cathode reaction and diffusion process with significant higher nonlinear voltage responses for the reaction.

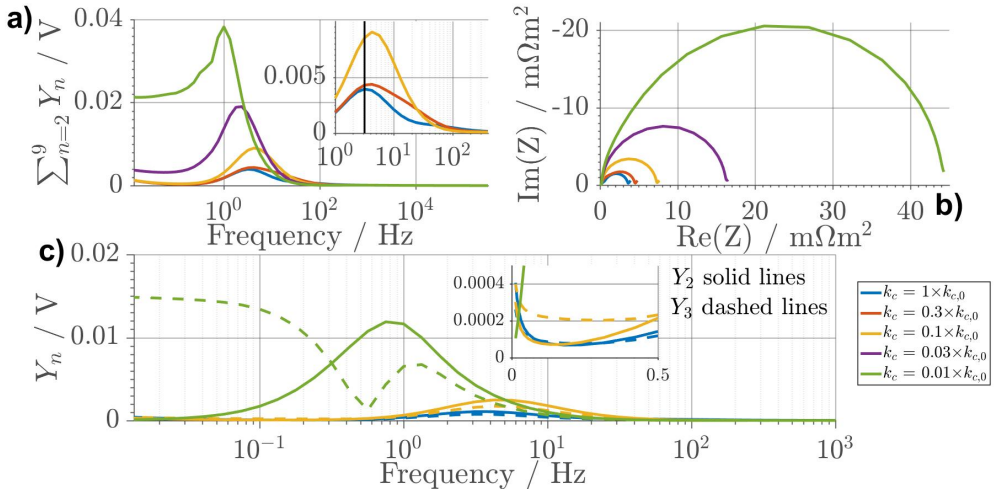

Figure 3.6.: Influence of cathode reaction rate constant k_c on a) sum of higher harmonics, b) EIS and c) individual higher harmonics Y_2 (solid line) and Y_3 (dashed line) c); k_c ranges from $k_c = 4{\cdot}10^{-11}$ $m^4mol^{-1}s^{-1}$ to $k_c = 4{\cdot}10^{-13}$ $m^4mol^{-1}s^{-1}$.

In the EIS, in Figure 3.6 b), one can see that smaller reaction rate constants k_c lead to a larger cathode reaction semi-circle. For the original reaction rate k_c (blue) two separate semi-circles exist. With decreasing k_c the cathode semi-circle increases and moves towards lower frequencies, thereby covering the anode semi-circle. For the lowest reaction rate $k_c = 4{\cdot}10^{-13}$ $m^4mol^{-1}s^{-1}$, the cathode reaction additionally dominates the diffusion process, resulting in a disappearing of the diffusion branch. In Figure 3.6 c), individual higher harmonics are shown. For $k_c = 4{\cdot}10^{-11}$ $m^4mol^{-1}s^{-1}$ (blue) and $k_c = 4{\cdot}10^{-12}$ $m^4mol^{-1}s^{-1}$ (yellow) the diffusion and electrochemical reaction processes are separable with NFRA, visible by a distinct peak for both harmonics in the mid frequency range and a diffusion part for low frequencies, shown in the inlet. Beginning with $k_c = 4{\cdot}10^{-12}$ $m^4mol^{-1}s^{-1}$ (yellow), Y_3 surpasses Y_2 in the frequency

range characteristic for diffusion, i.e. <0.5 Hz. Y_2 on the other hand dominates within the frequency range of the electrochemical reactions, between 0.5 Hz and 10 Hz. This effect becomes stronger for k_c =4·10^{-13} m^{4}mol^{-1}s^{-1} (green) and diffusion and electrochemical reaction are no longer separable. The possible differences for the progression of higher harmonics may be explained with different parities of the higher harmonics. Concluding, similar time constants of the diffusion and electrochemical reaction lead to a change of the characteristic progression of Y_2 and Y_3.

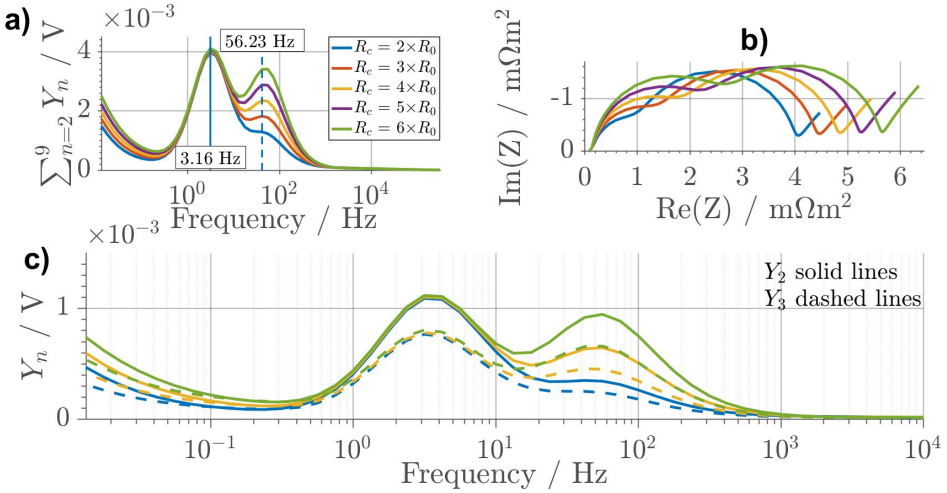

Figure 3.7.: Difference of cathode active material radius R_c on a) sum of higher harmonics, b) EIS and c) individual higher harmonics Y_2 (solid line) and Y_3 (dashed line) ranging between R_c =2·10^{-6} m to R_c =6·10^{-6} m.

In Figure 3.7 the influence of a variation of the cathode active material particle radius R_c is shown. For the sum of higher harmonics (Figure 3.7 a)), the corresponding characteristic frequency of the cathode reaction remains at f =56.23 Hz for all radius values. In this frequency range, the amplitude of the nonlinear voltage response increases with the cathode active material particle radius R_c. The specific surface area a_s depends on the active material particle radius R_c, as shown in equation 3.14. It directly influences the Butler-Volmer kinetics in equation 3.7. With a larger radius R_c the surface area a_s becomes smaller and the overpotential η has to increase to generate the same flux j_{Li}, causing an increased nonlinear voltage response. Simultaneously, the electrochemical reaction would occur at lower frequencies since the process becomes slower. In parallel to the change in the Butler-Volmer kinetics, the smaller specific area a_s affects the j_{DL} in equation 3.6. This in contrary causes a faster response. Therefore, both phenomena counteract, which results in a cathode reaction occurring in the same frequency range for the overall range of radii.

Further, the diffusion paths become longer with an increased radius. This results in increased nonlinear voltage responses in the solid diffusion dominated low frequency range. Concerning the EIS in Figure 3.7 b), the left semi-circle represents the cathode reaction as previously discussed. The larger the radius R_c becomes, the bigger the corresponding semi-circle gets and the more distinct is the diffusion process. Similar as for NFRA, the EIS reveals only changes in the cathode processes.

In Figure 3.7 c), the individual nonlinear voltage responses are investigated. In addition to the increased signal within the frequency ranges characteristic for diffusion and cathode reaction, a slight influence on the signal within the frequency range characteristic for the anode is visible. With an increasing particle radius R_c, the overall frequency range for the diffusion and reaction processes increases. Therefore, an increase in nonlinear voltage responses at a broader frequency bandwidth is visible. This information is essential to qualitatively compare different cell types but also for quantitative analysis.

Concluding, the characteristic progression of the individual higher harmonics is not influenced by a variation of the active material particle radius R_c. In general, the nonlinear voltage response increases with increasing particle radius R_c.

3.3.4. Sensitivity to Electrolyte Properties

Electrolyte properties change due to cell ageing and between cell types. To take this into account, the electrolyte diffusion coefficient D_e and respectively, due to the relation in equation 3.11, the conductivity σ_e, are simultaneously varied. The simulation results are shown in Figure 3.8. The EIS and NFR spectrum are slightly influenced in the frequency range characteristic for solid diffusion.

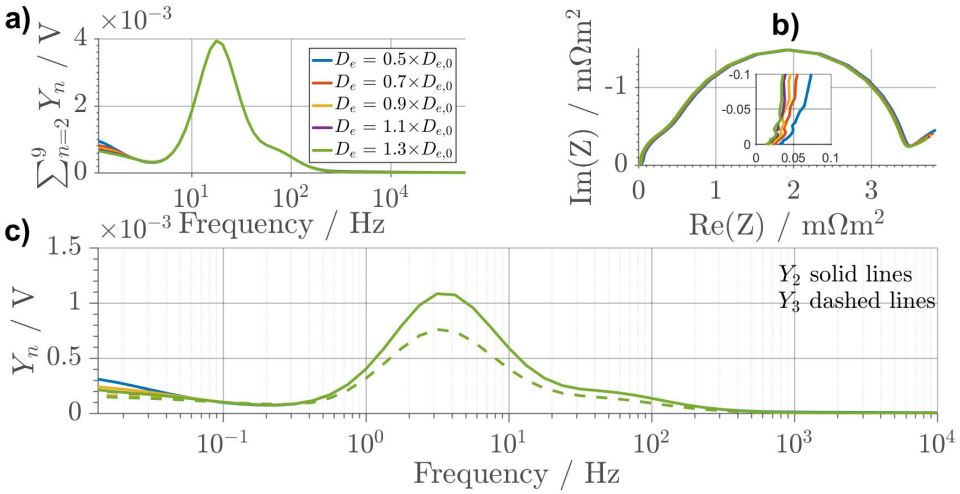

Figure 3.8.: Difference of electrolyte diffusion coefficient D_e on a) sum of higher harmonics, b) EIS and c) individual higher harmonics Y_2 (solid line) and Y_3 (dashed line) ranging between $0.5 \times D_{e,0}$ and $1.3 \times D_{e,0}$.

If the diffusion coefficient D_e is lowered, a more distinct concentration profile in the electrolyte will develop, an effect most distinct for low frequencies. This leads, due to coupled processes, to different concentrations at the particle boundaries, thereby influencing the solid diffusion process. For NFRA in Figure 3.8 a), the diffusion is more distinct for a lower diffusion coefficient D_e, visible by higher nonlinear voltage responses. In the EIS in Figure 3.8 b), the diffusion branch increases with decreasing electrolyte diffusion coefficient D_e. Concerning both methods, EIS and NFRA, only a minor effect of the electrolyte diffusion is present. By changing D_e the conductivity σ_e is changed due to the direct relation in equation 3.11. Therefore, with EIS, the influence of the electrolyte conductivity σ_e is visible a high frequencies. A lower conductivity σ_e leads to an increased internal resistance due to the Ohmic potential distribution. Concerning the influence on the individual higher harmonics, in Figure 3.8 c), the characteristic progression is not further influenced.

A major impact on cell ageing, which is not included in the modeling, is the change of the SEI due to electrolyte degradation. This may strongly effect both spectra and is discussed in Chapter 4.

3.3.5. Comparison of Experiments and Simulation

Next to a simulation of parameter variations, it is aimed to compare measurement and simulation. Therefore, the characteristic progression of the sum of higher harmonics for active material particle radii of $R_a = 1 \cdot 10^{-6}$ m and $R_c = 6 \cdot 10^{-6}$ m and the

measurement of the 18650 cell of Figure 3.1 a) are compared in Figure 3.9.

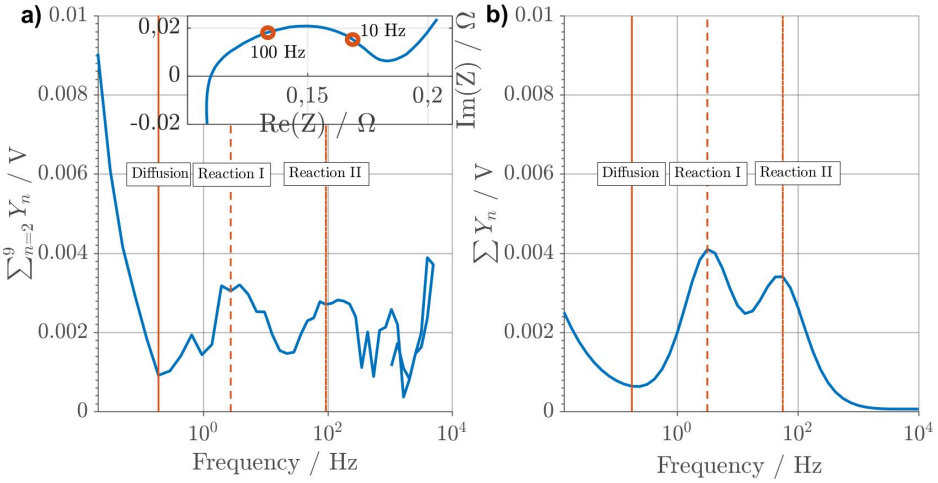

Figure 3.9.: Measured sum of higher harmonics for the 18650 cell in a) and simulation with active material particle radii of R_a =1·10^{-6} m R_c =6·10^{-6} m in b).

Strong nonlinearities at low frequencies and two characteristic peaks in the mid frequency range can be identified in experiment and simulation. Time constants for simulation and experiment are in similar frequency ranges. Further, in the inlet of Figure 3.9 a), the measured impedance spectrum with only one flattened semi-circle is shown. Harting et. al showed that processes can be distinguished with NFRA even if they cannot be separated by EIS [47]. Thus two different processes underlying this one semi-circle are assumed. The simulation based analysis allows now to interpret such experimental spectra. It should be noted that for the simulation based studies, no SEI processes were included in the model. Transport through the SEI is mostly a linear process with typical time constants above 100 Hz [79]. Its detailed analysis should be discussed separately in future studies.

3.4. Concluding Remarks

Within this Chapter, NFRA has been applied to a P2D model for liquid electrolyte cells. Measurements of three different cell types show that characteristic frequency ranges can be detected for all cells, though the cell spectra strongly diverge. Amplitude and the progression of individual higher harmonics strongly differ between cells. Thus, model-based analysis is used to enhance process characterization and identification.

The investigated system reaches for a new steady-state, once it is excited with a si-

nusoidal current with high excitation amplitude. Therefore, one can distinguish between a transient and a steady-state excitation concerning NFRA. Within Chapter 2, singular processes were investigated in the steady-state. In contrast to this, for the application on LiB, the first output oscillation was chosen for investigation, since a transient part in the presented measurements was assumed. The corresponding simulated NFR spectra contain a transient and a steady-state part as previously described. This leads to differences between NFR spectra of Chapter 2 and this chapter.

Modeling and simulation have been applied to identify which processes can be observed with NFRA and how they affect individual higher harmonics and their sum. With NFRA, diffusion and electrochemical reactions can be separated and the dynamics of the nonlinear system can be detected. It is shown that depending on the chosen cell parameters and therefore on cell properties, the progression of higher harmonics changes. If electrochemical reactions occur at low frequencies and the characteristic time constants become similar to the one of the diffusion process, it is observed that the third harmonic Y_3 surpasses the second harmonic Y_2.

Concluding, this model-based analysis is indeed essential to get a deeper understanding of the nonlinear response and the underlying processes and as such to interpret experimental studies. The progression of the nonlinear voltage response strongly varies with the cell chemistry. Individual higher harmonics can change their characteristic progression, thereby enabling the possibility of further in-depth cell characterization. This analysis contained the steady-state as well as the transient part of the response to a sinusoidal input. In-depth investigation of these individual parts is of high interest to further refine the measurement method. In general, the combination of NFRA and EIS is a new powerful and non destructive method to deeply characterize LiB and their nonlinear and linear processes.

Within this chapter higher harmonics voltage responses of LiB were calculated in the transient state. In a next step, it is aimed to understand differences between the transient and steady-state and the corresponding excitation of higher harmonics. To further enhance the predictability of the model and to enhance understanding with NFRA, additionally, the SEI is included in the model. Here, the SEI is implemented in a SP battery model due to the complexity of the SEI process and its interaction with higher harmonic voltage responses.

4 Solid-Electrolyte-Interface in Lithium-Ion Batteries[1]

After demonstrating a first application of NFRA on LiB in the transient state, it is aimed to understand the transition from transient to steady-state and the excitation of higher harmonics in the steady-state. The priorly investigated state-of-the art model further neglected the effect of ageing. To account for both, a SP-battery model is extended with a SEI. This step backwards from a P2D to a SP model is conducted due to the complexity of the transition from the initial excitation to the steady-state in combination with the SEI process.

The SEI is believed to be the dominating effect for ageing in liquid electrolyte cells [43]. Therefore, deep understanding of thr impact of the SEI on cell dynamics is essential to enable longer battery lifetime. The common assumption that the SEI consists of a dense inner and a porous outer layer is based on the work of Peled et al. in which the physical properties of the SEI are explained, they further achieved agreement between measured impedance results and an ECM [80]. Based on this work, Gao et al. used a Point Defect Model (PDM) which has been introduced by Macdonald to describe transport processes within the SEI [81, 82]. Using this PDM, Gao and Macdonald have been able to simulate the influence of the SEI on metal surfaces on the impedance spectrum. In order to further analyze the SEI, Nainville et al. developed a model which simulates the growth of the SEI on Lithium anodes [83]. Broussely et al. extended the prior model and used a full LiB model focussing on calendar ageing [20]. In 2004, Christensen et al. published results for the growth of the SEI during charge and discharge cycles with an isothermal physics-based ageing model [84]. Based on this model, Colclasure et al. developed a thermodynamically consistent model con-

[1] Parts of this chapter have been published in: Physico-Chemical Modeling of a Lithium-Ion Battery: An Aging Study with Electrochemical Impedance Spectroscopy, Batteries & Supercaps, 2, 1-12, 2018, [10]. The paper on EIS has been written by Marco Heinrich and Nicolas Wolff. Both authors contributed equally to this paper. The literature review of the paper and this chapter was mostly done by Marco Heinrich whereas model derivation and initial parameter fitting was performed by Nicolas Wolff. All measurements were conducted by Nina Harting. Further parts of this chapter have been published in: Nonlinear Frequency Response Analysis on Lithium-Ion Batteries: Process Identification and Differences between Transient and Steady-State Behavior, Electrochimica Acta 298, 788-798 2019 [11], again, all measurements were conducted by Nina Harting.

sidering the detailed chemistry of the SEI growth for a SP model of the anode [6, 8]. This approach has been used by Röder et al. who combined it with a kinetic Monte Carlo model to perform multi-scale simulations of the SEI formation [72]. Zavalis et al. did not use a detailed model like Christensen et al. and Colclasure et al., but achieved agreement between simulations and measurement data during ageing [85]. In one of the few works including a model-based analysis of the ageing impact on the impedance spectrum, Xie et al. adjusted simulation parameters of a battery model to investigate impedance data from cycle-aged coin cells [86].

Within this Chapter, first, a full cell SP model with simplifications in the amount of considered reactions and neglected diffusion processes in the SEI is developed and fully derived. The transport of Lithium-ions across the SEI/electrolyte interface may be a rate determining step [87] and its kinetics has up to now been barely investigated and understood despite of extensive research on SEI. Therefore, it is further aimed within this chapter to make use of possibly the greatest advantage of NFRA: the possibility to distinguish between linear and nonlinear processes in electrochemical cells, and thus to gain knowledge about the nature of an investigated process, whether it has a linear of nonlinear kinetic. Thus, both, a linear and nonlinear current-voltage relation for this transport process are implemented in the battery model to compare the effect that both ion transport kinetics have on NFRA and thus to lay the foundation for identifying the nature of this process. In a further step, the influence of transient and steady-state behavior are investigated. Differences between the initial excitation, i.e. transient behavior, and the steady-state behavior in NFRA, for both, experiment and simulation are thereby shown. Further, reaction rate constants k_i, double layer capacitances $C_{DL,i}$, diffusion coefficients $D_{s,i}$ and excitation amplitude are varied within the model for process characterization. The results are compared to experimentally recorded and simulated EIS.

4.1. Modeling of a Battery with Solid-Electrolyte-Interface

A SP full cell battery model including a SEI at the anode side, schematically shown in Figure 4.1, is derived in this section. Focus is thereby laid on the anode side, where equations for reaction kinetics are in-depth analyzed. Fundamentals and in-depth literature review on EIS and NFRA are not discussed as they already have been provided in Chapter 2.

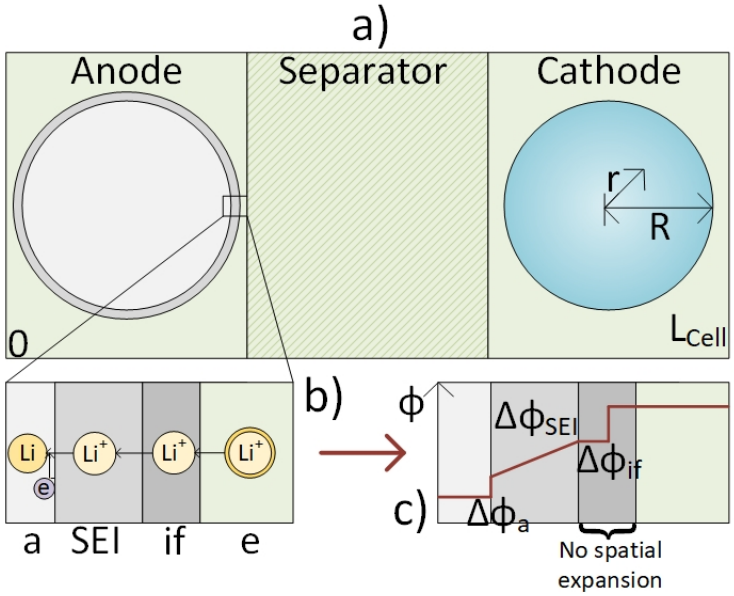

Figure 4.1.: Schematic illustration of a SP-SEI model a) including magnified illustration of the anode particle/SEI (a/SEI), SEI/electrolyte interface (if/e) b) and the corresponding potential distribution c) [10].

The geometry, underlying the model is illustrated in Figure 4.1. It consists of a negative electrode, a positive electrode and a separator inbetween. Both electrodes are assumed to be porous. Electrodes and separator are not discretised in x-direction for this study, to focus on the analysis of the main effects. Modeled spherical active material particles are radially discretised. On the anode side, an additional SEI layer is implemented as shown in Figure 4.1 b) [88]. During the charging process a solvated Lithium-ion, originating from the electrolyte phase, enters the interfacial area (if) of the SEI, where it loses its solvate layer. This process is analogously described to a charge transfer reaction and is displayed in Figure 4.1 c) as a potential drop. Note that the interfacial layer has no spatial expansion. Next to the interfacial area, the

SEI is present and an Ohmic potential distribution causing a linear potential drop is assumed. At the particle-SEI interface, Lithium electrochemically reacts and intercalates in a next step into the active material particle. For the following model derivation, abbreviations from Figure 4.1 are used to mark the corresponding interface and underlying process.

Fundamental equations underlying the model have already been extensively discussed. Therefore, Table 4.1 is provided where implemented processes are listed. Equations are not shown again.

Process	Equation
solid diffusion	equation 3.1
diffusion and migration in the electrolyte	equation 3.3
accumulation of reaction and douvle layer flux	equation 3.5
charge accumulation at double layers	equation 3.6
Butler-Volmer equation for cathode reaction	equation 3.7
concentration dependent exchange current density for cathode $i_{0,c}$	equation 3.8
overpotentials η	equation 3.9
specific surface area a_s	equation 3.14

Table 4.1.: Summarized fundamental model equations for SP model

For the calculation of the cathode overpotential η_c, shown in equation 3.9, the open circuit voltage of the cathode active material is needed. In this case a measured OCV curve, as implemented by Lenze et al. [28], is used. Concerning the anode side, a derivation follows within this chapter. Further all additional model equations are shown and derived if necessary.

The potential distribution within the electrolyte is approximated with a Ohmic, therefore linear, approach:

$$\Delta\Phi_e = \frac{L_{Cell}}{\sigma_e}\frac{j_{Li}}{F}, \tag{4.1}$$

with the electrolyte conductivity σ_e.

At the anode side of the model, a SEI is implemented. The entering of Lithium-ions into the interfacial area between solid and liquid electrolyte might be closely related to the skimming of their solvate layer [87]. Yamada et al. reported that this might be the rate-determining step [89], but no further research on this topic has been reported yet:

$$\mathrm{Li}^+ + V_{Li,if} \rightleftharpoons \mathrm{Li}^+_{if}, \tag{4.2}$$

with $V_{\mathrm{Li},if}$ as vacancies at the SEI/electrolyte interface (if). Afterwards the Lithium-ions enter the SEI from the if:

$$\mathrm{Li}^+_{if} \rightleftharpoons \mathrm{Li}^+_{SEI} + V_{Li,if} \tag{4.3}$$

This reaction is directly coupled with a charge-transfer reaction at the SEI/particle interface (a/SEI) to enforce charge neutrality within the SEI. Thereby, $V(\mathrm{C}_6)$ equals an intercalation vacancy within the graphite [6]:

$$\mathrm{Li}^+ + \mathrm{e}^- + V(\mathrm{C}_6) \rightleftharpoons \mathrm{Li}(\mathrm{C}_6) \tag{4.4}$$

The ion flux resulting from these coupled processes is calculated with equation 4.5 according to [90],

$$j_{Li,a} = \frac{c_{Li,a}\gamma_{\mathrm{Li}}\lambda_{a,SEI}\lambda_{SEI,if} - c_{Li,if}\gamma_V\lambda_{SEI,a}\lambda_{if,SEI}}{\lambda_{SEI,a} + \lambda_{SEI,if}}, \tag{4.5}$$

with $c_{Li,if}$ as Lithium-ion concentration at the if-side and $c_{Li,a}$ as Lithium concentration at the surface of the active material particle. The activity coefficients of Lithium in the active material γ_{Li} and corresponding vacancies in the active material γ_V are calculated using a Redlich-Kister approach according to [6]. At this point, no further surface coverage balance equation is implemented.

$$\gamma_{Li} = \exp\left(\frac{1}{\mathrm{R}T}(1-y_a)^2\sum_{i=1}^{11}B_i\,(2y_a-1)^i\left(1+\frac{2iy_a}{2y_a-1}\right)\right), \tag{4.6}$$

$$\gamma_V = \exp\left(\frac{1}{\mathrm{R}T}y_a^2\sum_{i=1}^{11}B_i\,(2y_a-1)^i\left(1+\frac{2i(1-y_a)}{2y_a-1}\right)\right), \tag{4.7}$$

with $y_a = c_a/c_{max,a}$ and B_i as Redlich-Kister parameters, which are listed in the Appendix in Table A.1. To solve equation 4.5, the reaction coefficients $\lambda_{a,SEI}$, $\lambda_{SEI,a}$, $\lambda_{SEI,if}$ and $\lambda_{if,SEI}$ are needed. The index a,SEI equals the forward and the index SEI,a the backwards main charge transfer reaction. The indices SEI,if and if,SEI

are used in the same manner for the concentration dependent reaction.

$$\lambda_{a,SEI} = a_{s,a} \cdot k_{f,a} \exp\left(\alpha_a \Delta\Phi_a \frac{\mathrm{F}}{\mathrm{R}T}\right), \tag{4.8}$$

$$\lambda_{SEI,a} = a_{s,a} \cdot k_{b,a} \cdot \exp\left(-\left(1-\alpha_a\right)\Delta\Phi_a \frac{\mathrm{F}}{\mathrm{R}T}\right), \tag{4.9}$$

$$\lambda_{SEI,if} = a_{s,if} \cdot k_{f,SEI} \cdot (1-\Theta), \tag{4.10}$$

$$\lambda_{if,SEI} = a_{s,if} \cdot k_{b,SEI}, \tag{4.11}$$

with the reaction rate constants $k_{f,a}$, $k_{b,a}$, $k_{f,SEI}$ and $k_{b,SEI}$ for each forward and backward reaction, α_a as reaction symmetry factor and with the occupied surface sites Θ. Θ is thereby obtained/calculated from the vacancies $V_{Li,if}$ given in the reactions in equations 4.2 and 4.3.

Forward reaction rate constants are provided in Table 4.3. The corresponding backwards reaction rate constant is calculated with equation 4.12, according to [6].

$$\frac{k_f}{k_b} = \frac{c_C^0 c_D^0}{c_B^0 c_A^0} \exp\left(\frac{-\Delta G^0}{\mathrm{R}T}\right) \tag{4.12}$$

ΔG^0 is the Gibbs free energy at standard conditions, c_C^0, c_D^0, c_B^0 and c_A^0 thereby are the standard state concentrations for the following generic reaction:

$$\mathrm{A} + \mathrm{B} \rightleftharpoons \mathrm{C} + \mathrm{D} \tag{4.13}$$

For the calculation of the backwards reaction rate constants, the standard state concentrations are set according to the reactions shown in equation 4.2 to 4.4. All parameters are taken from the literature [72]. Further, the corresponding concentration of Li^+ within the SEI is minimal due to the assumption of electroneutrality and set to the small value of 3 mol/m^3.

The ion flux at the if/e interface generated from the reaction in equation 4.2 can be expressed with the following equation:

$$\begin{aligned} j_{Li,if} \;=\; & (1-\Theta) \cdot a_{s,if} \cdot c_{Li,e} \cdot k_{b,if} \exp\left(-\left(1-\beta_s\right)\Delta\Phi_{if} \frac{\mathrm{F}}{\mathrm{R}T}\right) \\ & -\Theta \cdot a_{s,if} \cdot k_{f,if} \exp\left(\beta_s \Delta\Phi_{if} \frac{\mathrm{F}}{\mathrm{R}T}\right) \end{aligned} \tag{4.14}$$

It has to be mentioned that the process might not be exponentially dependent on the overpotential but linear dependent instead. The interfacial Lithium-ion transport across the SEI/electrolyte interface $j_{Li,if}$ contributes to potential losses and at high frequencies to a dynamic response visible in the EIS. Despite its crucial influence on the spectra, the process and its kinetics have yet to be understood [87]. Heinrich et al. used a nonlinear approach for the current voltage relation. Nevertheless, it is mentioned that this relation could possibly be linear [10]. Since EIS works under the assumption of a linear system, it can not be used to determine if the process is linear or not. Indeed, no physical equation was yet presented in the literature, to model this process. Within this study a nonlinear dynamic measurement method is used to enable to study the process in detail, and which dynamic response would be expected for both theories, i.e. linear or nonlinear. Therefore, differences in the spectra due to a linear or nonlinear current voltage relation of the interfacial Lithium-ion transport across the SEI/electrolyte interface $j_{Li,if}$ are investigated. To account for this, a case study is set up within this work. For this, the nonlinear equation 4.14, which assumes an exponential dependency, is compared with the linear relation in equation 4.15. Here, as for the nonlinear relation, the potential difference at the interface $\Delta\Phi_{if}$ is the driving force for the process.

$$j_{Li,if} = a_{s,if} k_{if} \Delta\Phi_{if}, \tag{4.15}$$

with the transport rate coefficient k_{if}. For the case study all model equations remain the same, only equation 4.14 is changed to equation 4.15. Reasons for nonlinearity of this process may be the fact that the transported Lithium-ion needs to strip off its solvations shell and integrates into a Lithium-salt containing solid. The process may be linear as well, equivalent to a typical linear resistance for the transport of ions in the electrolyte. If it is not mentioned otherwise the nonlinear relation is implemented. The change of occupied surface sites is calculated according to equation 4.16.

$$\frac{\partial\Theta}{\partial t} = \left(j_{Li,a} - j_{Li,if}\right) \frac{\psi}{\Gamma} \tag{4.16}$$

Thereby, values of the site-occupancy number ψ and the site density Γ are taken from the literature [72].

In order to account for the internal resistance of the cell, the SEI thickness d_{SEI} is assumed to cause a potential drop, which is dependent on the conductivity σ_{SEI}:

$$\Delta\Phi_{SEI} = \frac{d_{SEI}}{\sigma_{SEI}} J_{\mathrm{Li}} \tag{4.17}$$

The thickness of the SEI, which is formed during the formation of the battery, is calculated according to:

$$d_{SEI,init} = \frac{V_{SEI} R_a}{3\varepsilon_{s,a} A_{cell} d_a} \tag{4.18}$$

An assumption, that 15 % of the Lithium, which deintercalates the cathode during the first charge will build up an initial SEI instead of intercalating into the anode, is used here [91]. This initial SEI is assumed to be composed of pure Lithium carbonate.

$$V_{SEI} = \frac{n_{loss} M_{\mathrm{Li_2CO_3}}}{2\rho_{\mathrm{Li_2CO_3}}}, \tag{4.19}$$

with the amount of lost mol Lithium n_{loss} and the molar mass and density of Lithium carbonate $M_{\mathrm{Li_2CO_3}}$ and $\rho_{\mathrm{Li_2CO_3}}$ respectively.

Since a completely new model is set up, model validation is essential. An in-depth description and the corresponding results are shown in the Appendix A.2. For further simulations, the parameters shown in Table 4.2 and Table 4.3 are used. It is has to be mentioned that the parameters related to the SEI process are adapted for the shown simulations towards smaller SEI resistances compared to the model validation in Appendix A.2. The cell shows an unproportionally big semi circle related to the SEI. To decrease this influence of a dominating SEI and to be able to study processes with similar resistances, this adaption is made.

Parameter	Anode	Separator	Cathode
Width δ / μm	$43.66^{(a)}$	$20.00^{(a)}$	$56.75^{(a)}$
Particle radius R_i / μm	$6.83^{(a)}$	-	$6.40^{(a)}$
Volume fraction solid ε_s / -	$0.35^{(b)}$	-	$0.33^{(b)}$
Volume fraction electrolyte ε_e / -	$0.60^{(b)}$	$0.5^{(b)}$	$0.57^{(b)}$
Maximal solid concentration $c_{s,max}$ / $\frac{mol}{m^3}$	$28605.42^{(b)}$	-	$50862.18^{(b)}$
Initial solid concentration, SOC 50 % / $\frac{mol}{m^3}$	25140	-	18296
Electrolyte concentration c_e / $\frac{mol}{m^3}$	$1000^{(a)}$	$1000^{(a)}$	$1000^{(a)}$
Transfer coefficients α / -	$0.50^{(c)}$	-	$0.50^{(c)}$
Electrolyte phase diffusion coeff. D_e / $\frac{m^2}{s}$	$2.6 \cdot 10^{-10\,(c)}$	$2.6 \cdot 10^{-10\,(c)}$	$2.6 \cdot 10^{-10\,(c)}$
Solid phase diffusion coeff. D_s / $\frac{m^2}{s}$	$2.0 \cdot 10^{-16\,(c)}$	-	$3.7 \cdot 10^{-15\,(e)}$
Transference number t_p / -	$0.37^{(c)}$	-	$0.37^{(c)}$
Bruggeman's exponent β / -	$1.50^{(c)}$	$1.50^{(c)}$	$1.50^{(c)}$
Electrolyte Conductivity σ_e / $\frac{S}{m}$	1.20	1.20	1.20

Table 4.2.: Base case model parameters: (a) measured, (b) calculated according to [28], (c) literature value from [5], (d) literature value from [6], (e) literature value from [28].

Parameter	if	SEI	Anode	Cathode
Double layer capacitance C_{DL} / $\frac{F}{m^2}$	$3.50 \cdot 10^{-3}$	-	17.89	1.70
nonlinear approach:				
Reaction rate constant k_f / $\frac{m^{2.5}}{mol^{0.5}s}$	3.90	$4.99 \cdot 10^{6}$	$1.0 \cdot 10^{-7}$	$2.05 \cdot 10^{-10}$
linear approach:				
Reaction rate constant k_f / $\frac{m^{2.5}}{mol^{0.5}s}$	$3.90 \cdot 10^{-13}$	$4.99 \cdot 10^{6}$	$0.5 \cdot 10^{-7}$	$2.05 \cdot 10^{-10} (= k_b)$
SEI conductivity σ_{SEI} / $\frac{S}{m}$		$8.76 \cdot 10^{-5}$		
SEI thickness d_{SEI} / m		$1.81 \cdot 10^{-7}$		

Table 4.3.: Kinetic model parameters [11].

Concerning the evaluation of NFRA, focus again is laid on the analysis of the first two individual higher harmonics Y_2, Y_3 as they show distinct different characteristic behavior [47, 9] and the rms Y_{rms} of these two harmonics, shown in equation 1.4. Once a system is excited with a sinusoidal input, it reaches for a steady-state [68]. This theoretically enables the possibility to characterize a system by differentiating between its first excitation and steady-state behavior as well as the transition in between, as schematically shown in Figure 1.8 and experimentally analyzed in Figure 4.2.

4.2. Experimental Investigation

A commercial Emmerich cell with graphite as anode and Nickel Manganese Cobalt Oxide (NMC) as cathode material in the 14500 format with a capacity of 800 mAh is investigated with an excitation AC amplitude of 2.9 C.

To evaluate the influence of transient behavior on NFRA, five different measurements

with varying number of evaluated output oscillations, always starting with the second oscillation, were performed. The exact oscillations are listed in Table 4.4. Measurements were repeated three times. For a more detailed description of the measurements, it is referred to [11][2].

Experiment	Output Oscillation
1	2
2	2-3
3	2-4
4	2-5
5	2-6

Table 4.4.: NFRA experiments with a variation of oscillations used to calculate the NFR response, measured on an Emmerich 14500 cell.

4.3. Results and Discussion

First, experimental studies are discussed to demonstrate transient cell behavior and its influence on NFR spectra. Then, simulation results concerning transient and steady-state behavior as well as the Lithium-ion transport process across the SEI/electrolyte interface and process characterization via parameter variation are investigated for further in-depth understanding of NFRA. If not mentioned otherwise, the nonlinear current voltage relation for the Lithium-ion transport across the SEI/electrolyte interface is used.

4.3.1. Experimental Analysis

For in-depth understanding and thus reliable and optimal usage of NFR spectra, differences between transient and steady-state behavior of the cell have to be understood. Therefore, the variation of the NFR spectra for different oscillations is investigated and results are shown in Figure 4.2. As priorly stated, the first transient oscillation of the measurement device is discarded.

In Figure 4.2 a), the sum of higher harmonics for a variation of the number of included output oscillations is shown, starting with the second oscillation (Exp. 1) and ending with the average of the first six oscillations (Exp. 5). As each measurement was repeated three times, the mean value is taken and error bars are additionally provided.

[2]Measurements were conducted by Nina Harting.

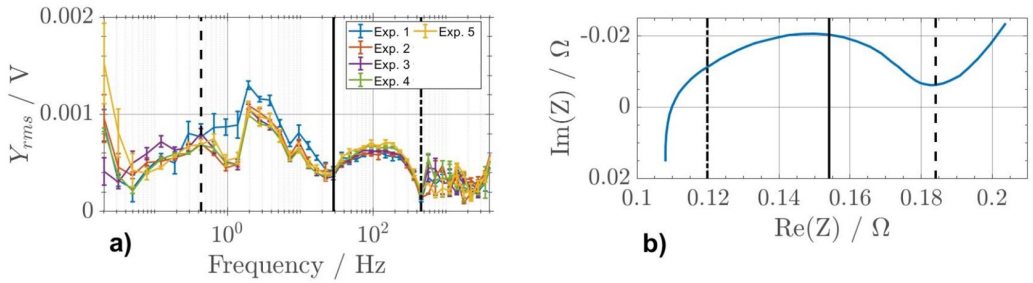

Figure 4.2.: a) Measured NFR spectra with Y_{rms} for various output oscillations according Table 4.4 and an AC amplitude of 2.9 C. Characteristic frequencies are at 0.5 Hz (dashed), 30 Hz (solid), 500 Hz(dash dotted). b) Measured EIS with AC amplitude 1/15 C at SOC 50% at T=25°C.

In the low frequency domain below 0.5 Hz, a significant increase of nonlinear voltage responses with increasing amount of output oscillation is visible. If frequencies smaller 0.5 Hz are measured, the open circuit voltage was observed to change during measurement with 0.05 V. This effect becomes stronger with the number of included oscillations, as priorly mentioned, due to longer measurement time and is therefore the reason for changing of nonlinear voltage responses. This phenomenon is attributed to the Coulomb efficiency of the cell, which is typically smaller than 1 [92]. With the number of investigated oscillations and a lowering of the input frequency, the measurement time increases, thereby lowering the potential of the cell and increasing the nonlinear voltage responses due to a potential shift. This phenomenon may also be attributed to balancing between electrode particles. All of the above leads to the conclusion that one has to be careful while measuring NFRA in the low frequency domain due as ageing of the cell may impact the spectra. In-depth analysis of this are the focus of ongoing research.

The area between 0.5 Hz (dashed line) and 30 Hz (solid line) is sensitive towards transient behavior. It clearly can be seen that with increasing number of oscillations, the nonlinear voltage response decreases. Already after two oscillations, an almost steady-state is reached. This frequency range corresponds to the lower frequency part of the semi-circle of the impedance spectrum, shown in Figure 4.2 b). This indicates strongly that this range should be attributed to the electrochemical reactions. Electrochemical reactions were indeed observed to show strong nonlinearities in this frequency range [47].

At frequencies higher than 30 Hz, a steady-state is already reached for the first inves-

tigated output oscillations. Whether the maximum at 100 Hz is caused by reactions or the SEI is open, though typical SEI frequencies are usually rather at 1000 Hz, suggesting the signal at 100 Hz should be rather attributed to a fast reaction at either anode or cathode. In that region, the NFR signal is rather smooth, while for frequencies above 300 Hz the signal becomes noisy and small. This range corresponds to the high frequency arc in the EIS, which is usually attributed to the SEI.

It can be concluded from experiments that changes in NFR due to transient behavior are significant. Transient effects influence the dynamic response mostly in the first two oscillations at medium frequencies, between 0.5 Hz and 50 Hz, but lead to drifting NFR for low frequencies in the diffusion affected area. This latter effect is not included in the model-based approach and is therefore not focus of these studies. All of the above is essential information for quantitative evaluation of NFR spectra.

4.3.2. Model-Based Study of Transient and Steady-State Behavior

Modeling allows in-depth analysis of the observed nonlinear, transient behavior. In the following section, the initial, transient response of the battery, the steady-state and the transition in between is further studied. Therefore, the SP model with a Solid Electrolyte Interface is applied. First, transient cell behavior is analyzed with NFRA and compared to EIS. For this purpose, the first oscillation of the output voltage, which can not be included in experimental studies with the present measurement device, is investigated concerning nonlinear voltage responses. At this point it is again mentioned that the SEI process is adapted for the shown simulations towards smaller SEI resistances compared to the model validation in Appendix A.2 to decrease the influence of a dominating SEI.

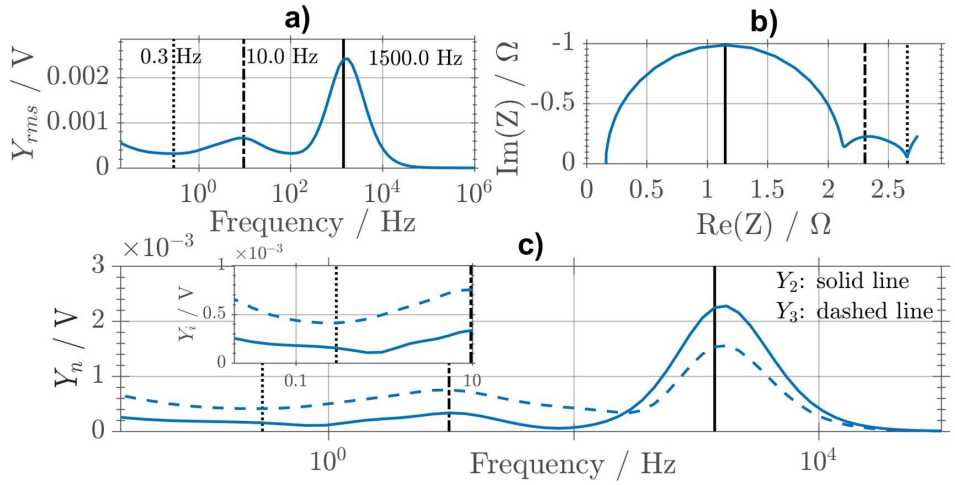

Figure 4.3.: Simulation results for a) Y_{rms} with AC amplitude 3 C for transient behavior, b) EIS with AC amplitude 1/15 C and c) individual higher harmonics Y_2, Y_3; SOC 50%, T=25°C.

In Figure 4.3, simulation results for a) the sum of higher harmonics, b) EIS and c) individual higher harmonics Y_2 and Y_3 are shown. Three characteristic frequency ranges are thereby identified. The highest peak at 1500.0 Hz for the sum of higher harmonics corresponds to the characteristic time constant of the high-frequency semi-circle in the impedance spectrum assigned to the SEI [10]. The spectrum shows a strong nonlinearity because of the assumed exponential correlation of transport into SEI and potential. This would not be the case for the model variant with linear approach in equation 4.15. Further, individual higher harmonics Y_2 and Y_3 show a distinct peak at this frequency. Both higher harmonics have the same dependency of frequency.

The peak for the sum of higher harmonics, at 10.0 Hz, is present at a frequency similar to the characteristic time constant of the small semi-circle in the impedance spectrum, corresponding to the electrochemical reactions. If individual harmonics are investigated, a maximal value for Y_3 can be seen whereas Y_2 is less sensitive in this range.

A small local minimum for the sum of higher harmonics and Y_3 is present at 0.3 Hz; Y_2 is less sensitive, visible in the inlet of Figure 4.3 c). This frequency range corresponds to the beginning of the diffusion part in the impedance spectra at the right hand side of the spectrum.

By investigating the transient NFRA deduced from the first oscillation, characteristic time constants as for the EIS were found. As priorly stated, the first output oscillation is discarded by the measurement device. Accessing time constants with transient behavior, as for the simulation would therefore require software and most probably

hardware modifications in the experimental device by the manufacturer. For reliable NFRA, thus, it is important to know how and when a steady-state is reached.

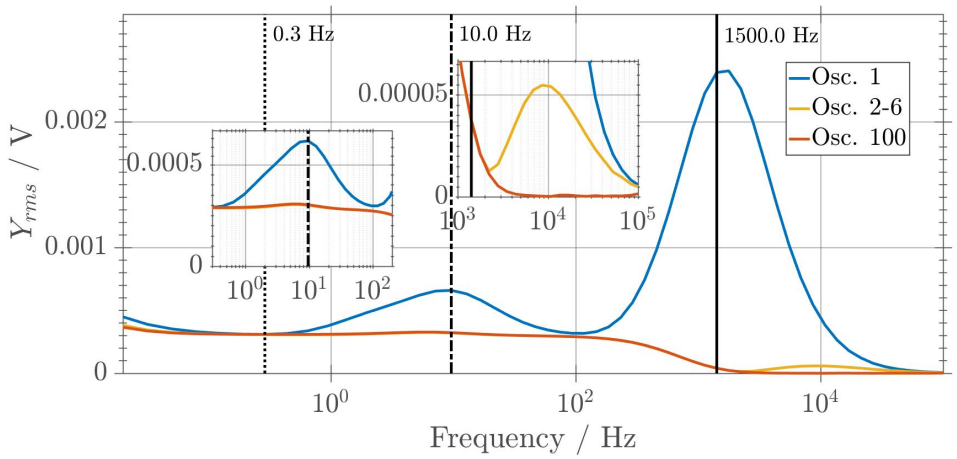

Figure 4.4.: Influences of transient and steady-state on NFR by investigating output oscillation 1, 2-6 and 100 with Y_{rms} at SOC 50% at T=25°C with AC amplitude of 3 C.

The influence of the number of oscillations considered for NFRA is investigated by simulating nonlinear responses for the 1st and 100th output oscillation and the 2nd to 6th oscillation in regard to the measured spectra. In Figure 4.4, the sum of higher harmonics is shown. NFR spectra reveal a significant transient behavior over the whole frequency range. Corresponding characteristic peaks at 10.0 Hz and 1500.0 Hz almost vanish for the 100th oscillation, as seen in the left inlet of Figure 4.4 and corresponding nonlinear voltage responses decrease. As it well can be seen, the characteristic frequency of the process shifts with the number of investigated oscillations towards higher frequencies. This phenomenon is clearly visible for the high frequency peak, attributed to the SEI. As corresponding instationary nonlinearities decrease, the underlying phenomenon becomes faster, thereby occurring at higher frequencies. After 100 oscillations, only steady-state behavior is present and a voltage response increase with decreasing frequency can be observed. This behavior differs from the experiment, where more distinct peaks in the steady-state can be observed. Previous studies showed that NFR spectra can significantly differ whether hand-made pouch cells or commercial cylindrical cells are investigated [9]. Concerning the low frequency domain, a steady-state is reached in the simulation, but not in the experiments as priorly discussed. It further can be seen that an implementation of the 2nd to 6th oscillation seems sufficient for steady analysis in the intermediate frequency range, both, in the experiment and simulation. Only in the high frequency domain around 1500 Hz in the

simulation the integral signal of oscillation two to six still shows transient behavior, though with a low amplitude, as shown in the right inlet of Figure 4.4.

For further deeper insight into cell processes and to determine when the steady-state is reached, solid concentration $c_{surf,a}$ at $r_a = R_a$ and double layer potentials $\Delta\phi_a$ and $\Delta\phi_{if}$ dependent on the number of output oscillations at the characteristic frequencies a) 0.02 Hz, b) 10.0 Hz and c) 1500.0 Hz are investigated in Figure 4.5. As shown in the literature, the cathode is not limiting for this cell configuration [10] and is therefore neglected in the interpretation of transient behavior. The relative intensity y_i/y_0 of the states $c_{surf,a}$, $\Delta\phi_a$ and $\Delta\phi_{if}$, is calculated by comparing the maximal excitation of the states for a given output oscillation relative to the corresponding value of the first output oscillation. The total value of the relative deviation does not indicate whether a process is linearly of nonlinearly excited. If a constant value is reached, the corresponding process is in its steady-state. Further, as priorly mentioned, processes shift towards higher frequencies with progressing number of output oscillations. The following investigation takes place at a constant frequency as the observed peaks emerge at a broad frequency range. This allows for a detection of instationary behavior, even if the maximum of the peak is not at the analyzed frequency.

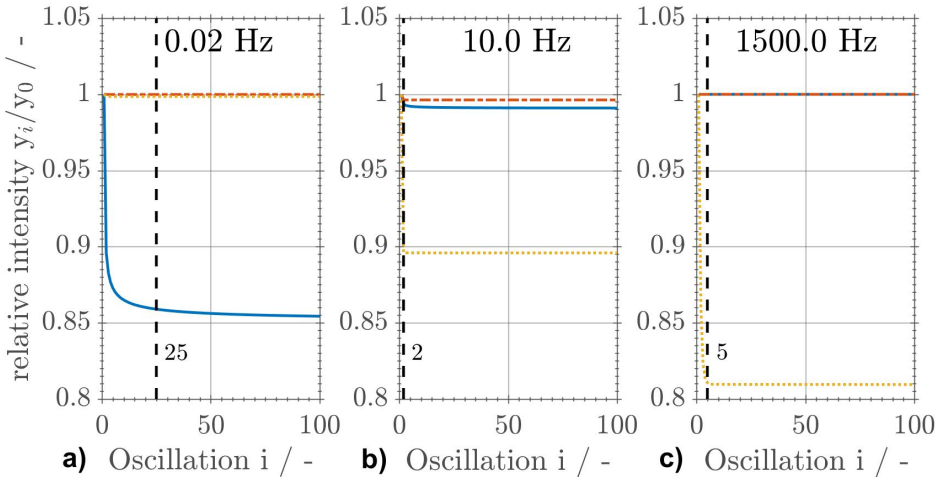

Figure 4.5.: Transient behavior of state variables: relative intensity for oscillation i to initial oscillation for boundary concentrations $c_{surf,a}$ (solid), double layer potentials $\Delta\phi_a$ (dash dotted), $\Delta\phi_{if}$ (dotted) dependent on number of output oscillations at a) 0.02 Hz, b) 10.0 Hz and c) 1500.0 Hz, for SOC 50% at T=25°C.

The relative intensity for the state variables at 1500.0 Hz is displayed in Figure 4.5 c). This frequency is assigned to the SEI and transient behavior can only be seen for the double layer potential $\Delta\phi_{if}$. Already after 5 oscillations, the potential and thus the

cell reaches equilibrium.

In Figure 4.5 b) also, the characteristic frequency for the electrode reactions at 10.0 Hz is investigated. It can be seen that not only the double layer potential at the anode $\Delta\phi_a$ is affected. Also, the SEI double layer potential $\Delta\phi_{if}$ is influenced. The relative deviation of the SEI double layer potential $\Delta\phi_{if}$ is higher compared to the double layer potential at the anode $\Delta\phi_a$. This can be explained by further investigating the impedance spectrum. The semi-circle corresponding to the SEI is almost one order of magnitude greater than the semi-circle of the anode reaction. Both double layer potentials reach their steady-state after two oscillations. Further, at 10.0 Hz, an influence of the anode boundary concentration $c_{surf,a}$ due to the commencing diffusion process is visible. The overall relative deviation of $c_{surf,a}$ is smaller than 1 % and therefore neglected concerning the determination of the steady-state.

At the lowest frequency of 0.02 Hz, an influence is only visible for the anode boundary surface concentration $c_{surf,a}$. After 25 oscillations, the steady-state is reached for this concentration. This leads to the assumption that more than the 2^{nd} to 6^{th} oscillation have to be included in the experiment. Nevertheless, according to Figure 4.4, the differences between spectra of the 2^{nd} to 6^{th} and the 100^{th} oscillation are minimal. Furthermore, in the experiment the low frequency domain is dominated by a potential change due to the Coulomb efficiency of the cell. Thus, 2^{nd} to 6^{th} oscillation are seen as a good compromise between both effects and thus a good choice conducting NFRA.

Overall, specific states show transient behavior, which is strongly correlated to NFR transient behavior. These states are the surface concentration $c_{surf,a}$ in the diffusion dominated regime at 0.02 Hz, which reaches a steady-state only slowly after approximately 25 oscillations, the $\Delta\phi_a$ and $\Delta\phi_{if}$ in the mid frequency domain, reaching a steady-state after 2 oscillations and $\Delta\phi_{if}$ in the high frequency domain with 5 oscillations until reaching a steady-state. For further simulations, a steady-state is assumed after 25 oscillations. However, as discussed above in case of experimental analysis, the 2^{nd} to 6^{th} has proven to be sufficient for steady-state analysis.

4.3.3. Differences in the Transport across the SEI/Electrolyte Interface

Nonlinear dynamic measurement methods allow for a deeper in-depth study of the transport of Lithium-ions across the interface of SEI and electrolyte compared to the conventional EIS [87]. Within this section, the nonlinear approach (equation 4.14) is compared to the linear approach (equation 4.15) by evaluating oscillation 25. The transport rate constant $k_{f,if}$ is set such that resistances of the linear and nonlinear approach are similar. Since the transport across this interface directly influences the coupled reaction (equation 4.5) via the interface transport layer, the corresponding reaction rate constant $k_{f,a}$ has to be adapted to yield the same resistance for a given SOC. Values for both reaction rate constants are given in Table 4.3.

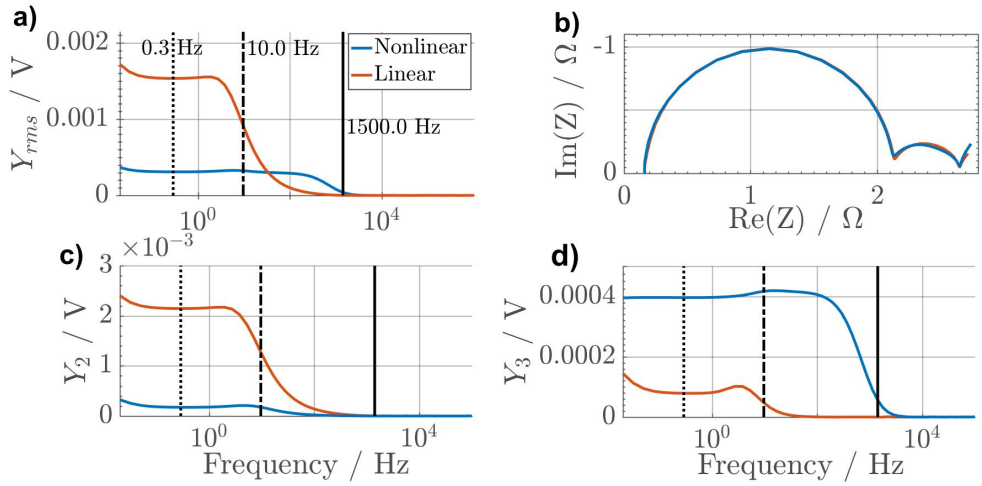

Figure 4.6.: Influence of the kinetic models (linear, nonlinear) for the SEI/electrolyte interface on cell dynamics: a) Y_{rms} with AC amplitude of 3 C, b) EIS with AC amplitude of 1/15 C, c) individual harmonic Y_2, d) individual harmonic Y_3, at SOC 50% at T=25°C.

In Figure 4.6 b), impedance simulations for both implemented approaches are shown. Due to the linear excitation of the system, no significant differences can be detected with EIS, only slightly smaller impedances in the low frequency domain, corresponding to the diffusion process are visible. If instead the sum of higher harmonics, shown in Figure 4.6 a), is investigated, significant differences between both spectra can be seen. For a detailed analysis, why the spectra are affected, individual harmonics have to be considered. Concerning the second harmonic Y_2, shown in Figure 4.6 c), a higher excitation due to the linear approach can be seen over the full frequency range. As priorly discussed, the approach for the Lithium-ion transport across the SEI/elec-

trolyte interface directly influences the coupled reaction. The coupled reaction is highly asymmetric and therefore majorly affects Y_2, according to [13]. Differences between both approaches are only of quantitative nature. If the third harmonic Y_3, shown in Figure 4.6 d), is investigated instead, essential information for the possibility to identify the kinetic across the interface is uncovered. It clearly can be seen that with the nonlinear approach, Y_3 is excited up to 1500 Hz and therefore at a higher frequency than with the linear approach. A linear process will not cause an excitation of higher harmonics in this SEI-specific frequency range. Further, a maximum is visible in the frequency dominated by anode reaction, at ca. 20 Hz, for the linear case. As the experiment shows such a maximum and a steep decline to small values at ca. 100 Hz, this might be a first indicator that the transport process is indeed a linear one. This model-based insight demonstrates that NFRA is an excellent tool to detect the nature of Lithium-ion transfer into the SEI. This is also supported by previous work [47, 64], where no clear nonlinearity at SEI typical frequencies around 1000.0 Hz was found. However, due to a noisy experimental signal at high frequency around 1500 Hz, a final conclusion can not be drawn yet; further experimental research with an improved, low noise setup is suggested. In this way, experimental NFRA will allow to determine the kinetics across this interface.

4.3.4. Process Identification

Prior model-based studies on NFRA applied to LiB focused on transient excitation for process characterization [9]. It is now aimed for further in-depth understanding of LiB by applying NFRA on a battery model with nonlinear SEI transport kinetics in its steady-state. Process identification with steady-state behavior is investigated by analyzing parameter sensitivity of the spectra, starting with the characteristic parameters of the SEI; its reaction rate constant $k_{f,if}$ and double layer capacitance $C_{DL,if}$ and the AC amplitude.

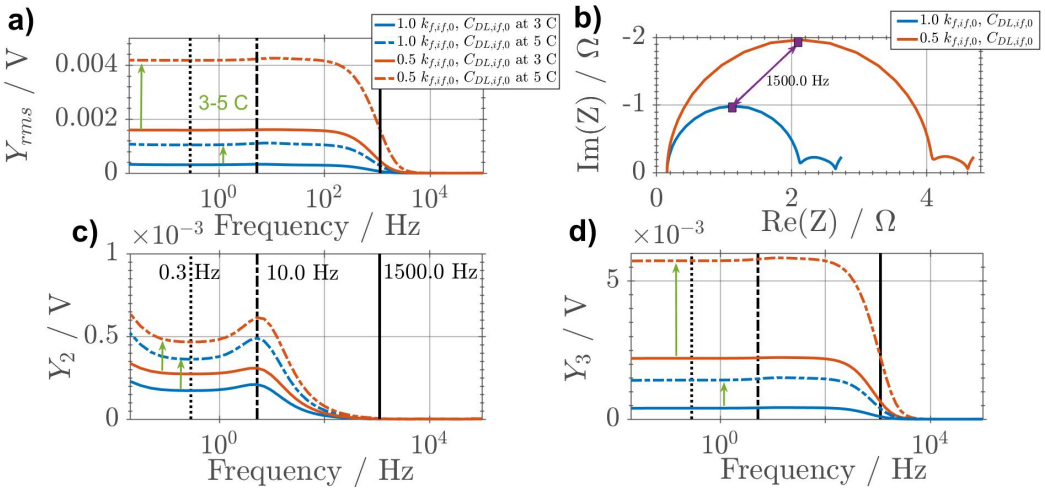

Figure 4.7.: Steady-state simulation results for NFRA for a) Y_{rms}, b) EIS with AC amplitude of 1/15 C, c) individual higher harmonic Y_2 and d) individual higher harmonic Y_3, for variation of SEI reaction rate constant $k_{f,if}$ and double layer capacitance $C_{DL,if}$ and AC amplitude, at SOC 50% at T=25°C.

A 50% decreased reaction rate constant $k_{f,if}$ and double layer capacitance $C_{DL,if}$ cause a twice higher impedance for the SEI process, visible by a two times larger corresponding SEI semi-circle. The characteristic time constant is constant, as halving $k_{f,if}$ doubles the SEI resistance, which is multiplied by a halved $C_{DL,if}$, leading to the same time constant. The effect on the sum of higher harmonics at steady-state is shown in Figure 4.7 a), for changing reaction rate constant $k_{f,if}$ and double layer capacitance $C_{DL,if}$ for AC excitation amplitudes 3 C and 5 C. A low reaction rate constant $k_{f,if}$ causes high overpotentials and therefore increases the resistance of the corresponding process. This leads to high nonlinear voltage responses within the overall frequency range. This effect is further increased for the high excitation amplitude of 5 C. In general, the characteristic frequency of 1500 Hz, taken from the impedance spectra, indicates the frequency where the excitation of nonlinear voltage responses starts.

The qualitative progression of individual higher harmonic responses, shown in Figure 4.7 c) and d), do not differ with the input amplitude, i.e. no new or shifted spectra, but show a quantitative dependency on SEI resistance and amplitude. As $k_{f,if}$ and $C_{DL,if}$ were found to decrease with ageing [10], it may be concluded that ageing of cells causes an increase in nonlinear voltage responses in the overall frequency range. This feature of the NFR spectrum has been used for SOH analysis [65].

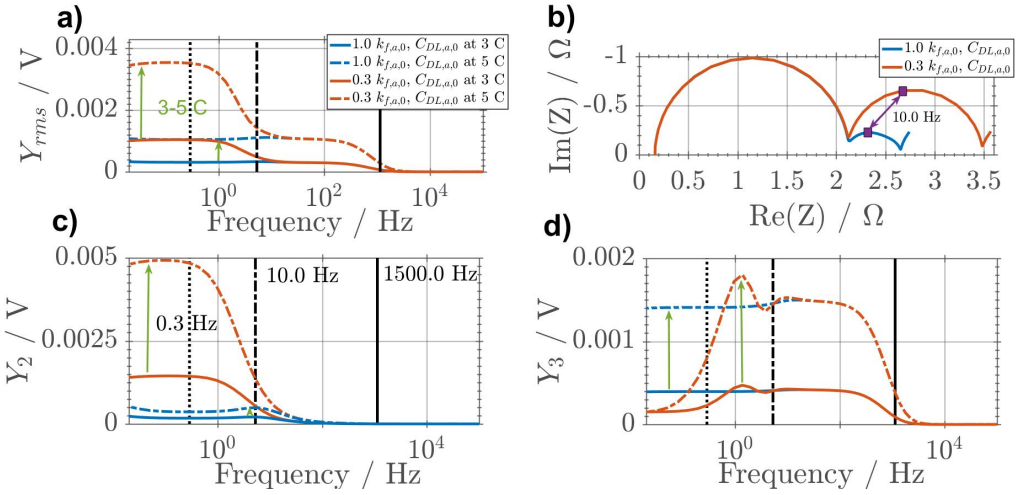

Figure 4.8.: Steady-state simulation results for NFRA for a) Y_{rms}, b) EIS with AC amplitude of 1/15 C, c) individual higher harmonic Y_2 and d) individual higher harmonic Y_3, for a variation of the anode reaction rate constant $k_{f,a}$ and double layer capacitance $C_{DL,a}$ and AC amplitude, at SOC 50% at T=25°C.

Subsequent to an investigation of the SEI, the impact of the anode reaction at steady-state on the NFR spectrum is investigated. Relevant parameters, thereby, are the reaction rate constant $k_{f,a}$, double layer capacitance $C_{DL,a}$ and AC amplitude. Simulation results are shown in Figure 4.8. Ageing studies showed that $k_{f,a}$ and $C_{DL,a}$ can be influenced simultaneously by an isolation of surfaces [10]. This is similar to a change of the specific surface area a_s in equation 3.6 and 4.5. With simultaneously decreasing $k_{f,a}$ and $C_{DL,a}$, the resistance of the anode reaction is increased and the time constant stays constant, thereby only the corresponding right semi-circle in the impedance spectra, shown in Figure 4.8 b), increases. Concerning the sum of higher harmonics, shown in Figure 4.8 a), a nonlinear voltage response increase for an increasing anode resistance is visible. Compared to an increased SEI resistance, not the overall frequency range is affected. A sensitivity is only visible for frequencies smaller than 10.0 Hz, which corresponds to the frequency range characterisistic for reaction and diffusion as known from the impedance spectra. This is expectable, as changes in the reaction rate constants are supposed to mainly affect the area characterized by reaction. Furthermore, the diffusion part is also impacted as the impact of diffusion on NFRA is mainly due to the concentration dependent reaction kinetics (equation 4.5), which is also impacted by $k_{f,a}$. In Figure 4.8 d), Y_3 shows a lower absolute sensitivity towards changes in the reaction resistance compared to Y_2 in Figure 4.8 c), but relative changes are significant. In contrast to the variation of the SEI parameters, dis-

tinct maxima get visible in the reaction-related frequency range. The lower reaction rate constant needs to be compensated by higher overpotentials to reach the same current. This leads to the observed stronger nonlinerities in this range and to local maxima as visible in the transient response at 10 Hz in Figure 4.3. At the anode side, a highly asymmetric coupled reaction is implemented. As the symmetry of a process influences the sensitivity of higher harmonics [13], new or shifted maxima can be expected. Due to this, one can clearly distinguish between the impact of changes of the anode and the SEI.

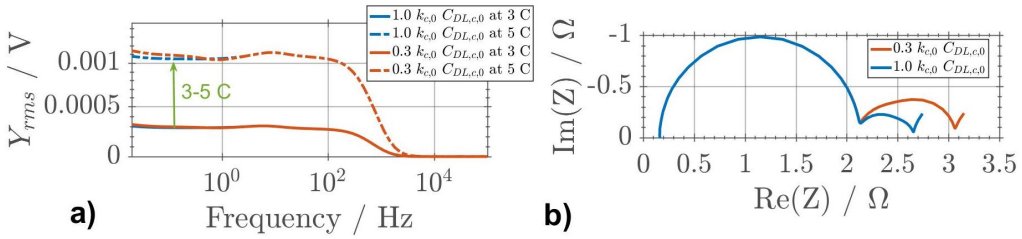

Figure 4.9.: Steady-state simulation results for NFRA for a) Y_{rms} for variation of cathode reaction rate constant k_c and double layer capacitance $C_{DL,c}$ and AC amplitude in comparison to b) EIS with AC amplitude of 1/15 C, at SOC 50% and T=25°C.

Similar simulations as for the variation of the anode reaction are investigated in Figure 4.9, but for the cathode reaction. An increased size of the smaller semi-circle can clearly be observed in the impedance spectra in Figure 4.9 b), if the reaction rate constant k_c and double layer capacitance $C_{DL,c}$ are lowered simultaneously to 30 %, which is equivalent to an isolation of 70 % of the surface area a_s; see equation 3.6 and 3.7.

However, the sum of higher harmonics, shown in Figure 4.9 a), shows almost no influence towards a change of the reaction in the cathode. This leads to the conclusion, that for the chosen case, the cathode reaction process shows linear response behavior and higher harmonic voltage responses and amplitude are not excited by a change in k_c and $C_{DL,c}$ for the chosen excitation amplitude. This enables further great potential for complementary diagnosis using a combination of NFRA and EIS.

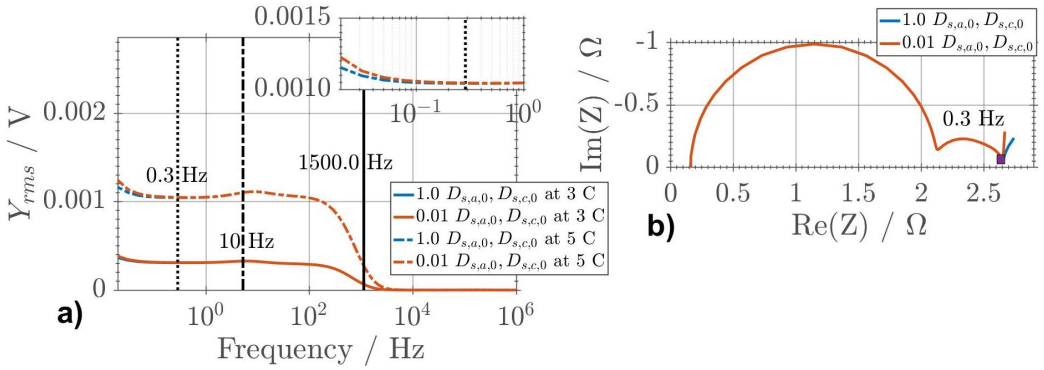

Figure 4.10.: Steady-state simulation results for NFRA for a) Y_{rms} for a variation of the anode and cathode diffusion coefficient $D_{s,a}$, $D_{s,c}$ and AC amplitude in comparison to b) EIS with AC amplitude of 1/15 C, at SOC 50% and T=25°C.

In a last step, in Figure 4.10, simulation results for the influence of the slow solid diffusion process in the anode and cathode on NFRA and EIS are shown. For the sum of higher harmonics, in Figure 4.10 a), smaller diffusion coefficients $D_{s,a}$, $D_{s,c}$ lead to higher nonlinear voltage responses only in the low frequency domain. This effect is minimal and only visible in the magnified inset for high excitation amplitudes. An excitation of nonlinear voltage responses due to the diffusion process is present, starting with the frequency of 0.3 Hz similarly as in the impedance spectra, as shown in Figure 4.10 b). Here the slope of the diffusion part increases with decreasing diffusion coefficients $D_{s,a}$, $D_{s,c}$ leading to almost capacitive behavior. Additionally, the reaction rate of the anode and cathode process are concentration dependent, thereby a decrease to 1 % for the diffusion coefficient might lead to insufficient Lithium transport to the particle surface and thus capacitative behavior.

4.4. Concluding Remarks

Focus of the research of this chapter was laid on model-based investigation of transient and steady-state behavior of a LiB by applying NFRA as experiments showed a deviation of the NFR spectra, if transient and steady-state signals are analyzed. To explain this behavior and correlate it to processes within the battery, the transition between initial excitation and steady-state was analyzed via a simulation based approach. For this purpose, a SP battery model, extended with a SEI was derived and applied. NFRA was thereby used to study the nature of the transport process across the SEI/electrolyte interface.

Simulations have shown that, in this case, after 25 oscillations, also the slowest process, solid diffusion in the anode reached a steady-state. This nonlinear behavior was shown to decrease significantly in the SEI and reaction dominated frequency range. Additionally, it was shown that NFRA is a highly promising tool to determine the yet unknown kinetics across the SEI/electrolyte (if/e) interface in future studies. Further, reaction rate constants k_i, double layer capacitances $C_{DL,i}$, diffusion coefficients $D_{s,i}$ and excitation amplitude were varied to identify the influence of battery processes on the spectrum at steady-state. It was shown that processes can be sensitive in the EIS, but not in the NFRA due to a linear excitation of the system. Additionally, individual higher harmonics show different sensitivities concerning nonlinear processes in the battery.

As well. these new findings concerning transient and steady-state simulations have to be brought into context to prior research of this thesis and the literature. In Chapter 3, the initial excitation of the system for process characterization with NFRA was used and strong agreement between measurement and simulation was found. Concerning the measurement, the 2^{nd} to 6^{th} oscillation were included and thereby still contained a transient part for the examined cell, though this part is mostly averaged out. It was shown that depending on cell chemistry, the NFR spectrum can highly vary. This approach is extended further and it is stated that the shape of the spectrum can also highly vary, if transient or steady-state behavior are analyzed. It is shown, that a major proportion of the transient part is already vanished after the 2^{nd} oscillation. Thus, for the given experimental conditions, a steady-state simulation in general is

closer to the measurement than a transient simulation. It is thus preferable.

In general, these results of the steady-state analysis are close to the investigation of singular processes in the first chapter. Especially, for a variation of the reaction rate constant k_{if} and double layer constant $C_{DL,if}$, increased nonlinear voltage response can mostly be attributed to the third harmonic Y_3, as priorly shown for a symmetric reaction according to Butler-Volmer kinetics. Additionally, changes of the diffusion coefficients $D_{s,i}$ change nonlinear voltage responses in the low frequency domain. All these findings are in great agreement with the examination of singular processes in Chapter 2. Deviations between results of Chapter 2 and this chapter, especially for changes of parameters of the reaction can be attributed to the more complex reaction process and coupling of processes, in general.

Overall, the possibility for process characterization is drastically enhanced by the possibility to differentiate between transient and steady-state behavior as well as the utilization of steady-state behavior with NFRA compared to only using conventional EIS.

After showing the general applicability of NFRA on current generation LiB with and without SEI and demonstrating its benefits, next, the rising topic of next generation ASSB with SIC electrolyte are discussed. Therefore, fundamental differences to current generation batteries are identified and discussed in detail before NFRA is applied to enhance process characterization of ASSB.

5 Process Characterization in Next Generation Lithium-Ion Batteries[1]

NFRA has shown to be a reliable tool and an excellent addition to conventional methods, such as EIS, for the characterization of processes in electrochemical systems. Within this Chapter, next generation batteries, in particular All-Solid-State batteries with a Single-Ion-Conducting electrolyte, are analyzed. For a sound analysis with NFRA, fundamental model differences to liquid, binary electrolyte Lithium-ion cells are derived and analyzed in-depth by simulations of discharge curves, EIS and NFRA. Sensitivity of both systems to key design parameters, such as electrolyte conductivity and electrode thickness, is shown. An in-depth literature review on ASSB and NFRA as well as the working principle of NFRA is provided in Chapter 1. Within this research, individual higher harmonics Y_n as well as the sum of higher harmonics NFR, are analyzed and interpreted.

Focus is laid on pure model-based analysis to allow for comprehensive and systematic comparison of both cell types. For this, the commonly applied P2D model is modified, to account for SIC electrolytes. This is enabled by assuming a Nernst-Planck flux and electroneutrality within the solid electrolyte phase. It is, to the authors best knowledge, the first time that bulk type full battery cells with SIC electrolytes are modeled with a P2D approach. Within this study, the effects of a SEI, which forms due to the electrochemical instability of the liquid electrolyte at the anode potential in the binary electrolyte model is neglected, since it has been studied extensively in the previous chapter. Further, by including a SEI, a model comparison using the results of Chapter 3 would be prevented.

Experimental validation is envisioned in future work, but requires significant effort in order to provide electrodes and cells with identical structure except for the replaced electrolyte to compare cells. In any case, as established battery models are used, the results should be reliable and give a first insight into what to expect as main differ-

[1] Parts of this chapter have been published in: Model Based Assessment of Performance of Lithium-Ion Batteries Using Single Ion Conducting Electrolytes, Electrochimica Acta, 284, 639-646, 2018 [12].

ences.

5.1. Modeling of a All-Solid-State Battery

A P2D model as presented by Legrand et al. [5], where a liquid and thus binary electrolyte is assumed and which is extended by a concentration dependent reaction rate from Colclasure et al. [6], is applied. Here, the same model as for the previous study is chosen.

Since most of the equations of the P2D model are applicable for binary and SIC electrolytes, those common equations are summarized in Table 5.1. Equation 3.1 and 3.2 are describing species transport and potential in the active material; charge balance, double layer charging and reaction are given in Equation 3.5, 3.6 and 3.7 with Equation 3.8, 3.9, 3.10, 3.14 and 3.15 giving the concentration dependent exchange current density i_0, overpotentials η_i, open circuit potential, specific surface area a_s and effective conductivity $\sigma_{s,eff}$. Note that for this comparative study, a Nernst-approach for open circuit potential is used and not experimental determined curves. This may result in deviations of simulations to experiments. Equations where the ASSB model deviates from the model for classical LiB, i.e. those for calculating electrolyte concentration c_e and potential ϕ_e, are derived for the binary and SIC electrolyte.

In Figure 5.1, processes of a cell using binary and SIC electrolyte are schematically illustrated. Anode and cathode active materials are considered to be Graphite and Lithium Iron Phosphate , since those materials are applicable to both, cells with liquid and solid electrolytes. Lithium concentration in the solid phase is spacially dependent on radial coordinate r. Potential in the solid and electrolyte phase as well as Lithium concentration in the electrolyte phase are dependent on spacial coordinate x.

Model Equations				Boundary Conditions
$\frac{\partial c_s(r)}{\partial t}$	$=$	$\frac{1}{r^2}\frac{\partial}{\partial r}\left(D_s r^2 \frac{\partial c_s(r)}{\partial r}\right)$	(3.1)	$\frac{\partial c_s(0)}{\partial r} = 0, \frac{\partial c_s(R)}{\partial r} = \frac{j_{\mathrm{Li}}}{a_s F}$
j_{tot}	$=$	$\frac{\partial}{\partial x}\left(\sigma_{s,eff}\frac{\partial \phi_s}{\partial x}\right)$	(3.2)	$\frac{\partial \phi_s(0)}{\partial x} = -\frac{\partial \phi_s(L)}{\partial x} = \frac{I}{A\sigma_{s,eff}}$
j_{tot}	$=$	$j_{\mathrm{Li}} + j_{DL}$	(3.5)	
j_{DL}	$=$	$a_s C_{DL}\frac{\partial\left(\phi_s - \phi_e\right)}{\partial t}$	(3.6)	
j_{Li}	$=$	$a_s i_0 \exp\left(\alpha\frac{\eta F}{RT}\right)$		
		$-a_s i_0 \exp\left(-(1-\alpha)\frac{\eta F}{RT}\right)$	(3.7)	
i_0	$=$	$k\mathrm{F}c_e^{\alpha}\left(c_{s,max} - c_s\right)^{\alpha} c_s^{1-\alpha}$	(3.8)	
η	$=$	$\phi_s - \phi_e - U_{OCV}$	(3.9)	
U_{OCV}	$=$	$U_0 + \frac{RT}{\mathrm{F}}$		
		$\ln\left(\frac{\left(1-\frac{c_{\mathrm{Li}^+}}{c_{\mathrm{Li}^+,max}}\right)\frac{c_{\mathrm{Li},^+,e}}{c_{\mathrm{Li},^+,e,0}}}{\frac{c_{\mathrm{Li}}}{c_{\mathrm{Li}^+,max}}}\right)$	(3.10)	
a_s	$=$	$\frac{3\varepsilon_{s,i}}{R_i}$	(3.14)	
$\sigma_{s,eff}$	$=$	$\sigma_{s,i}\varepsilon_{s,i}$	(3.15)	

Table 5.1.: Common equations for P2D model with binary and SIC electrolyte including boundary conditions.

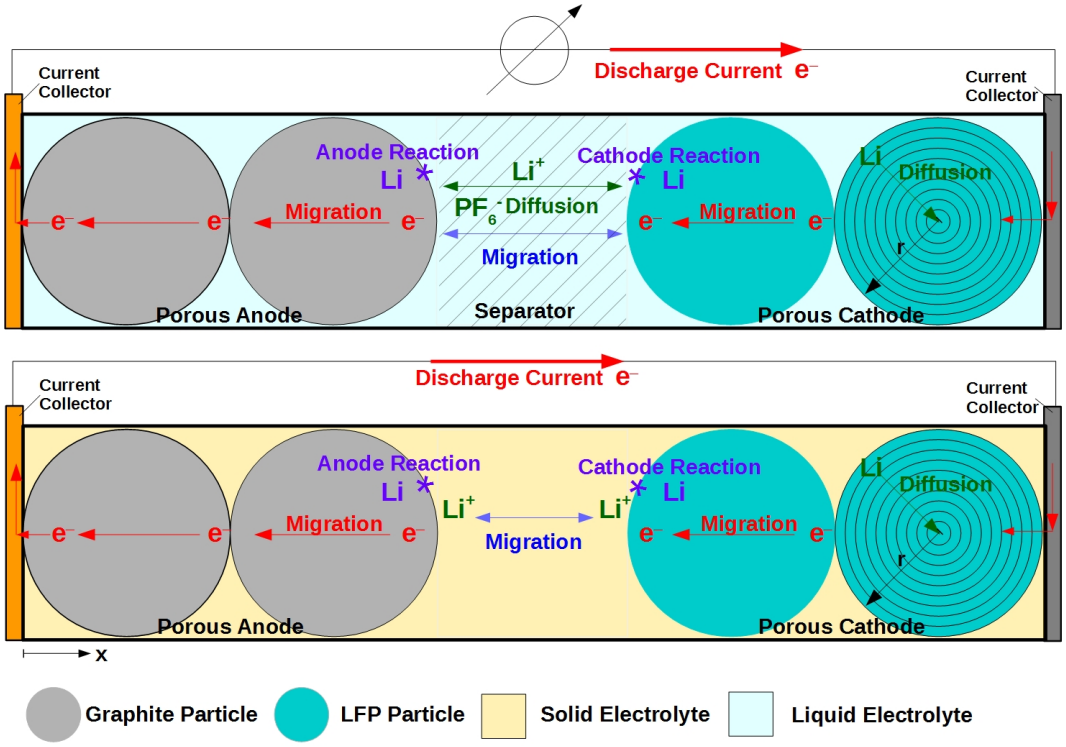

Figure 5.1.: Overview of processes in LiB cell with binary (top) and SIC electrolyte (bottom).

The species flux and the resulting molar balance of the charged species k through the electrolyte can be expressed in general as a Nernst-Planck flux without convection as [7]:

$$\frac{\partial c_k}{\partial t} = \underbrace{\frac{\partial}{\partial x}\left(D_k \frac{\partial c_k}{\partial x}\right)}_{\text{Diffusion}} + \underbrace{\frac{\partial}{\partial x}\left(D_k^{\text{mig}} \frac{\partial \phi}{\partial x}\right)}_{\text{Migration}} + \underbrace{R}_{\text{Reaction}}, \tag{5.1}$$

with ion charge z_k, diffusion coefficient D_k, Faraday constant F, concentration c_k, potential ϕ and the potential induced transport coefficient D_k^{mig} [7]:

$$D_k^{\text{mig}} = \frac{z_k F c_k D_k}{\text{RT}} \tag{5.2}$$

In a cell with SIC electrolyte only one charged species, Li^+, is mobile, whereas in a cell with binary electrolyte Li^+ and the counterion are mobile. For both systems, i.e. with binary and SIC electrolyte, electroneutrality $\sum z_k c_k = 0$ is assumed.

This denotes that for a binary electrolyte with two oppositely charged species Li^+ ($z_{\text{Li}^+} = 1$) and typically PF_6^- ($z_{\text{PF}_6^-} = -1$) the migration term of Equation 5.1 cancels out and further the concentrations c_{Li^+} and $c_{\text{PF}_6^-}$ and thus their corresponding time derivatives are equal:

$$c_{\text{Li}^+} = c_{\text{PF}_6^-} = c_e \tag{5.3}$$

For systems with binary electrolyte, the reaction term in Equation 5.1 equals the resulting ion flux j_{Li} in equation 3.7 divided by F. This results in:

$$\frac{\partial c_e}{\partial t} = D_e \frac{\partial^2 c_e}{\partial x^2} + (1 - t_p)\frac{j_{\mathrm{Li}}}{F}, \tag{5.4}$$

with the electrolyte diffusion coefficient D_e and transference number t_p, given according to Newman et al. [7], as:

$$D_e = \frac{2D_{\mathrm{Li}^+} D_{\mathrm{PF}_6^-}}{D_{\mathrm{Li}^+} + D_{\mathrm{PF}_6^-}}, t_p = \frac{D_{\mathrm{Li}^+}}{D_{\mathrm{PF}_6^-} + D_{\mathrm{Li}^+}} \tag{5.5}$$

Additionally, accounting for effects of porosity on diffusion, the effective diffusion coefficient is implemented via Bruggeman relation [5]:

$$D_{e,eff} = D_e \varepsilon_e^{\beta} \tag{5.6}$$

With this and the electrolyte volume fraction ε_e, Equation 5.4 can be written as equation 3.3 from Table 3.1.

Danilov et al. [76] use the assumption of mobile negatively charged vacancies and positively charged Li^+. In contrast to this, only one mobile species, Li^+ and therefore Lithium-ion hopping via lattice defects is assumed. With the assumption of only one mobile species and charge neutrality, there is no concentration gradient within the electrolyte:

$$\frac{\partial c_e}{\partial t} = 0 \tag{5.7}$$

The boundary conditions at the interface to the current collectors for the binary and SIC electrolyte are:

$$\frac{\partial c_e(0)}{\partial x} = \frac{\partial c_e(L)}{\partial x} = 0 \tag{5.8}$$

The electrolyte potential ϕ_e for both systems is expressed by a liquid junction potential as provided by Newman et al. [7]:

$$F\frac{\partial \phi_e}{\partial x} = -\frac{F}{\sigma_e} J - RT \sum_i \frac{t_i}{z_i} \frac{\partial \ln c_e}{\partial x} - RT \sum_i \frac{t_i}{z_i} \frac{\partial}{\partial x} \left(f_i - \frac{z_i}{z_n} \ln f_n \right), \tag{5.9}$$

with σ_e as the electrolyte conductivity, i as index of charged species and current den-

sity J. By neglecting idealities through activity coefficients $f_{i,n}$, the electrolyte potential ϕ_e can be expressed as:

$$\sigma_e \frac{\partial \phi_e}{\partial x} = -J - 2\frac{RT}{F}\sigma_e(t_p - \frac{1}{2})\frac{\partial \ln c_e}{\partial x} \tag{5.10}$$

Using a binary electrolyte, the conductivity σ_e can be calculated using the diffusion coefficients D_{Li^+} and $D_{\mathrm{PF}_6^-}$, according to a Nernst-Einstein relation and further assuming a Bruggemann relation to account for the effective conductivity $\sigma_{e,eff}$ [6, 5] as for equation 3.11, and shown in the following and therefore transforming equation 5.10 to equation 3.4 from Table 3.1.

Using a SIC electrolyte, there is no concentration gradient in the electrolyte, thus conductivity $\sigma_{e,eff}$ does not vary with spatial coordinate. As the electrolyte concentration c_e is initially homogeneous, Equation 5.10 can be simplified to:

$$\sigma_{e,eff} \frac{\partial \phi_e}{\partial x} = -J, \tag{5.11}$$

Thus, the electrolyte potential drop in Equation 5.11 considers only Ohmic losses. Further, for both models the potential boundary conditions are defined with a fixed potential at $x = 0$ and a potential gradient of zero at $x = L$ which leads to:

$$\phi_e(0) = 0, \ \frac{\partial \phi_e(L)}{\partial x} = 0 \tag{5.12}$$

To evaluate the differences between cells with SIC and binary electrolyte and thus compare their performance, parameters for the both have to be the same. Therefore, the electrolyte conductivity σ_e and diffusion coefficient D_e are set equal for the battery models. Both models are implemented in MATLAB. The spacial discretization of the partial differential equations takes place with a finite volume approach and the time derivatives are solved with an embedded ode solver. Further, all simulation parameters and initial values are taken from literature [5, 93, 94, 95, 96] and listed in Table 5.2. Thereby, the electrode width δ is chosen freely, the electrolyte diffusion coefficient D_e is adapted to guarantee a limiting electrolyte and the cathode reaction rate is calculated using the exchange current density from [93] and applying Equation 3.8. Additionally, all simulations refer to a pouch cell with an area of A_{cell} =0.0025

m^2.

Parameter	Anode	Seperator	Cathode
Width δ / μm	75	45	75
Particle radius R_i / μm	1	-	0.7
Volume fraction solid ε_s / - [5]	0.580	-	0.500
Volume fraction electrolyte ε_e / - [5]	0.332	0.500	0.330
Max. solid concentration $c_{s,max}$ / mol m^{-3} [5, 95]	16100	-	22800
Electrolyte concentration c_e / mol m^{-3} [5]	1200	1200	1200
Transfer coefficients α / - [5]	0.5	-	0.5
Solid phase diffusion coeff. D_s / m^2s^{-1} [5, 93]	$2{\cdot}10^{-16}$		$8{\cdot}10^{-18}$
Electrolyte phase diffusion coeff. D_e / $m^2s^{-1}13$ [5]	$0.39{\cdot}\ 10^{-10}$	$0.39{\cdot}10^{-10}$	$0.39{\cdot}\ 10^{-10}$
Electronic conductivity σ_s / Sm^{-1} [5, 96]	100	0	10
Transference number t_p / - [5]	0.363	0.363	0.363
Bruggeman's exponent β / - [5]	1.5	1.5	1.5
Double layer capacitance C_{DL} / F m^{-2} [5]	0.2		0.2
Reaction rate k / $m^4mol^{-1}s^{-1}$ [94, 93]	$5.03{\cdot}10^{-12}$	-	$1.31{\cdot}\ 10^{-11}$

Table 5.2.: Base case parameter simulation set for a binary electrolyte.

For model comparison, EIS with an AC amplitude, guaranteeing linear excitation of the system, e.g. 1/15 C at a state of charge (SOC) of 85% is simulated. Further, discharge curves and energy of the cell with a high discharge rate of 5 C and NFRA, to demonstrate electrolyte limitations in the cell with binary electrolyte, are investigated. Impedance results are divided by cell area to offer the possibility to be independent from cell design.

5.2. Results and Discussion

In this section, first, a binary and a SIC electrolyte battery model are compared. Then, sensitivities are analyzed via simulation of variations of electrolyte conductivity and electrode thickness with both models. Where possible, simulation results are brought into context of experiments from the literature. Nevertheless, bulk type ASSBs with SIC electrolytes are still difficult to manufacture and are therefore rarely addressed.

5.2.1. Comparison of Cells with Binary and Single-Ion-Conducting Electrolyte

In Figure 5.2, simulation results for both models with EIS a) and discharge curves b) are shown.

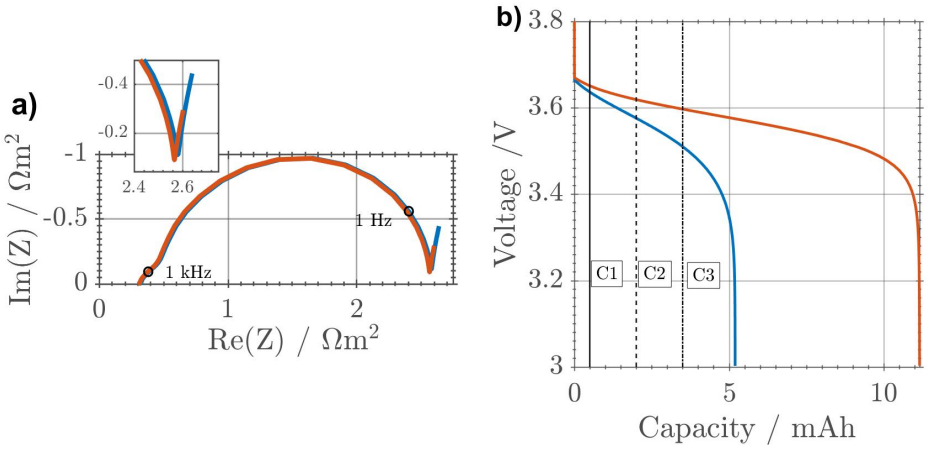

Figure 5.2.: Simulation results for a) EIS at SOC 85% and b) discharge curves with 5 C for a battery with binary electrolyte (blue) and a SIC electrolyte (red) at T=25°C with marked capacities C1 = 0.5 mAh (solid), C2 = 2.0 mAh (dash), C3 = 3.5 mAh (dash-dot).

The value at the intersection of the impedance spectra with the real axis corresponds to the internal resistance of the battery cell. It can be seen that the internal resistance does not significantly deviate between both models. This is attributed to the fact that equal electrical conductivity σ_e is assumed. Further, the EIS includes charge transfer processes at anode and cathode. Those processes appear as semi-circles in the impedance spectra. In the results shown here, two semi-circles can be seen. The small semi-circle at higher frequencies corresponds to the cathode reaction and the large semi-circle at the lower frequency range corresponds to the anode reaction. Both semi-circles merge at intermediate frequencies. Differences between both models can only be detected in the low frequency range on the right hand side of the spectrum which can be assigned mostly to diffusion processes of Lithium in anode and cathode active material particles. Results for the binary electrolyte have a larger impedance in the diffusion dominated range compared to SIC electrolytes. This is due to the absence of diffusion processes in the SIC electrolyte which leads to an absence of a concentration gradient in the solid electrolyte itself and thus an influence on the solid diffusion process.

In Figure 5.2 b), simulation results for discharge curves are shown for both models. As can be seen, the discharge capacity differs significantly: It is higher for batteries with SIC electrolytes. Comparing impedance spectra and the discharge curves, a higher impedance in diffusion is correlated to potential losses in the discharge curve. This is due to higher kinetic losses in the diffusion processes and thus leads to an overall lower total capacity of the cell. These findings are in agreement with the literature, Kato et al. [97] stated a very high applicable current density for SIC electrolytes. Ogawa et al. [98] further show that the discharge capacity of a SIC electrolyte cell barely changes for an increase of the C rate from 0.5 C to 24 C.

In order to provide detailed physical explanations for those findings, cell states are analyzed at the discharge capacities C1, C2 and C3 marked in Figure 5.2.

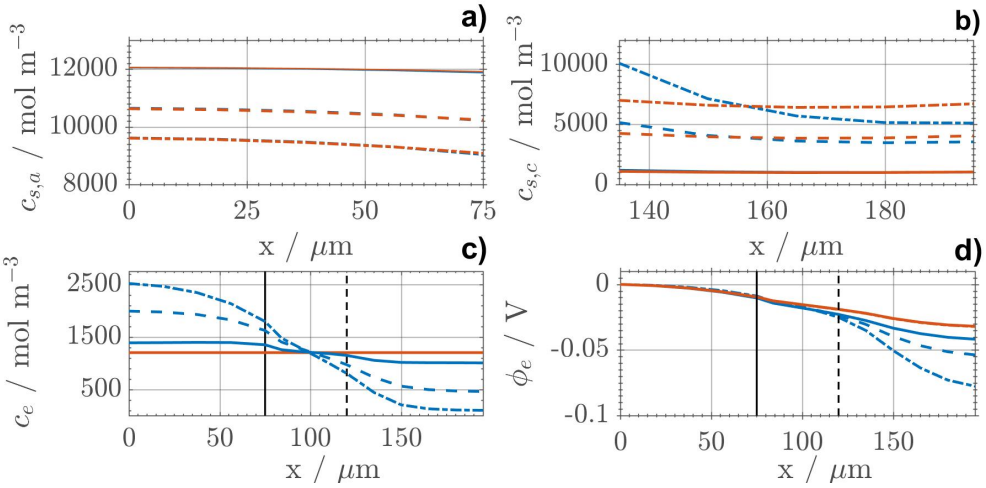

Figure 5.3.: Cell states as a function of space for cell model using binary electrolyte (blue) and SIC electrolyte (red), for a) the anode $c_{s,a}$ and b) cathode $c_{s,c}$ active material boundary concentration, c) concentration c_e and d) electrolyte potential ϕ_e over the whole crosssection extracted at capacities C1 = 0.5 mAh (solid), C2 = 2.0 mAh (dash), C3 = 3.5 mAh (dash-dot) at T=25°C, the vertical solid and dashed black lines in c) and d) show the boundary of anode and cathode, respectively.

The Lithium concentration $c_{s,a}$ at the particle surface of the anode is shown in Figure 5.3 a). For both models the concentration decreases in x-direction, i.e. particles are discharged earlier close to the separator. At the discharge capacity C_1 only a slight difference in the concentration between both models can be seen. The difference between the models becomes more distinct at the higher discharge capacity C_3. The concentration gradient is larger for binary electrolytes near the electrode/separator interface. This effect becomes stronger during discharge. As can be seen in Figure 5.3 b), for the cathode surface concentration similar observations can be made; however,

the deviation between the models is even more distinct. The observed uneven discharge in the electrodes can be explained by analyzing the electrolyte concentration c_e which is shown in Figure 5.3 c). It can be seen that with a binary electrolyte during the discharge, a concentration profile is established, while with the SIC electrolyte the concentration is constant. This difference arises from the assumption of a diffusion process according to Fick's second law for the binary electrolyte in Equation 3.3. In the SIC electrolyte with the assumption of an initially homogeneous concentration distribution and of immobile counter ions, no uneven Lithium-ion profile can be established, see also Equation 5.7. Local electrolyte concentration affects the local exchange current density of the electrochemical reaction. The spatial difference in electrolyte concentration thus causes spacial differences in current density and in solid concentration over the electrodes. This was observable also in the impedance spectra where differences in the diffusion related low frequency part were observable. Further, the electrolyte concentration affects the charge transfer in the electrolyte and thus impacts the electrolyte potential ϕ_e. In the results, the binary electrolyte cell shows a weaker performance due to higher Ohmic losses within the electrolyte itself. This directly causes the strong boundary concentration differences near the separator for both electrodes and leads to a lower capactity of the binary electrolyte cell.

In a next step model differences are elucidated with NFRA first in the transient and afterward in the steady-state. For all simulations, the SOC is set to 85% and the AC excitation amplitude to 4 C.

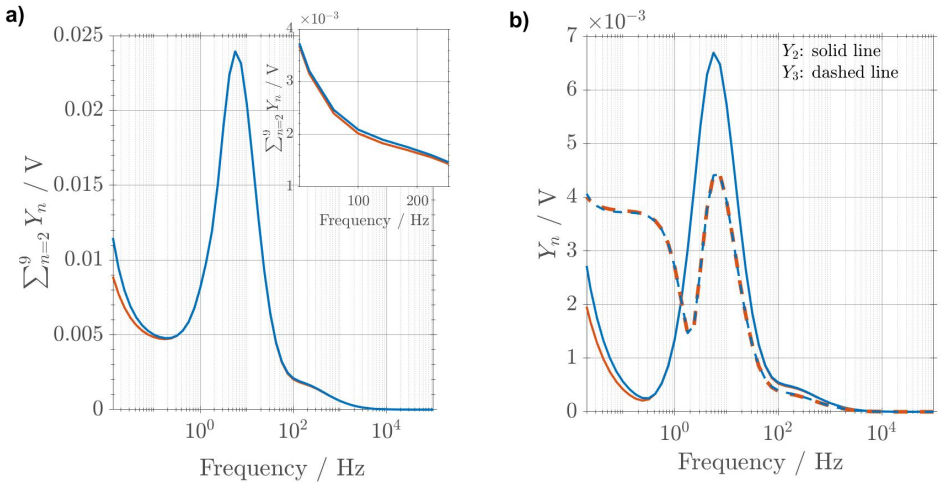

Figure 5.4.: Simulation results for NFRA for binary electrolyte cell (blue) and SIC electrolyte cell (red) for a) sum of higher harmonics including zoom in inset and b) individual harmonics Y_2 and Y_3 at SOC 85%. Further simulation parameters are provided in Table 5.2.

As for the investigation of both models with EIS, only minor differences can be detected with NFRA, shown in Figure 5.4 a), for the sum of higher harmonics. Nevertheless, due to a higher excitation amplitude, it is possible to detect an additional minimal difference in the mid frequency region, at approximately 100 Hz, characteristic for the electrochemical reaction of the cathode, shown in the inlet. Due to the concentration dependent exchange current density i_0 and electrolyte conductivity σ_e, within the binary electrolyte model, higher nonlinear voltage responses are present. These can, again, be observed in the low frequency range, characteristic for diffusion. If individual harmonics, Y_2 and Y_3, are investigated, shown in Figure 5.4 b), similar observations for model differences, as for their corresponding sum, can be made. In general, the qualitative progression of individual harmonics Y_2 and Y_3 is similar and independent from the type of electrode. Between Y_2 and Y_3, only differences in the frequency range between the reaction and the diffusion process can be detected. This part equals the characteristic excitation, previously described, for coupling of a diffusion and reaction process according to Butler-Volmer kinetics, in Chapter 2. Here, this behavior is superimposed by a transient part and therefore not as distinct visible as for the investigation of singular processes.

In a next step, model differences are elucidated with NFRA in the steady-state, not dynamic-state, following the conclusions from Chapter 4. The steady-state is assumed to be reached latest after 25 oscillations.

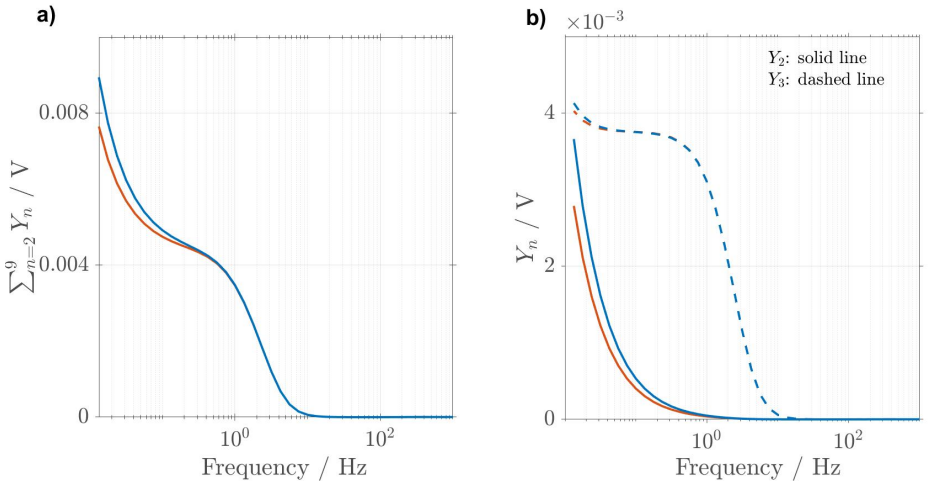

Figure 5.5.: Simulation results for NFRA in the steady-state for binary electrolyte cell (blue) and SIC electrolyte cell (red) for a) sum of higher harmonics and b) individual harmonics Y_2 and Y_3 at SOC 85%. Further simulation parameters are provided in Table 5.2.

Steady-state NFRA simulation results for the model comparison are shown in Figure 5.5 a), for the sum of higher harmonics. For the liquid electrolyte model, higher nonlinear voltage responses are excited in the low frequency region, characteristic for diffusion, compared to the ASSB model. For an explanation of this phenomenon, individual harmonics, shown in Figure 5.5 b), have to be investigated. It can be seen that the excitation of Y_3 is almost identical for both investigated models. This is in agreement with the transient simulation, shown in Figure 5.4. Y_2 on the other hand shows a higher response for the binary electrolyte model for the steady-state simulation, thereby explaining the higher sum of higher harmonics. This is identical to the simulation in the transient domain. Within the ASSB model, only Ohmic potential losses in the electrolyte and no influences of a concentration gradient in the electrolyte are present, thereby explaining the smaller excitation of higher harmonic voltage responses.

Concluding, differences between models with solid and liquid electrolyte can be seen due to the potential and concentration gradient in the electrolyte. Individual harmonics for both models, in general, show a behavior, well known from the simulation of singular processes in Chapter 2. Y_3 is excited, beginning at the characteristic frequency of the reaction processes. Due to the symmetric reaction, according to Butler-Volmer kinetics, Y_2 is barely excited in this region. Further, Y_2 and Y_3 are excited in the low frequency range due to the diffusion process.

The presented results for all simulations indicate that a SIC electrolyte can theoretically considerably improve cell performance via more homogeneous discharge in the electrodes due to the non-existing concentration gradient in the electrolyte. This is in agreement with the findings by Cao et al. [21]. Therefore, for identical conductivities, high energy batteries with thick electrodes and a SIC electrolyte can be discharged more homogeneously than liquid electrolyte cells; a benefit which increases with the C-rate.

5.2.2. Sensitivity to Electrolyte Conductivity

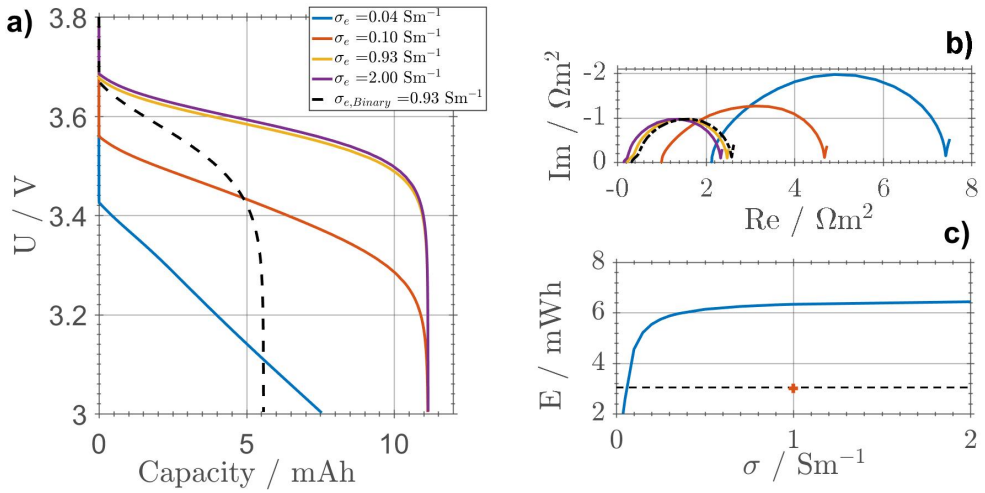

Figure 5.6.: Impact of conductivity σ_e of SIC electrolyte on a) discharge curves for a discharge rate of 5 C, b) EIS for the SIC electrolyte cell at SOC 85% and c) usable energy of cell (blue) with a discharge rate of 5 C, in comparison to binary electrolyte cell (red) $\sigma_{e,Binary}$ at T=25°C.

In the following, focus is laid on the impact of cell design parameters on cell performance to understand, if both cells react similarly to changes in cell and electrode parameters. This will yield important information on how best to optimize cells or which parameters should be adjusted or measured more carefully than others due to their impact on performance. This section targets the sensitivity to electrolyte properties, especially ionic conductivity, as there is a wide range of conductivities on the market to choose from, when building ASSB. In Figure 5.6, impact of electrolyte conductivity σ_e for a SIC electrolyte cell is shown and compared to the binary electrolyte cell with reference parameters from Table 5.2. According to Cao et. al [21] and Kato et. al [97], the electrical conductivity of actual glassy SIC electrolytes ranges from $\sigma_e = 0.04$ Sm^{-1} to $\sigma_e = 2$ Sm^{-1}, thus system performance is evaluated within this range. In Figure 5.6 a), discharge curves with a discharge rate of 5 C are shown. As can

be seen, the conductivity σ_e of the solid electrolyte considerably impacts discharge capacity. An evident impact is visible at the beginning of the discharge process. Here, a voltage decrease with conductivity σ_e is visible. This effect is discussed deeply for the investigation of impedance spectra. Compared to a binary electrolyte cell, simulated SIC cells reach a higher, almost constant total capacity even if the conductivity is lower by one order of magnitude. Similar as for the binary electrolyte cell, cell potential drops during discharge for the solid electrolyte cell. With a lower conductivity σ_e, the gradient becomes stronger and causes a change in slope of the discharge curve. If the conductivity is reduced significantly to $\sigma_e = 0.04\ \mathrm{Sm}^{-1}$, electrolyte losses within the cell affect the total capacity and only 55% of the capacity of the binary cell is reached.

In the impedance spectra, shown in Figure 5.6 b), it can be seen that the electrolyte conductivity σ_e impacts cell impedance. Decreasing conductivity σ_e leads to an increased internal resistance. A high internal resistance leads to high overpotentials and therefore an initial voltage drop as seen in Figure 5.6 a). The electrolyte conductivity σ_e further influences the local electrolyte potential ϕ_e and therefore directly the potential difference in the double layers. As a result, the impedances within the reaction and diffusion part of the spectrum increase with decreasing conductivity σ_e. In Figure 5.6 c), the usable energy of the cell is shown. It can be seen that for a discharge rate of 5 C, the SIC electrolyte significantly limits the cell performance for conductivities smaller than $\sigma_e = 1\ \mathrm{Sm}^{-1}$. Nevertheless, for conductivities greater $\sigma_e = 0.1\ \mathrm{Sm}^{-1}$, the usable energy surpasses the binary electrolyte cell with its reference conductivity of $\sigma_e = 1\ \mathrm{Sm}^{-1}$. Concluding, it is shown that even for conductivities lower than for a binary electrolyte cell, a SIC cell can reach higher capacities and usable energy at high discharge rates.

Next, the influence of the electrolyte conductivity σ_e on the excitation of higher harmonic voltage responses for the SIC electrolyte cell in comparison to the binary electrolyte cell is investigated with NFRA in the steady-state.

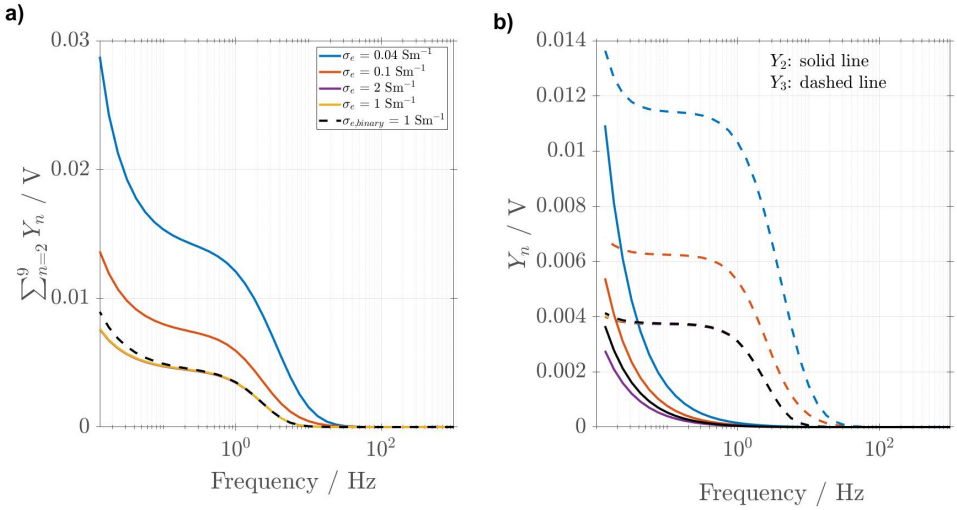

Figure 5.7.: Simulation results for NFRA in the steady-state for the SIC electrolyte cell for a variation of the electrolyte conductivity σ_e and the binary electrolyte cell for a) sum of higher harmonics and b) individual harmonics Y_2 and Y_3 at SOC 85%. Further simulation parameters are provided in Table 5.2.

In Figure 5.7 a), the sum of higher harmonics for a variation of the electrolyte conductivity σ_e for the ASSB model is shown. For conductivities σ_e higher than 1 Sm^{-1}, no nonlinear voltage responses are excited due to only minor potential gradients in the electrolyte. If σ_e is smaller than 1 Sm^{-1}, nonlinear voltage responses are excited in the overall excited frequency range. By investigating individual harmonics Y_2 and Y_3 in Figure 5.7 b), no further, new information can be acquired. Overall, it can be stated that processes in the electrolyte interact with all other processes and influence the overall excited frequency range.

5.2.3. Sensitivity to Electrode Design

One major disadvantage of binary electrolyte cells is a high electrolyte resistance, especially for cells with thick electrodes [99]. SIC cells are promising to overcome this drawback as shown in the previous section and also in [21]. Electrode properties may influence the ionic potential loss in electrodes. To quantify the impact of the electrode design on ASSB, electrode thicknesses d_a and d_c are varied simultaneously and simulation results of a) discharge curves with a discharge rate of 5 C, b) EIS, c) total energy and d) potential losses are compared to simulation results with binary

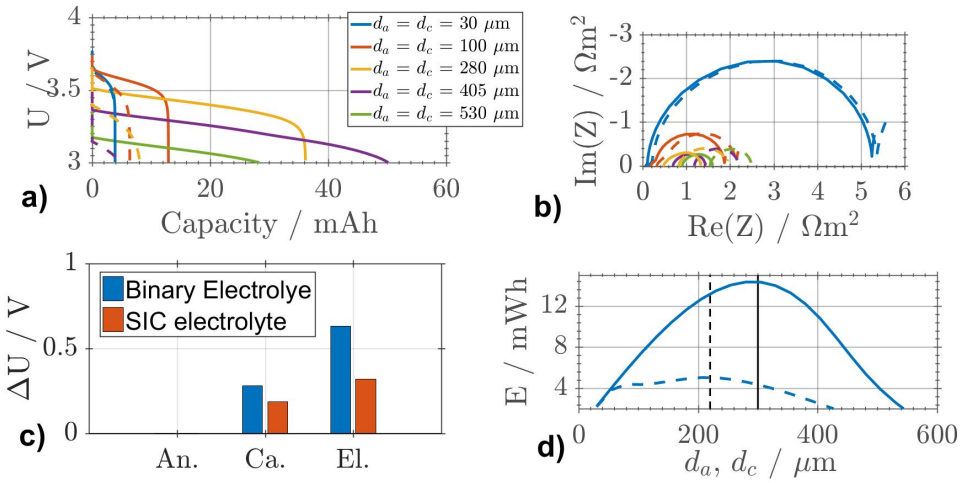

Figure 5.8.: Simulation results for simultaneous variation of anode and cathode thickness d_a, d_c for SIC electrolyte (solid) and binary electrolyte (dash) for a) discharge curves with a discharge rate of 5 C, b) EIS at SOC 85%, c) anode (An.), cathode (Ca.) and electrolyte (El.) increase in potential losses for increasing electrode thicknesses from $d_a = d_c$ =30 μm to $d_a = d_c$ =530 μm at discharge rate 5 C extracted at SOC 25% of the binary electrolyte cell and d) energy at T=25°C. Further simulation parameters are provided in Table 5.2.

electrolyte cells and shown in Figure 5.8. With increasing electrode thicknesses the theoretical capacity of the cell increases. The input current is related to the theoretical capacity of the cell. Therefore, with thicker electrodes, the input current and simultaneously overpotentials increase. This causes an initial drop of the potential, visible at a capacity of 0 Ah and a change of slope of the discharge curve, especially in case of a binary electrolyte cell, shown in Figure 5.8 a), as the electrolyte concentration profile causes more potential loss than solid state cells, as discussed previously. In the provided simulation results, the capacity of the SIC electrolyte cell increases up to an electrode thickness of $d_a = d_c$ =405 μm. For thicker electrodes, the electrolyte potential losses surpass the benefits of an increasing theoretical capacity and the total capacity decreases. In case of a binary electrolyte cell, similar observations can be made. A maximal capacity of ≈30% in comparison to the SIC electrolyte cell is reached at $d_a = d_c$ =280 μm. High electrolyte losses of the binary electrolyte cell, with its reference conductivity σ_e, are the reason for a low maximal capacity with a thinner electrode design as for SIC cells. Further, it can be stated that for thin electrodes, e.g. $d_a = d_c$ =30 μm, the electrolyte is not limiting the cell performance for the given C-rate and benefits of the SIC electrolyte cell almost vanish.

In Figure 5.8 b), simulated impedance spectra are shown. With increasing electrode

thicknesses d_a and d_c, the internal resistance of the cell increases due to an increased amount of electrolyte with a longer path length for Lithium ions and the low conductivity of the cathode active material σ_s. Further, the impedances related to the electrochemical reactions decrease due to the overall higher area for the reaction processes which leads to lower overpotentials for the same current. Impedance decrease is strongest between $d_a = d_c$ =30 μm and $d_a = d_c$ =100 μm, leading to the conclusion that for thin electrodes, the surface area for reaction is limiting and high impedances for solid diffusion due to higher current density are observed. As priorly stated, differences between cell designs are greatest for thick electrodes and almost vanish for $d_a = d_c$ =30 μm.

In Figure 5.8 c), the increase of potential losses for both cell designs, for an increase of the electrode thickness from $d_a = d_c$ =30 μm to $d_a = d_c$ =530 μm is shown. Losses are extracted after the binary electrolyte cell reaches a state of charge of 25%. It well can be seen that the anode has a minimal contribution to the overall potential losses due to its high conductivity $\sigma_{s,a}$. Highest impact have the cathode and electrolyte. With increasing thickness, losses are expected to drastically increase. This explains the observed impedance increase with increasing electrode thicknesses as priorly stated. Further, losses of the binary electrolyte cell surpass losses of the single ion conductor.

Finally, the overall usable energy of the cell for variation of electrode thicknesses is investigated and simulation results are shown in Figure 5.8 d). A distinct maximum for electrode thicknesses of $d_a = d_c$ =300 μm can be seen for the SIC electrolyte. This indicates that energy increases due to an increased amount of active material and decreases afterwards due to high transport losses. The binary electrolyte cell shows a similar trend, but with a maximal capacity at $d_a = d_c$ =230 μm of $\approx$37% in comparison to the SIC electrolyte cell.

In a last step, a variation of electrode thicknesses of anode d_a and cathode d_c, respectively, is investigated with NFRA.

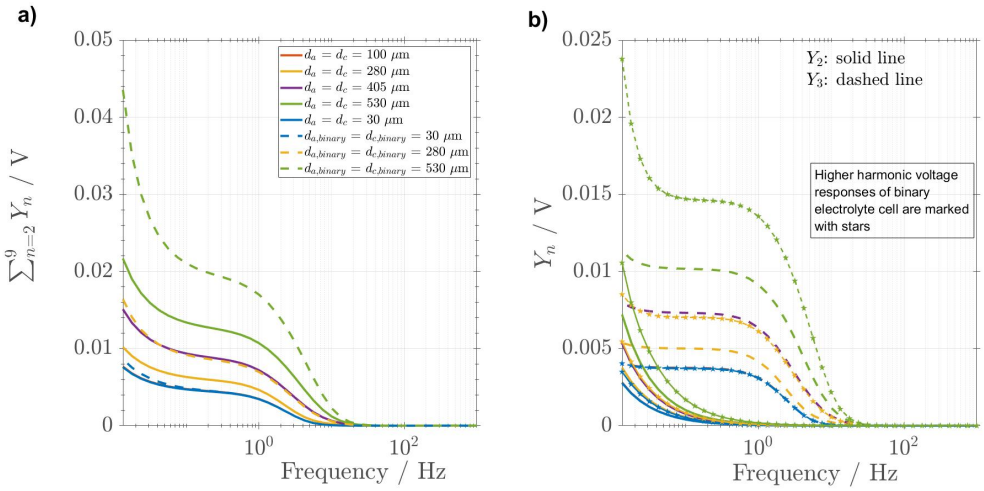

Figure 5.9.: Simulation results for NFRA in the steady-state for the SIC electrolyte cell for a variation of the anode and cathode thickness d_a, d_c for a) sum of higher harmonics and b) individual harmonics Y_2 and Y_3 at SOC 85%, compared to selected simulations for the binary electrolyte cell (marked with pentagrams for concerning individual harmonics). Further simulation parameters are provided in Table 5.2.

Simulation results for the sum of higher harmonics are shown in Figure 5.9 a). For thin electrodes ($d_{a,c} \leq 100$ µm), differences between the binary and SIC electrolyte model are minimal and an increasing electrode thickness does not cause an additional excitation of higher harmonics voltage responses as underlying processes are not rate determining (in-depth study on rate determining processes and corresponding excitation of higher harmonic voltage responses is provided in Chapter 4). These findings are in contrast to the investigation with EIS, shown in Figure 5.8, where, between $d_a = d_c$ =30 µm and $d_a = d_c$ =100 µm, the semi-circle corresponding to the reaction decreases due to the higher overall surface area with increasing electrode thicknesses. Due to the nonlinear excitation with a very high excitation amplitude, this effect is dominated by the higher resistance of the cell for thicker electrodes. This causes higher nonlinear voltage responses, analogously to the higher internal resistance, visible in the impedance spectrum and the initial potential drop, visible in the discharge curves. With further increasing thicknesses d_a and d_c, nonlinear voltage responses increase in the overall excited frequency range. Additionally, differences between the binary and SIC electrolyte cell become more significant as concentration gradients within the electrolyte and the electrodes increase with the thickness of the

electrodes and thereby cause higher overall nonlinearities for the binary electrolyte cell. In Figure 5.9 b), simulated individual harmonics Y_2 and Y_3 show the already well-known and priorly described characteristic progression for both kinds of investigated cells. Here, for a thick electrode design one can state higher nonlinear voltage responses for both individual harmonics concerning the binary electrolyte. Y_3 is thereby showing a more significant increase in dependence on the battery model, compared to Y_2. This may be attributed to the high concentration gradients in the electrodes, thereby decreasing the exchange current density i_0, analogue to the investigation of the exchange current density i_0 in Chapter 2. Due to thick electrodes, a shift of the beginning of an excitation of Y_2 towards lower frequencies due to higher concentration gradients in the electrode and electrolyte is present for the binary electrolyte cell.

The overall thickness variation of anode and cathode shows that SIC electrolyte cells theoretically allow a thick electrode design for high discharge rates and surpass the binary electrolyte cell in this case. Further, one has to differentiate between maximal capacity and energy concerning optimal electrode design. In total, this parameter variation shows that within the exemplary provided simulations, SIC electrolyte cells have a high capacity even for low amounts of electrolyte and high discharge rates.

5.3. Concluding Remarks

The model-based analysis focused on identification of fundamental differences between Lithium-ion cells with a binary electrolyte and a SIC electrolyte. Electrolyte model equations were thereby fully derived.

The results showed that potential losses in the electrolyte are more significant for binary electrolytes. Additionally, the electrolyte diffusion process in binary electrolytes causes concentration profiles which affect the performance of cells more strongly than the migration process with constant a concentration in the solid electrolyte. Both effects are leading to a lower maximal total capacity at thicker electrodes for the binary electrolyte cell. Model differences were investigated with NFRA, as well, first in the transient and afterwards in the steady-state, thereby elucidating higher nonlinear voltage responses for the binary electrolyte model in the frequency range, characteristic for the reaction and diffusion.

Even for lower conductivities than the binary electrolyte cell, the SIC electrolyte cell reaches a higher total capacity due to lower potential losses in the electrolyte. It was further shown that electrolytes should be chosen with a conductivity greater 0.1 Sm^{-1}, if high C-rates are applied to the cell. With increasing conductivity, the sensitivity to this parameter decreases. Higher harmonic excitation due to a changing electrolyte conductivity revealed similar information as the linear EIS. NFRA simulations thereby confirmed the prior findings.

It was further shown that one can theoretically produce SIC cells with thick electrodes and still apply high discharge rates. Nevertheless, NFRA reveals that the increasing resistance of the cell due to thicker electrodes can dominate other effects. Additional simulations for variation of active material volume fractions $\varepsilon_{s,a,c}$, electrode conductivities $\sigma_{s,a,c}$, cathode active material radius R_c, cathode reaction symmetry factor α_c and the SOC with NFRA are provided in the Appendix A.3.

Concluding, state-of-the art SIC electrolyte cells can theoretically surpass cells with binary electrolytes, especially for high discharge rates and a thick electrode design. A rigorous mathematical optimization of such cells may lead to identifying optimal electrodes regarding energy and capacity.

6 Conclusions and Outlook

6.1. Conclusions

Increasing demand for high energy LiB and fast charging possibilities make accurate and reliable understanding of underlying processes in LiB increasingly important. Dynamic measurement methods have proven to be helpful in this context. The most common method for process identification and characterization is EIS. Nevertheless, linear excitation of the system limits the accessible information. Therefore, this thesis is focused on a nonlinear method to determine additional characteristic information about processes in LiB, the so called NFRA, via a model-based approach.

NFRA uses information from nonlinear voltage responses, which are the voltage responses at multiples of the fundamental frequency. These occur, if the system is excited with a sinusoidal input current with high excitation amplitude.

Within the first Chapter of this thesis, understanding of this excitation due to electrochemical processes, i.e. a reaction process according to Butler-Volmer kinetics and spherical/planar diffusion was generated using simple generic electrode models. Results revealed that processes following a current-voltage relation symmetric to the center only cause an excitation of the third harmonic, whereas a current-voltage relation symmetric to the y-axis causes an excitation of the second harmonic. Further, a linear process, such as spherical diffusion, causes no excitation of higher harmonics. Only due to the concentration dependent open circuit potential, underlying the process, higher harmonics are excited. Concluding, the investigation of singular processes revealed the enormous potential of NFRA, since additional information to conventional methods, such as EIS, i.e. information about the symmetry of processes due to an excitation of the second harmonic, can be accessed. Therefore, the understanding of a complex system, such as a LiB, is drastically enhanced,

After generating fundamental understanding of the excitation of higher harmonics, in a next step, NFRA was applied to a state-of-the-art P2D-LiB model with a liquid electrolyte. Focus thereby was laid on parameter identification. If a complex system, such as a LiB, is excited with a sinusoidal current with high excitation amplitude,

it reaches for a new steady-state. Therefore, it is possible to differentiate between the transient excitation and steady-state. Within the investigation of the P2D battery model, only transient behavior was investigated. Results revealed similar time constants for EIS and NFRA. Further, comparison to measurements at different cell types and chemistries showed similar time constants and amplitudes for measured and simulated nonlinear voltage responses, indicating transient nonlinear content in measurements, as well.

An important characteristic of LiB, neglected so far, is the SEI. It is believed to be the dominating ageing effect for this battery type and its influence on nonlinear voltage responses has not been fully understood yet. Here, again, a model-based approach was chosen. Supporting measured spectra showed significant differences between transient and steady-state behavior. Therefore, understanding of the differences between these behaviors and how the steady-state is reached, is essential to understand processes in batteries and the excitation of nonlinear voltage responses. Due to this complexity, for this study, a SP battery model, extended with a SEI was chosen, derived and validated. With this SP-SEI model, differences between transient and steady-state were analyzed in-depth, thereby showing a steady-state after 25 oscillations for the chosen cell. Additionally, it was shown that NFRA can be used to determine the yet unknown kinetics across the SEI/electrolyte interface. Further simulations in the steady-state revealed that changes in the SEI process and changes in the electrochemical reactions influence nonlinear voltage responses starting at the characteristic frequency gathered from the impedance spectrum. In this way, they can be separated. Additionally, it was shown that it is possible that changes in processes show an influence in the impedance spectrum, but not in the nonlinear voltage responses, since the overall process change only impacts cell behavior on the linear scale.

Additionally to investigating current generation liquid electrolyte cells, an excursus towards next generation ASSB with SIC electrolytes was made. Thereby, fundamental differences were pointed out by model derivation and comparison. Simulation results of impedances and C-rate tests showed the enormous theoretical potential of ASSB for high discharge rates and thick electrode designs. Further, NFRA revealed higher nonlinear voltage responses for the liquid electrolyte cell in the frequency

range characteristic for the electrochemical reaction and diffusion, due to the concentration gradient in the electrolyte.

In Table 6.1, a selection of varied parameters and their influence on the excited frequency range as well as amplitude of higher harmonics is shown. f_{Y_2} and f_{Y_3} thereby mark the frequency for a beginning of higher harmonic voltage excitation. This table serves as a brief overview and indication of how processes affect higher harmonic voltage responses.

parameter/process:	state:	f_{Y_2}	f_{Y_3}	Y_2	Y_3	Chapter:
$I_A \uparrow$	steady	-	$\uparrow$	-	$\uparrow$	2
$C_{DL} \uparrow$	steady	-	$\downarrow$	-	-	2
$i_0 \uparrow$	steady	-	$\downarrow$	-	$\uparrow$	2
$\alpha \sim 0.5 \uparrow \downarrow$	steady	$\uparrow$	-	$\uparrow$	-	2
$I_{DC} \uparrow$	steady	$\uparrow$	-	$\uparrow$	$\downarrow$	2
$I_A \uparrow$	transient	-	-	$\uparrow$	$\uparrow$	3
$D_s \uparrow$	transient	$\uparrow$	$\uparrow$	$\uparrow$	$\uparrow$	3
$C_{DL} \uparrow$	transient	$\downarrow$	$\downarrow$	-	-	3
$k \downarrow$	transient	$\downarrow$	$\downarrow$	$\uparrow$	$\uparrow$	3
$R \uparrow$	transient	-	-	$\uparrow$	$\uparrow$	3
$D_e \downarrow$	transient	-	-	$\uparrow$	$\uparrow$	3
k,$C_{DL} \downarrow$	steady	-	-	$\uparrow$	$\uparrow$	4
$D_s \downarrow$	steady	-	-	$\uparrow$	$\uparrow$	4
Binary $\rightarrow$ SIC electrolyte	steady	-	-	$\downarrow$	$\downarrow$	5
$\sigma_{e,SIC} \downarrow$	steady	$\uparrow$	$\uparrow$	$\uparrow$	$\uparrow$	5
$d_s \uparrow$	steady	$\uparrow$	$\uparrow$	$\uparrow$	$\uparrow$	5

Table 6.1.: Summarized variation of parameters and their influences on the excitation of higher harmonic voltage responses

NFRA is a promising novel method for the characterization of LiB. This thesis aims to generate fundamental understanding of higher harmonic generation and interpretation in LiB. Thereby, NFRA has proven to have several advantages over common methods, such as EIS. These advantages are, among others, a) the detection whether changes in processes are linear or nonlinear, b) the possibility of process characterization via amplitude dependency and c) process characterization due to different sensitivities of individual harmonics. Concluding, process identification and separation can highly benefit from NFRA, especially in combination with EIS.

6.2. Outlook

Besides the efforts of this work, the field of understanding the generation of higher harmonic voltage responses is still very promising for future in-depth studies. This thesis serves as pioneering work on the application of NFRA on LiB. Concerning future research, one should separate the mid and long term goals. In the near future, the method itself should be strengthened and understood further. For this, half-cell measurements in combination with extensive temperature studies should be conducted. With this and further EIS measurements and discharge tests, it would be possible to exactly determine the kinetics of the transport process at the SEI/electrolyte interface, investigated in Chapter 4 as a model-based study. Further, NFRA can be applied to study effects like Lithium-plating or to study grain boundaries in ASSB, in a model-based approach. Further research on ASSB should thereby focus on the mentioned contact surfaces and effects of homogeneity of composition in the electrodes. As ASSB are suggested to be superior especially at high discharge rates, this might also suggest that they are more feasible for fast charging than classical LiB. This should be evaluated in further, similar, model-based studies.

Concerning long term goals, with rigorous and ambitious work, NFRA could further release its enormous potential. A possible application is the integration of NFRA in the battery management system of a vehicle. In combination with single cell control, a fast and reliable application oriented state-of-health determination and with this an optimal control of the cell to prolong its lifetime are possible. For this purpose, additionally, battery models can assist, but models are useless without solid paremetrization. NFRA can play an essential role in this accurate and unique parameter identification.

Generally, NFRA should be established as advanced diagnosis method for LiB and electrochemical systems in general.

A Supporting Simulations and Measurements

In the following, supporting simulations and measurements are provided. They are referred to at the corresponding passages of the thesis.

A.1. Influences of α and of a Pseudo-Concentration Dependent Exchange Current Density on NFRA

In addition to the analysis of fundamental processes in Chapter 2, a pseudo concentration dependent reaction rate constant is introduced to simply demonstrate the effect of a change of reactant concentration of the excitation of higher harmonic voltage responses. Further the effect of an in- and decreasing symmetry factor α on the excitation of higher harmonic voltage responses is enlightened.

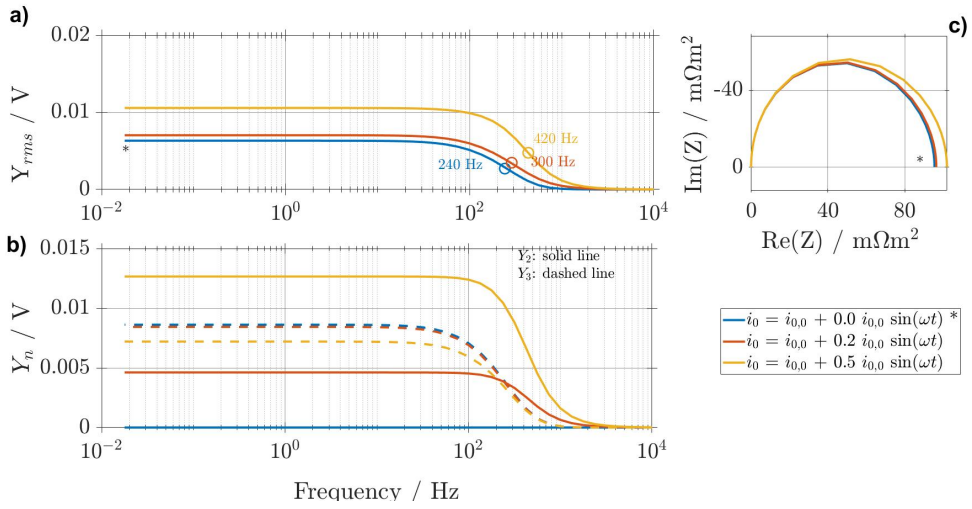

Figure A.1.: Simulated NFR for the reaction model with a pseudo concentration dependent exchange current density i_0 for a) Y_{rms}, b) individual harmonics Y_2 and Y_3 and c) EIS. The reference case simulation with parameters from Table 5.2 is marked with an asterisk.

Reactions in most electrochemical cells highly depend on the reactant concentration as reactants are consumed or produced by the reaction; the reactant concentration therefore changes sinusoidally with time. To account for this impact in a most generalized form with excluding diffusion processes to or from the electrode, a physically simplified and lucid approach is chosen to show the general impact of concentration on NFRA of the reaction process. Thus, a sinusoidally time dependent part is added

to the exchange current density i_0, which resembles consumption and production proportional to the consumption or production rate. It should be noted that in most technical systems, the concentration change causes a diffusion process to or from the electrode. This slow process may introduce a frequency dependent phase shift in concentration and thus in i_0. Please note that transport effects are analyzed in the next section.

In Figure A.1 a), Y_{rms} for a variation of the time dependent part of the exchange current density i_0 is shown. An increase of nonlinear voltage responses with an increase of the time dependent part is visible, as well indicated by an increased $Y_{rms}(f_{min})$. This phenomenon can be explained by investigating individual harmonics Y_2 and Y_3 in Figure A.1 b). If a time dependent part is added, the slope of current voltage relation due to the Butler-Volmer equation is varied constantly, therefore influencing the symmetry of the reaction, as priorly shown. This leads to an excitation of Y_2, thereby increasing the Y_{rms} nonlinearly and shifting the turning point as well as f_{min} and f_{max} towards higher frequencies. Further, a small decrease of Y_3 is visible. As for α, process identification can drastically benefit from these findings, since such characteristic changes in the spectra can not be observed with conventional methods, i.e. EIS, shown in A.1 c), where the spectrum is barely affected.

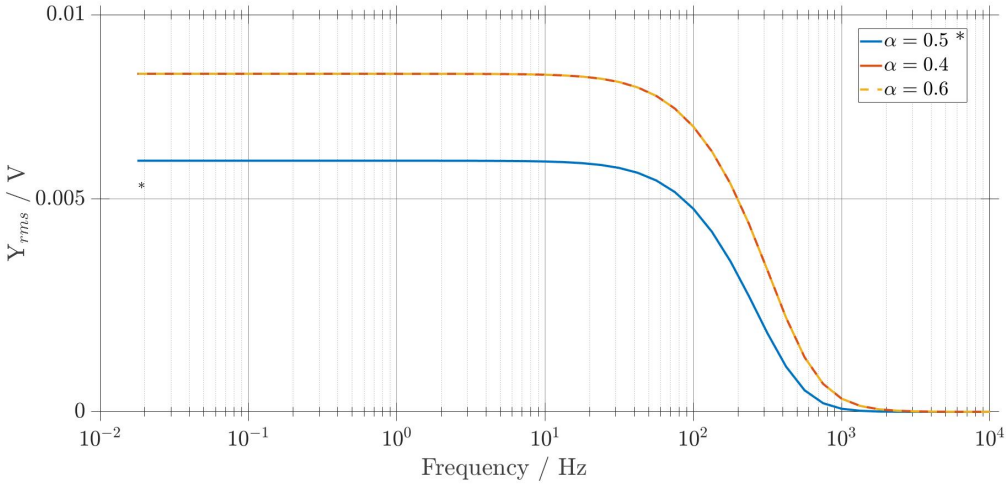

Figure A.2.: Simulated NFR for the reaction model with a variation of the symmetry factor α for Y_{rms}. The reference case simulation with parameters from Table 5.2 is marked with an asterisk.

In Figure A.2 Y_{rms} for an in- and decreasing symmetry factor α are shown. It well can be seen that if α is similarly in- or decreasing the excitation of higher harmonic voltage responses is identical since the shift of Butler-Volmer current voltage relation

is mirrored at $\Delta\eta = 0$ as shown in Figure 2.7 in Chapter 2.

A.2. Parameter Identification for Single Particle Battery Model[1]

PI for model validation of the SP-SEI model is conducted using a nonlinear least square trust-region-reflective algorithm embedded in MATLAB. The objective function $\chi^2(\omega, \vartheta)$, shown in equation A.1, contains the relative error for the real part of the measurement and simulation for the investigated frequencies ω_i of the part of the spectrum which is fitted. Using the real part of the impedance for the objective function was found to lead to better results than using an objective function combined of real and imaginary part or combined of phase and impedance. This is because of the use of a SP model instead of a more discretized model. A SP model calculates a defined deviation of the imaginary part of the impedance to the measured semicircles. Since this deviation is not physic-based but model-based, including the imaginary part or the phase of the impedance in the objective function will decrease the quality of the result. Therefore, the function which the MATLAB algorithm minimizes is:

$$\chi^2(\omega, \vartheta) = \min \sum_{i}^{k} \left| \frac{Re_{meas}^{\omega_i} - Re_{sim}^{\omega_i}}{Re_{meas}^{\omega_i}} \right| \tag{A.1}$$

where ϑ represents the parameters to be identified and k the number of frequencies.

Experimental Analysis with EIS

The pouch-cell used to obtain the experimental data for PI consists of NMC as cathode and graphite as anode material. Both electrodes have been produced in the Battery LabFactory Braunschweig. For a more detailed description and the measurement iteself it is referred to [10].

[1] Parts of this section are partially published in: Physico-Chemical Modeling of a Lithium-Ion Battery: An Aging Study with Electrochemical Impedance Spectroscopy, Batteries & Supercaps,2, 1-12, 2018, [10]. The initial parameter identification (PI) algorithm was set up by Nicolas Wolff. The PI itself was conducted by both authors of the paper. Measurements were thereby conducted by Nina Harting.

Identification of Kinetic Parameters

In a next step, kinetic and transport parameters of the model are identified using the parameters presented in Table 4.2 and the impedance measurement of the cell. For a more detailed description it is again referred to [10].

In addition to parameters from Table 4.2, Redlich-Kister parameters have to be provided for the calculation of activity coefficients of the Lithium γ_{Li} and the vacancies γ_V. They are shown in Table A.1.

B_1:	-35.80	B_7:	-28.79
B_2:	-35.01	B_8:	-14.98
B_3:	-35.25	B_9:	-39.91
B_4:	-35.69	B_{10}:	-96.17
B_5:	-38.63	B_{11}:	-63.26
B_6:	-35.91		

Table A.1.: Redlich-Kister parameters in kJ mol^{-1} [8].

PI is performed in order to determine unknown reaction rate constants $k_{f,a}$, k_c and $k_{f,if}$ as well as the corresponding double layer capacitances $C_{DL,a}$, $C_{DL,c}$ and $C_{DL,if}$. Additionally, the thickness of the SEI $d_{SEI,init}$ and the conductivity of the SEI σ_{SEI} are identified. The PI is performed stepwise in order to decrease the simulation time and to ensure uniqueness of the fit. Since parameters affect only a specific time constant of the spectrum, PI can be performed, beginning from high frequencies to low frequencies, without loss of accuracy.

Experiment and the resulting simulated EIS are shown in Figure A.3. The resulting values for the identified parameters are given in Table 4.3. At this point it is again mentioned that the SEI process is adapted for the simulations, shown in Chapter 4 towards smaller SEI resistances compared to the model validation in Appendix A.2 to decrease the influence of a dominating SEI. At the anode side, double layer capacitances at both interfaces of the SEI differ by more than four orders of magnitude, with the one of the electrolyte interface significantly smaller. This discrepancy is reasonable since the measured bigger semicircle has a much smaller time constant and is clearly separated from the low frequency semicircle. The double layer capacitance of the SEI is expectably much smaller than the anode double layer capacitance. For the reaction rate constants at the anode and SEI/electrolyte interface, no comparison with literature values is possible since a novel approach to couple the SEI reactions

according to equation 4.5 is used. The calculated cathode reaction rate constant is in agreement with the value presented by Colclasure et al. [8]. The simulation matches the internal resistance well but is not able to meet the imaginary part at the peak of the first semicircle. The Bode plots confirm this deviation and highlight that phase shift and impedance of the measurement are slightly shifted to higher frequencies in the range of the first semicircle. This deviation is attributed to the use of a SP model instead of a more discretised model. A SP model simulates one perfect charge transfer process on each electrode, whereas e.g. a P2D model or a model including a particle size distribution simulate one charge transfer process for each modeled particle. If the charge transfer processes in such a model occur at different time constants, e.g. due to different local overpotentials for each particle, the resulting semicircle in the Nyquist plot will be flattened, while semicircles simulated on a SP model are always unmodified. It should be noted at this point that using a P2D model does not lead to the mentioned distribution of time constants similar to the actual one in the cell. This can be seen in the results presented by Tippmann et al. [100]. The usage of a model including a particle size distribution would be sufficient. Using the introduced model, the first simulated semicircle includes only the time constant of the SEI/electrolyte interface process, rather than representing the actual distribution of time constants in the cell. Therefore, the flattening of the high frequency semicircle can not be reproduced perfectly. The algorithm for the PI is able to reproduce the low frequency semicircle well, since two time constants for the two main charge transfer reactions at anode and cathode are overlying in this frequency range. Another deviation is visible at the diffusion part of the impedance spectrum at low frequencies. Due to the low slope of the anode OCV-curve, the anode does not show any diffusion impedance [101]. The remaining cathode diffusion impedance, simulated with a SP model, increases with a similar slope as the measurement. These findings are in great agreement with the literature [78]. Nevertheless, the maximal value of real and imaginary part of simulation and measurement are not matched well. This can be attributed to the systematics of the SP model as priorly described by including a particle size distribution one would be able to influence the length of the diffusion part and to account for this effect.

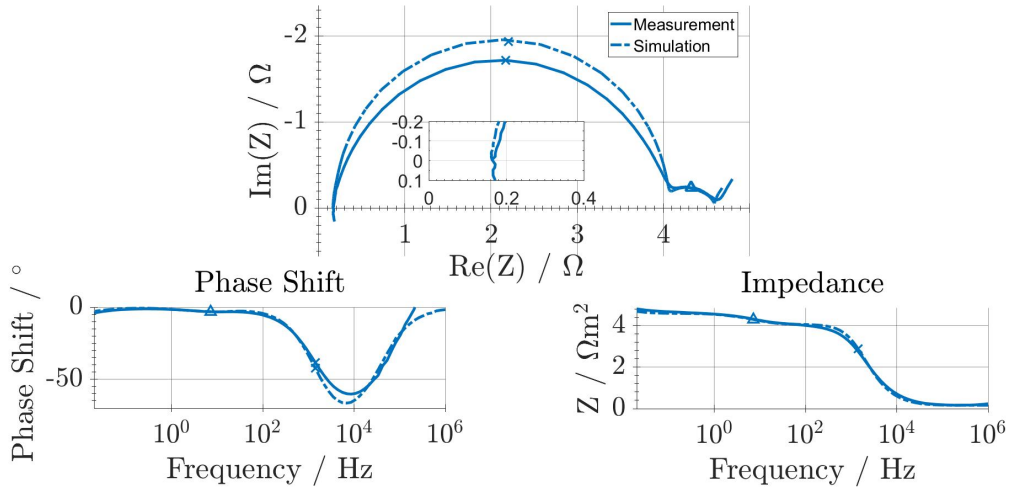

Figure A.3.: Experimental (solid line) and simulated (dashed line) EIS for an unaged LiB at SOC 50% and T=25 °C. ✕ and △ indicate impedance points at 1.4 kHz and 7.2 Hz respectively.

A.3. Simulations of All-Solid-State-Batteries in the Steady-State with NFRA

For further simulations in addition to Chapter 5, focus is laid on steady-state NFRA simulations. A variation of active material volume fractions $\varepsilon_{s,a,c}$, electrode conductivities $\sigma_{s,a,c}$, cathode active material radius R_c, cathode reaction symmetry factor α_c and the SOC, is investigated.

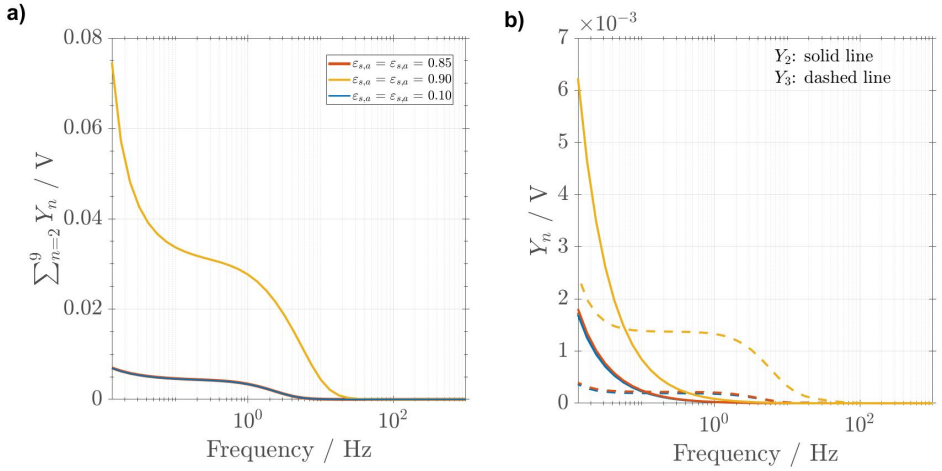

Figure A.4.: Simulation results for NFRA in the steady-state for the SIC electrolyte cell for a variation of the anode and cathode active material volume fraction ε_a, ε_c for a) sum of higher harmonics and b) individual harmonics Y_2 and Y_3 at SOC 85%. Further simulation parameters are provided in Table 5.2.

The active material volume fraction of the anode $\varepsilon_{s,a}$ and cathode $\varepsilon_{s,c}$ are simulta-

neously varied. With increasing active material volume fraction, the capacity of the cell and specific surface area of the electrode a_s increases. In parallel, the amount of electrolyte in the cell decreases and losses in the electrolyte increase. Due to the model characteristics, losses in the electrolyte are minimal. Therefore, as shown in Figure A.4 a), for the sum of higher harmonics, higher harmonic excitation due to a small amount of electrolyte in the electrodes is only visible, if the active material volume fraction is increased to $\varepsilon_{s,a,c} = 0.90$. This causes a signal increase in the overall excited frequency range. Until this volume fraction is reached positive effects due to the greater specific surface area dominate. Concerning individual harmonics, shown in Figure A.4 b), similar observations can be made. These results can be expected since, as priorly discussed, processes in the electrolyte influence the overall excited frequency range.

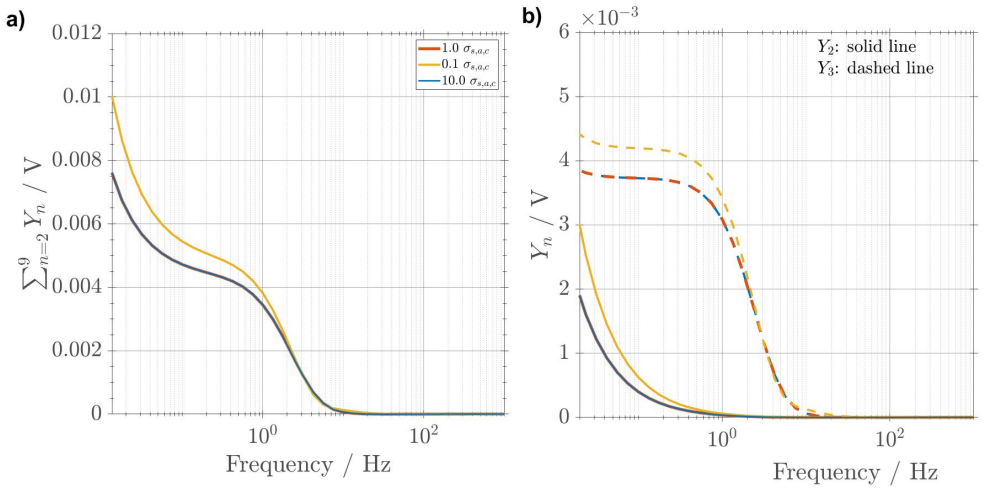

Figure A.5.: Simulation results for NFRA for the SIC electrolyte cell for a variation of the electrode conductivities $\sigma_{s,a,c}$ for a) sum of higher harmonics and b) individual harmonics Y_2 and Y_3 at SOC 85%. Further simulation parameters are provided in Table 5.2.

In Figure A.5 a), the sum of higher harmonics for a variation of the solid conductivities $\sigma_{s,a,c}$, is shown. Conductivities $\geq 1.0\ \sigma_{s,a,c,0}$ show no influence on the excitation of higher harmonics in the steady-state. In general, as priorly mentioned, the solid potential distributions itself follow Ohm's law and only cause a linear excitation of the system. Therefore, this effect is not visible with NFRA. Nevertheless, the solid potential interacts with the overpotentials for the reaction processes. Thereby, a potential gradient in the electrodes leads to different concentrations along the electrodes. This, in contrast to the Ohmic potential distribution, causes a nonlinear excitation of the

system and is visible in the NFRA; if a potential distribution along the electrodes is present. This is the case for conductivities $\leq 1.0\ \sigma_{s,a,c,0}$.

Individual harmonics, shown in Figure A.5 b), are influenced by the solid conductivities $\sigma_{s,a,c,0}$, along the overall excited frequency range. Further, no change in characteristic progression is visible, even for low conductivities $\sigma_{s,a,c,0}$.

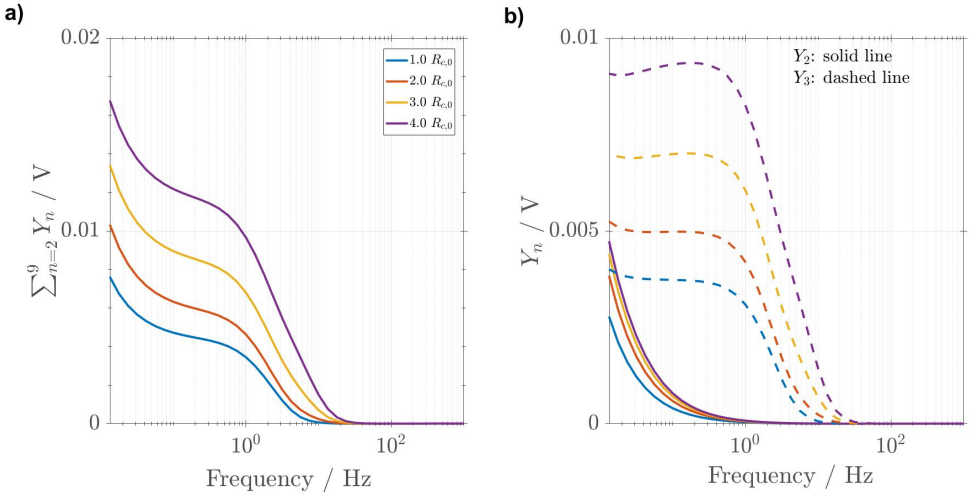

Figure A.6.: Simulation results for NFRA for the SIC electrolyte cell for a variation of the cathode active material radius R_c for a) sum of higher harmonics and b) individual harmonics Y_2 and Y_3 at SOC 85%. Further simulation parameters are provided in Table 5.2.

In Figure A.6 a), the sum of higher harmonics for a variation of the cathode active material radius R_c are shown. $R_{c,0}$ is thereby set to be R_c from Table 5.2. With increasing R_c, nonlinear voltage responses in the steady-state increase in the overall excited frequency range. This is in contrast to the investigation of the transient-state for the liquid electrolyte cell, in Chapter 3, where mostly the frequency ranges corresponding to the cathode reaction and diffusion were affected. In that case, the mentioned effect of influences on the overall excited frequency range is dominated by the transient state solution and therefore not visible.

For the steady-state simulation in general, the progression of individual harmonics is similar to the progressions observed in Chapter 2 and Chapter 4. Further, for individual harmonics, shown in Figure A.6 b), effects on both harmonics Y_2 and Y_3, are visible for a variation of R_c, since the active material radius R_c influences the reaction and diffusion process. Starting with R_c =3.0 $R_{c,0}$ a distinct maximum at around 0.2 Hz becomes visible. With increasing active material size, the maximum increases. This may also be observable for decreasing the reaction rate constant but with shifting of

the process's characteristic time constant.

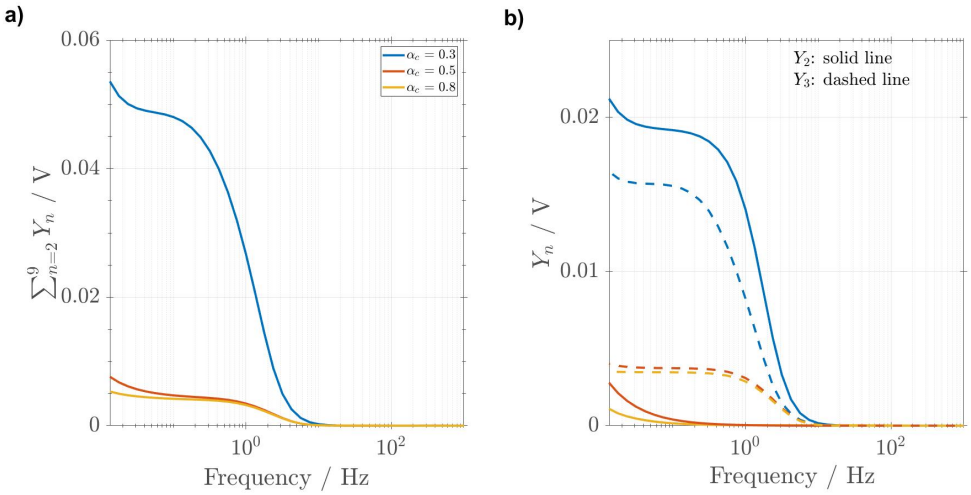

Figure A.7.: Simulation results for NFRA for the SIC electrolyte cell for a variation of the cathode reaction symmetry factor α_c for a) sum of higher harmonics and b) individual harmonics Y_2 and Y_3 at SOC 85%. Further simulation parameters are provided in Table 5.2.

In a next step, the influence of the cathode reaction symmetry factor α_c on NFR is investigated. The sum of higher harmonics is shown in Figure A.7 a). The reaction symmetry factor has priorly been investigated for NFR on singular processes, in Chapter 2. In that case, an asymmetric reaction ($\alpha \neq 0.5$) caused an excitation of the second harmonic Y_2 due to a change of the symmetry of the current voltage relation and barely influenced the excitation of Y_3. Within the investigation of the excitation of higher harmonics for the ASSB model, these observations have to be extended due to the more complex model characteristics including concentration effects. A change of the symmetry factor α_c does not only influence the symmetry of the reaction, but also the exchange current density $i_{0,c}$, according to equation 3.8. The greater α_c is, the greater the exchange current density $i_{0,c}$ becomes. For $\alpha_c = 0.5$ a perfectly symmetric reaction with an exchange current density of 0.3 Am^2 is present. For $\alpha = 0.8$, the exchange current density $i_{0,c}$ increases to 4.9 Am^2. Concerning the sum of higher harmonics, a decrease of nonlinear voltage responses can be seen. This confirms findings from Chapter 3 where an increasing reaction rate constant lead to decreasing higher harmonic voltage responses. Due to the high exchange current density $i_{0,c}$, the cathode reaction shows no influence on the sum of higher harmonics and a change in symmetry is not visible. This drastically changes for an investigation of $\alpha = 0.3$, where the exchange current density $i_{0,c}$ decreases to 0.05 Am^2, thereby in-

creasing the overpotentials of the reaction and simultaneously the nonlinear voltage responses.

If individual harmonics, shown in Figure A.7 b), are investigated, the priorly assumed change in symmetry for α =0.3 can be observed. Here, Y_2 is excited in the frequency range, characteristic for the electrochemical reaction. Further, nonlinear voltage responses of Y_2 and Y_3 are increased due to the low exchange current density $i_{0,c}$. If α =0.8 is investigated, no influence of the cathode reaction is present and therefore no change in symmetry and excitation of Y_2 can be seen.

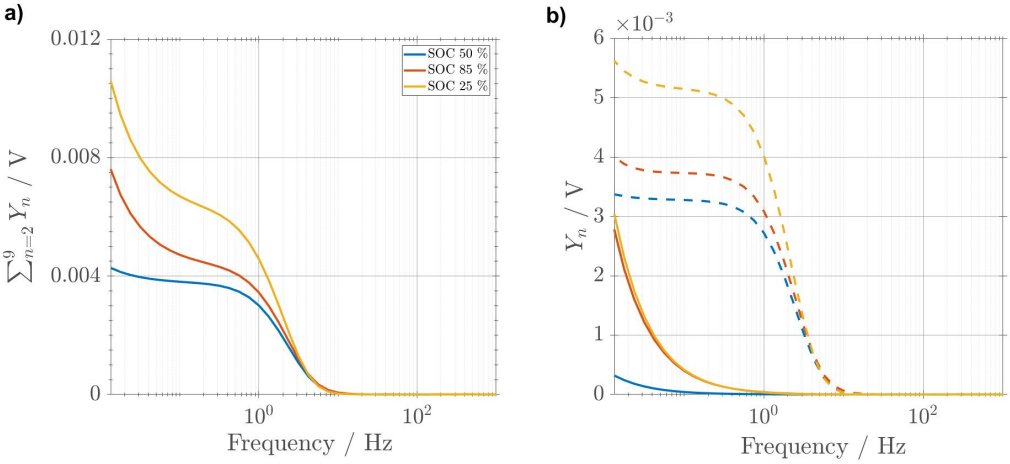

Figure A.8.: Simulation results for NFRA for the SIC electrolyte cell for a variation of the SOC for a) sum of higher harmonics and b) individual harmonics Y_2 and Y_3. Further simulation parameters are provided in Table 5.2.

In a last step, the influence of the SOC on the excitation of higher harmonics is investigated. Simulation results for the sum of higher harmonics are shown in Figure A.8 a). It well can be seen that for a moderate SOC of 50%, nonlinear voltage responses are smallest. For this SOC, both electrodes are approximately half charged and limitations can be expected to be minimal. For lower and higher SOCs, limitations occur and nonlinear voltage responses increase. These are highest for SOC 25%.

To further understand the limitations, individual harmonics, shown in Figure A.8 b), have to be investigated. As priorly described, the excitation of harmonics is minimal for the moderate SOC of 50%. If a higher or a lower SOC is investigated, a higher excitation of Y_2 in the low frequency domain is present. Therefore, a limiting diffusion process can be assumed. This effect is similar for a high and low SOC. A major difference between both SOCs can be seen in the excitation of Y_3. Here, a low SOC causes a higher excitation, thereby indicating a more limiting reaction process.

Concluding, the SOC is a sensitive parameter for the investigation with NFRA. Further model-based and experimental research should focus on the determination of the SOC at characteristic frequencies.

B Source Code for Higher Harmonic Voltage Responses

For the evaluation of higher harmonic voltage responses a fast Fourier transformation implemented in MATLAB is used. The adaptations of this embedded function are shown in the following.

Thereby T1 is a time vector and volt a voltage vector, both containing the last full simulated oscillation for every discrete frequency f. s and q are thereby possibilities to limit the examined frequency range. I_{Amp} is the current amplitude.

```
function [real,imag,Z,phi,U_Amp] = FFT_NFRA(T1,volt,f1,s,q,I_Amp)

%% Preallocating

r=8; %number of investigated higher harmonics

U_Amp=zeros([q,r]);

dc=zeros([q,r]); %dc offset

phi=zeros([q,r]);

real=zeros([q,r]);

imag=zeros([q,r]);

Z=zeros([q,r]);

frequency=zeros([(size(volt,1)-1)/2,q,r]); %Half of freq. vector

index1=zeros([q,r]); %Index for the investigated frequency

y=zeros([size(volt,1)-1,q,r]);

signal_angle=zeros([q,r]);
%% Calculation
```

```
for k=1:r
for i=s:q %Start and end of the frequency vector
f_NFRA(:,k)=k*f1; %inv. freq., changes for higher harmonics
N=size(volt,1);
N=N-1; %N has to be an integer after beeing divided by 2
t=T1(2,i)-T1(1,i); %Step width
fs=1/t; % Sampling frequency
f=(0:N-1)/N*fs;
frequency(:,i,k)=abs(f(1:N/2)-f_NFRA(i,k));
[~,index1(i,k)]=min(frequency(:,i,k)); %Find inv. freq.
y(:,i,k)=fft(volt(1:N,i),N); %fft of the voltage vector
mag(1:N/2+1,i,k)=abs(y(1:N/2+1,i,k)/N);
mag(2:end-1,i,k)=2*mag(2:end-1,i,k); %Magnitude of fft
signal_angle(i,k)=angle(y(index1(i,k),i,k));%Phaseshift
U_Amp(i,k)=mag(index1(i,k),i,k); %Amplitude at index value
dc(i,k)=mag(i,k)/2; %offset
phi(i,k)=signal_angle(i,k)-pi/2;
real(i,k)=(U_Amp(i,k)/I_Amp).*cos(phi(i,k))*1000;
imag(i,k)=(U_Amp(i,k)/I_Amp).*sin(phi(i,k))*1000;
Z(i,k)=sqrt((real(i,k).*real(i,k)+imag(i,k).*imag(i,k)));
phi(i,k)=phi(i,k)*360/(2*pi);

end
end
```

List of Symbols

a_s	specific surface area, m^{-1}
a	activity of reactant, -
A	area, m^2
A	reactant, -
b	valence of ions, -
B	Redlich-Kister parameter, J mol^{-1}
c	concentration, mol m^{-3}
C	double layer capacitance, F m−2
d	thickness, length, m
D	diffusion coefficient, m^2 s^{-1}
E_0	standard potential, V
f	frequency, s^{-1}
F	Faraday constant, C mol^{-1}
i_0	exchange current density, A m^{-2}
I	Current, A
j	current density, A m^{-3}
J	charge flux, A m^{-2}
k	reaction rate, $m^4 mol^{-1} s^{-1}$
L	thickness of cell, m
M	molar mass, kg mol^{-1}
n	amount of substance, mol
R	real gas constant, J mol^{-1} K^{-1}
r	radial coordinate, m
R	radius, m
t	time, s
t_p	transference number , -
T	temperature, K
T_P	turning point,
v	discrete function value, V
x	spacial coordinate, m
y	Lithium insertion rate, -
Y	Voltage response , V
z	number of sample points, -
α	reaction symmetry factor, -
β_s	reaction symmetry factor, -
β	Bruggeman's exponent, -
δ	width , m
Δ	difference, -
γ	activity coefficient, -
ε	volume fraction, -
η	reaction overpotential , V
σ	conductivity, S m^{-1}
ϕ	electrical potential, V
λ	reaction coefficient, A mol^{-1}
Θ	occupied surface sites, -
ψ	site-occupancy number, mol^{-1}
Γ	site density, m^{-2}

List of Abbreviations

ASSB:	All-Solid-State Batteries
CA:	Chronoamperometry
CV:	Cyclovoltammetry
CP:	Chronopotentiometry
ECM:	Equivilent Circuit Models
EIS:	Electrochemical Impedance Spectroscopy.
FFT:	fast-Fourier transformation
LiB:	Lithium-ion batteries
NFRA:	Nonlinear Frequency Response Analysis
P2D:	Pseudo-Two-Dimensional
rms:	root mean square
SEI:	Solid-Electrolyte-Interface
SIC:	Single-Ion-Conducting
SOC:	State-of-Charge
SP:	Single-Particle
THD:	Total Harmonic Distortion

Superscripts and Subscripts

0:	initial value
00:	standard potential
a:	anode
AC:	alternating current
Ads:	adsorption layer
b:	backwards
binary:	binary electrolyte
c:	cathode
Cell:	Cell
DC:	direct current
DL:	double layer
e:	electrolyte phase
f:	forward
f:	Faradaic
if:	SEI/Electrolyte interface
Li:	Lithium
Li^+:	cation
Li_2CO_3:	Lithium carbonate
max:	maximum value
mig:	migration
min:	minimal value
n:	negatively charged
n:	numerator
p:	positively charged
PF_6^-:	anion
OCV:	open circuit potential
rms:	root mean square
s:	solid phase
S:	SEI
SEI:	SEI phase
SIC:	Single-Ion-Conducting
tot:	total
v:	vacancy
+:	positively charged
0:	initial value

Bibliography

[1] R. van Noorden, The rechargeable revolution: A better battery, 2014. URL: https://www.nature.com/news/the-rechargeable-revolution-a-better-battery-1.14815.

[2] N. Nitta, F. Wu, J. T. Lee, G. Yushin, Li-ion battery materials : present and future, Materials Today 18 (2015) 252–264.

[3] J. Vetter, P. Novak, M. R. Wagner, C. Veit, K.-C. Möller, J. O. Besenhard, M. Winter, M. Wohlfahrt-Mehrens, C. Vogler, A. Hammouche, Ageing mechanisms in lithium-ion batteries, Journal of Power Sources 147 (2005) 269–281.

[4] N. Lin, F. Röder, U. Krewer, Multiphysics Modelling for Detailed Analysis of Multi-Layer Lithium-Ion Pouch Cells (submitted), Energies 11 (2018) 1–26.

[5] N. Legrand, S. Raël, B. Knosp, M. Hinaje, P. Desprez, F. Lapicque, Including Double-Layer Capacitance in Lithium-Ion Battery Mathematical Models, Journal of Power Sources 251 (2014) 370–378.

[6] A. Colclasure, R. Kee, Thermodynamically Consistent Modeling of Elementary Electrochemistry in Lithium-Ion Batteries, Electrochimica Acta 55 (2010) 8960–8973.

[7] J. Newman, K. E. Thomas-Alyea, Electrochemical Systems, John Wiley & Sons, 2004.

[8] A. M. Colclasure, K. A. Smith, R. J. Kee, Modeling Detailed Chemistry and Transport for Solid-Wlectrolyte-Interface (SEI) Films in Li-Ion Batteries, Electrochimica Acta 58 (2011) 33–43.

[9] N. Wolff, N. Harting, M. Heinrich, F. Röder, U. Krewer, Nonlinear Frequency Response Analysis on Lithium-Ion Batteries: A Model-Based Assessment, Electrochimica Acta 260 (2018) 614–622.

[10] M. Heinrich, N. Wolff, N. Harting, F. Röder, S. Seitz, U. Krewer, Physico-Chemical Modeling of a Lithium-Ion Battery: An Aging Study with Electrochemical Impedance Spectroscopy, Batteries & Supercaps 2 (2019) 1–12.

[11] N. Wolff, N. Harting, M. Heinrich, U. Krewer, Nonlinear Frequency Response Analysis on Lithium-Ion Batteries: Process Identifcation and Differences between Transient and Steady-State Behavior, Electrochimica Acta 298 (2019) 788–798.

[12] N. Wolff, F. Röder, U. Krewer, Model Based Assessment of Performance of Lithium-Ion Batteries Using Single Ion Conducting Electrolytes, Electrochimica Acta 284 (2018) 639–646.

[13] N. Wolff, N. Harting, F. Röder, M. Heinrich, U. Krewer, Understanding Nonlinearity in Electrochemical Systems, European Physical Journal Special Topics 227 (2019) 2617–2640.

[14] S. Michaelis, E. Maiser, A. Kampker, H. Heimes, C. Lienemann, S. Wessel, A. Thielmann, A. Sauer, T. Hettesheimer, Roadmap Batterie-Produktionsmittel 2030, VDMA Batterieproduktion, 2016.

[15] R. Jung, M. Metzger, F. Maglia, C. Stinner, H. A. Gasteiger, Oxygen Release and Its Effect on the Cycling Stability of $LiNi_xMn_yCo_zO_2$ (NMC) Cathode Materials for Li-Ion Batteries, Journal of the American Chemical Society 164 (2017) 1364–1377.

[16] C. Xu, F. Lindgren, B. Philippe, M. Gorgoi, Improved Performance of the Silicon Anode for Li-Ion Batteries: Understanding the Surface Modification Mechanism of Fluoroethylene Carbonate as an Effective Electrolyte Additive, Chemistry of Materials 27 (2015) 2591–2599.

[17] M. D. Wilka, Untersuchungen von Polarisationseffekten an Lithium-Ionen-Batterien, Ph.D. thesis, Universität Ulm, Zentrum für Sonnenenergie- und Wassterstoff-Forschung Ulm, 2013.

[18] J. B. Goodenough, K. Park, The Li-Ion Rechargeable Battery: A Perspective, Journal of the American Chemical Society 135 (2013) 1167–1176.

[19] S. F. Schuster, M. J. Brand, C. Campestrini, M. Gleissenberger, A. Jossen, Correlation between Capacity and Impedance of Lithium-Ion Cells during Calendar and Cycle Life, Journal of Power Sources 305 (2016) 191–199.

[20] M. Broussely, S. Herreyre, P. Biensan, P. Kasztejna, Aging Mechanism in Li-Ion Cells and Calendar Life Predictions, Journal of Power Sources 97-98 (2001) 12–21.

[21] C. Cao, Z.-B. Li, X.-L. Wang, X.-B. Zhao, W.-Q. Han, Recent Advances in Inorganic Solid Electrolytes for Lithium Batteries, Frontiers in Energy Research 2 (2014) 25–35.

[22] M. Tatsumisago, F. Mizuno, A. Hayashi, All-Solid-State Lithium Secondary Batteries using Sulfide-Based Glass–Ceramic Electrolytes, Journal of Power Sources 159 (2006) 193–199.

[23] N. Ohta, K. Takada, L. Zhang, R. Ma, M. Osada, T. Sasaki, Enhancement of the High-Rate Capability of Solid-State Lithium Batteries by Nanoscale Interfacial Modification, Advanced Materials 18 (2006) 2226–2229.

[24] F. Mizuno, C. Yada, H. Iba, Lithium-Ion Batteries - Advances and Applications, Elsevier, 2014.

[25] K. Takada, T. Inada, A. Kajiyama, M. Kouguchi, H. Sasaki, S. Kondo, Y. Michiue, S. Nakano, M. Tabuchi, M. Watanabe, Solid State Batteries with Sulfide-Based Solid Electrolytes, Solid State Ionics 172 (2004) 25–30.

[26] D. Santhanagopalan, D. Qian, T. McGilvray, Z. Wang, F. Wang, F. Camino, J. Graetz, N. Dudney, Y. S. Meng, Interface Limited Lithium Transport in Solid-State Batteries, Journal of Physical Chemistry Letters 5 (2014) 298–303.

[27] T. Uemura, K. Goto, M. Ogawa, K. Harada, High-Power All-Solid Secondary Battery with High Heat Resistance, Environment & Energy (2013) 132–136.

[28] G. Lenze, F. Röder, H. Bockholt, W. Haselrieder, A. Kwade, U. Krewer, Simulation-Supported Analysis of Calendering Impacts on the Performance of Lithium-Ion-Batteries, Journal of The Electrochemical Society 164 (2017) 1223–1233.

[29] M. Lewerenz, A. Marongiu, A. Warnecke, D. U. Sauer, Differential Voltage Analysis as a Tool for Analyzing Inhomogeneous Aging: A Case Study for $LiFePO_4$ Graphite Cylindrical Cells, Journal of Power Sources 368 (2017) 57–67.

[30] M. Dubarry, V. Svoboda, R. Hwu, B. Y. Liaw, Incremental Capacity Analysis and Close-to-Equilibrium OCV Measurements to Quantify Capacity Fade in Commercial Rechargeable Lithium Batteries, Electrochemical and Solid-State Letters 9 (2006) 454–457.

[31] J. Heinze, Cyclic Voltammetry - Electrochemical Spectroscopy, Angewandte Chemie 23 (1984) 831 – 918.

[32] J. Rusling, S. L. Suib, Characterizing Materials with Cyclic Voltammetry, Advanced Materials 6 (1994) 922–930.

[33] N. Elgrishi, K. J. Rountree, B. D. Mccarthy, E. S. Rountree, T. T. Eisenhart, J. L. Dempsey, A Practical Beginner's Guide to Cyclic Voltammetry, Journal of Chemical Education 95 (2018) 197–206.

[34] D. M. Bernardi, J. Go, Analysis of Pulse and Relaxation Behavior in Lithium-Ion Batteries, Journal of Power Sources 196 (2011) 412–427.

[35] H. Schweiger, O. Obeidi, O. Komesker, A. Raschke, M. Schiemann, C. Zehner, M. Gehnen, M. Keller, P. Birke, Comparison of Several Methods for Determining the Internal Resistance of Lithium Ion Cells., Sensors 10 (2010) 5604–5625.

[36] A. J. Bard, L. R. Faulkner, E. Swain, C. Robey, Electrochemical Methods: Fundamentals and Applications, John Wiley & Sons, 2001.

[37] U. Krewer, A. Kamat, K. Sundmacher, Understanding the Dynamic Behaviour of Direct Methanol Fuel Cells : Response to Step Changes in Cell Current, Journal of Electroanalytical Chemistry 609 (2007) 105–119.

[38] H. Baltruschat, Differential Electrochemical Mass Spectrometry, American Society for Mass Spectrometry 15 (2004) 1693–1705.

[39] F. Kubannek, U. Krewer, A Cyclone Flow Cell for Quantitative Analysis of Kinetics at Porous Electrodes by Differential Electrochemical Mass Spectrometry, Electrochimica Acta 210 (2016) 862–873.

[40] D. Klotz, Characterization and Modeling of Electrochemical Energy Conversion Systems by Impedance Techniques, Ph.D. thesis, Karlsruher Institut für Technoligie, 2012.

[41] D. Andre, M. Meiler, K. Steiner, C. Wimmer, T. Soczka-Guth, D. U. Sauer, Characterization of High-Power Lithium-Ion Batteries by Electrochemical Impedance Spectroscopy. I. Experimental Envestigation, Journal of Power Sources 196 (2011) 5334–5341.

[42] J. R. Macdonald, Impedance Spectroscopy, John Wiley & Sons, 1987.

[43] J. Melorose, R. Perroy, S. Careas, Lithium-Ion Batteries - Solid-Electrolyte Interphase, 1 ed., Imperial College Press, 2004.

[44] J. Koryta, J. Dvorak, V. Bohackova, Lehrbuch der Elektrochemie, Springer Verlag, 2012.

[45] H. Varela, K. Krischer, Nonlinear Phenomena during Electrochemical Oxidation of Hydrogen on Platinum Electrodes, Catalysis Today 70 (2001) 411–425.

[46] M. Koper, Non-Linear Phenomena in Electrochemical Systems, Journal of the Chemical Society, Faraday Transactions 94 (1998) 1369–1378.

[47] N. Harting, N. Wolff, F. Röder, U. Krewer, Nonlinear Frequency Response Analysis (NFRA) on Lithium-Ion Batteries, Electrochimica Acta 248 (2017) 133–139.

[48] H. R. E. Siller, Non-Linear Modal Analysis Methods for Engineering, Ph.D. thesis, Imperial College London, 2004.

[49] W. M. Grady, S. Santoso, Understanding Power System Harmonics, IEEE Power Engineering Review 21 (2001) 8–11.

[50] A. Metya, M. Ghosh, N. Parida, S. Palit Sagar, Higher Harmonic Analysis of Ultrasonic Signal for Ageing Behaviour Study of C-250 Grade Maraging Steel, NDT and E International 41 (2008) 484–489.

[51] G. Vampa, C. R. McDonald, G. Orlando, D. D. Klug, P. B. Corkum, T. Brabec, Theoretical Analysis of High-Harmonic Generation in Solids, Physical Review Letters 113 (2014) 073901.

[52] K. Darowicki, J. Majewska, Harmonic Analysis of Electrochemical and Corrosion Systems - a Review, Corrosion Reviews 17 (1999) 383–399.

[53] T. R. Vidakovic-Koch, V. V. Panic, M. Andric, M. Petkovska, K. Sundmacher, Nonlinear Frequency Response Analysis of the Ferrocyanide Oxidation Kinetics . Part I . A Theoretical Analysis, The Journal of Physical Chemistry C 115 (2011) 17341–17351.

[54] T. R. Vidakovic-Koch, V. V. Panic, M. Andric, M. Petkovska, K. Sundmacher, Nonlinear Frequency Response Analysis of the Ferrocyanide Oxidation Kinetics . Part II . Measurement Routine and Experimental Validation, The Journal of Physical Chemistry C 115 (2011) 17352–17358.

[55] M. Kiel, O. Bohlen, D. U. Sauer, Harmonic Analysis for Identification of Nonlinearities in Impedance Spectroscopy, Electrochimica Acta 53 (2008) 7367–7374.

[56] B. Bensmann, M. Petkovska, R. Hanke-rauschenbach, K. Sundmacher, Nonlinear Frequency Response of Electrochemical Methanol Oxidation Kinetics : A Theoretical Analysis, Journal of The Electrochemical Society 157 (2010) 1279–1289.

[57] T. Kadyk, R. Hanke-Rauschenbach, K. Sundmacher, Nonlinear Frequency Response Analysis of PEM Fuel Cells for Diagnosis of Dehydration, Flooding and CO-Poisoning, Journal of Electroanalytical Chemistry 630 (2009) 19–27.

[58] T. Kadyk, R. Hanke-Rauschenbach, K. Sundmacher, Nonlinear Frequency Response Analysis for the Diagnosis of Carbon Monoxide Poisoning in PEM Fuel Cell Anodes, Journal of Applied Electrochemistry 41 (2011) 1021–1032.

[59] T. Kadyk, R. Hanke-Rauschenbach, K. Sundmacher, Nonlinear Frequency Response Analysis of Dehydration Phenomena in Polymer Electrolyte Membrane Fuel Cells, International Journal of Hydrogen Energy 37 (2012) 7689–7701.

[60] Q. Mao, U. Krewer, R. Hanke-Rauschenbach, Total Harmonic Distortion Analysis for Direct Methanol Fuel Cell Anode, Electrochemistry Communications 12 (2010) 1517–1519.

[61] Q. Mao, U. Krewer, Total Harmonic Distortion Analysis of Oxygen Reduction Reaction in Proton Exchange Membrane Fuel Cells, Electrochimica Acta 103 (2013) 188–198.

[62] Q. Mao, U. Krewer, Sensing Methanol Concentration in Direct Methanol Fuel Cell with Total Harmonic Distortion: Theory and Application, Electrochimica Acta 68 (2012) 60–68.

[63] J. R. Wilson, D. T. Schwartz, S. B. Adler, Nonlinear Electrochemical Impedance Spectroscopy for Solid Oxide Fuel Cell Cathode Materials, Electrochimica Acta 51 (2006) 1389–1402.

[64] N. Harting, N. Wolff, U. Krewer, Identification of Lithium Plating in Lithium-Ion Batteries using Nonlinear Frequency Response Analysis (NFRA), Electrochimica Acta 281 (2018) 378–385.

[65] N. Harting, R. Schenkendorf, N. Wolff, U. Krewer, State-of-Health Identification of Lithium-Ion Batteries Based on Nonlinear Frequency Response Analysis: First Steps with Data Mining, Applied Sciences 8 (2018) 1–14.

[66] N. Harting, N. Wolff, R. Fridolin, U. Krewer, State-of-Health Diagnosis of Lithium-Ion Batteries Using Nonlinear Frequency Response Analysis, Journal of the Electrochemical Society 166 (2019) 277–285. doi:10.1149/2.1031902jes.

[67] M. D. Murbach, D. T. Schwartz, Extending Newman's Pseudo-Two-Dimensional Lithium-Ion Battery Impedance Simulation Approach to Include the Nonlinear Harmonic Response, Journal of The Electrochemical Society 164 (2017) 3311–3320.

[68] A. Buonomo, A. Lo Schiavo, A Method for Analysing the Transient and the Steady-State Oscillations in Third-Order Oscillators with Shifting Bias, International Journal of Circuit Theory and Applications 29 (2001) 469–486.

[69] V. Ramadesigan, P. W. C. Northrop, S. De, S. Santhanagopalan, R. D. Braatz, V. R. Subramanian, Modeling and Simulation of Lithium-Ion Batteries from a

Systems Engineering Perspective, Journal of The Electrochemical Society 159 (2012) 31–45.

[70] M. Doyle, T. F. Fuller, J. Newman, Modeling of Galvanostatic Charge and Discharge of the Lithium / Polymer / Insertion Cell, Journal of The Electrochemical Society 140 (1993) 1526–1533.

[71] I. J. Ong, J. Newman, Double-Layer Capacitance in a Dual Lithium Ion Insertion Cell, Journal of The Electrochemical Society 146 (1999) 4360–4365.

[72] F. Röder, R. D. Braatz, U. Krewer, Multi-Scale Simulation of Heterogeneous Surface Film Growth Mechanisms in Lithium-Ion Batteries, Journal of the Electrochemical Society 164 (2017) 3335–3344.

[73] K. Becker-Steinberger, S. Funken, M. Landstorfer, K. Urban, A Mathematical Model for All Solid-State Lithium Ion Batteries, Journal of The Electrochemical Society 25 (2009) 285–296.

[74] M. Landstorfer, S. Funken, T. Jacob, An Advanced Model Framework for Solid Electrolyte Intercalation Batteries., Physical chemistry chemical physics: PCCP 13 (2011) 12817–12825.

[75] A. Bates, S. Mukherjee, N. Schuppert, B. Son, J. Kim, S. Park, Modeling and Simulation of 2D Lithium-Ion Solid State Battery, International Journal of Energy Research 39 (2015) 1508–1518.

[76] D. Danilov, R. A. H. Niessen, P. H. L. Notten, Modeling All-Solid-State Li-Ion Batteries, Journal of The Electrochemical Society 158 (2011) 215–222.

[77] U. Krewer, T. Vidakovic-Koch, L. Rihko-Struckmann, Electrochemical Oxidation of Carbon-Containing Fuels and Their Dynamics in Low-Temperature Fuel Cells, ChemPhysChem 12 (2011) 2518–2544.

[78] T. Jacobsen, K. West, Diffusion Impedance in Planar, Cylindrical and Spherical Symmetry, Electrochimica Acta 40 (1995) 255–262.

[79] D. Aurbach, B. Markovsky, I. Weissman, E. Levi, Y. Ein-Eli, On the Correlation between Surface Chemistry and Performance of Graphite Negative Electrodes for Li Ion Batteries, Electrochim. Acta 45 (1999) 67–86.

[80] E. Peled, D. Golodnitsky, G. Ardel, The SEI Model-Application to Lithium-Polymer Electrolyte Batteries, Electrochimica Acta 40 (1995) 2197–2204.

[81] L. Gao, D. D. Macdonald, Characterization of Irreversible Processes at the Li/Poly[bis(2,3-di-(2-methoxyethoxy)propoxy)phospazene] Interface on Charge Cycling, Journal of The Electrochemical Society 144 (1997) 1174–1179.

[82] D. D. Macdonald, The Point Defect Model for the Passive State, Journal of The Electrochemical Society 139 (1992) 3434–3449.

[83] I. Nainville, A. Lemarchand, J.-P. Badiali, Passivation of a Lithium Anode: A Simulation Model, Electrochim. Acta 41 (1996) 2855–2863.

[84] J. Christensen, J. Newman, A Mathematical Model for the Lithium-Ion Negative Electrode Solid Electrolyte Interphase, Journal of The Electrochemical Society 151 (2004) 1977–1988.

[85] T. G. Zavalis, M. Klett, M. H. Kjell, M. Behm, R. W. Lindström, G. Lindbergh, Aging in Lithium-Ion Batteries: Model and Experimental Investigation of Harvested LiFePO4 and Mesocarbon Microbead Graphite Electrodes, Electrochimica Acta 110 (2013) 335–348.

[86] Y. Xie, J. Li, C. Yuan, Mathematical Modeling of the Electrochemical Impedance Spectroscopy in Lithium Ion Battery Cycling, Electrochimica Acta 127 (2014) 266–275.

[87] M. R. Busche, T. Drossel, T. Leichtweiss, D. A. Weber, M. Falk, M. Schneider, M. Reich, H. Sommer, P. Adelhelm, J. Janek, Dynamic Formation of a Solid-Liquid Electrolyte Interphase and its Consequences for Hybrid-Battery Concepts, Nature Chemistry 8 (2016) 426–434.

[88] J. P. Meyers, M. Doyle, R. M. Darling, J. Newman, The Impedance Response of a Porous Electrode Composed of Intercalation Particles, Journal of the Electrochemical Society 147 (2000) 2930–2940.

[89] Y. Yamada, F. Sagane, Y. Iriyama, T. Abe, Z. Ogumi, Kinetics of Lithium-Ion Transfer at the Interface between $Li_{0.35}La_{0.55}TiO_3$ and Binary Electrolytes, The Journal of Physical Chemistry 113 (2009) 14528–14532.

[90] F. Helfferich, Kinetics of Homogeneous Multistep Reactions, Elsevier, 2001.

[91] P. Arora, R. E. White, M. Doyle, Capacity Fade Mechanisms and Side Reactions in Lithium-Ion Batteries, Journal of the Electrochemical Society 145 (1998) 3647–3667.

[92] F. Yang, D. Wang, Y. Zhao, K. Tsui, S. Joo, A Study of the Relationship between Coulombic Efficiency and Capacity Degradation of Commercial Lithium-Ion Batteries, Energy 145 (2018) 486–495.

[93] S.-L. Wu, A. E. Javier, D. Devaux, N. P. Balsara, V. Srinivasan, Discharge Characteristics of Lithium Battery Electrodes with a Semiconducting Polymer Studied by Continuum Modeling and Experiment, Journal of the Electrochemical Society 161 (2014) 1836–1843.

[94] K. Takahashi, V. Srinivasan, Examination of Graphite Particle Cracking as a Failure Mode in Lithium-Ion Batteries: A Model-Experimental Study, Journal of the Electrochemical Society 162 (2015) 635–645.

[95] L. H. Saw, Y. Ye, A. A. O. Tay, Electrochemical-Thermal Analysis of 18650 Lithium Iron Phosphate Cell, Energy Conversion and Management 75 (2013) 162–174.

[96] R. E. Gerver, J. P. Meyers, Three-Dimensional Modeling of Electrochemical Performance and Heat Generation of Lithium-Ion Batteries in Tabbed Planar Configurations, Journal of The Electrochemical Society 158 (2011) 835–843.

[97] Y. Kato, S. Hori, S. Toshiya, K. Suzuki, M. Hirayama, A. Mitsui, M. Yonemura, H. Iba, R. Kanno, High-Power All-Solid-State Batteries Using Sulfide Superionic Conductors, Nature Energy 1 (2016) 1–7.

[98] M. Ogawa, K. Yoshida, K. Harada, All-Solid-State Lithium Batteries with Wide Operating Temperature Range, SEI Technical Review 74 (2012) 88–90.

[99] H. Hahn, T. Danner, M. Singh, S. Hein, A. Latz, Thick Electrodes for Li-Ion Batteries : A Model Based Analysis, Journal of Power Sources 334 (2016) 191–201.

[100] S. Tippmann, D. Walper, L. Balboa, B. Spier, W. G. Bessler, Low-Temperature Charging of Lithium-Ion Cells Part I: Electrochemical Modeling and Experimental Investigation of Degradation Behavior, Journal of Power Sources 252 (2014) 305–316.

[101] J. Illig, J. P. Schmidt, M. Weiss, A. Weber, E. Ivers-tiffée, Understanding the Impedance Spectrum of 18650 $LiFePO_4$-Cells, Journal of Power Sources 239 (2013) 670–679.